UNIVERSITY OF OKLAHOMA

GRADUATE COLLEGE

ESTIMATION OF RELATIVE PERMEABILITY IN NANOPOROUS SAMPLES AND MODELING OF PRESSURE TRANSIENT RESPONSE IN NATURALLY FRACTURED RESERVOIRS

A THESIS

SUBMITTED TO THE GRADUATE FACULTY

in partial fulfillment of the requirements for the

Degree of

MASTER OF SCIENCE

By

SHIV PRAKASH OJHA
Norman, Oklahoma
2017

Downloaded from SHAREOK. Persistent Handle URL: https://hdl.handle.net/11244/52773

ESTIMATION OF RELATIVE PERMEABILITY IN NANOPOROUS SAMPLES AND MODELING OF PRESSURE TRANSIENT RESPONSE IN NATURALLY FRACTURED RESERVOIRS

A THESIS APPROVED FOR THE
MEWBOURNE SCHOOL OF PETROLEUM AND GEOLOGICAL ENGINEERING

BY

_____
Dr. Siddharth Misra, Chair

_____
Dr. Chandra S. Rai

_____
Dr. Deepak Devegowda

© Copyright by SHIV PRAKASH OJHA 2017
All Rights Reserved.

This thesis is dedicated to my family and friends who have helped me stay focused.

ACKNOWLEDGEMENTS

I appreciate and thank all those who have helped me technically and personally in completing this thesis work successfully.

First and foremost, I sincerely thank my advisor, Dr. Siddharth Misra for giving me an opportunity to work under his guidance. His working style showed me the importance of perseverance and dedication in academic research. His consistent guidance and constructive feedbacks have helped me to improve my research aptitude, technical writing skills and my analytical abilities.

I also thank my thesis committee members, Dr. Chandra Rai and Dr. Deepak Devegowda for their invaluable inputs and suggestions during the review of this thesis. Their comments helped me to improve my work and present it better in the form of this thesis.

This thesis is dedicated to my family including my parents, my elder brother, my sister-in-law and my two year old nephew. Their constant support and encouragement has allowed me to focus on my research work.

Lastly, I convey my gratitude to my colleagues Yifu Han, Sangcheol Yoon, Ankita Sinha, Son Dang and Dr. Ali Tinni along with numerous other individuals. They contributed to this research by providing suggestions and comments which helped me to improve the outcome of this thesis.

TABLE OF CONTENTS

ACKNOWLEDGEMENTS ..... **iv**

TABLE OF CONTENTS ..... **v**

LIST OF TABLES ..... **vii**

LIST OF FIGURES ..... **ix**

ABSTRACT ..... **xv**

CHAPTER 1: INTRODUCTION **1**

1.1 Estimation of relative permeability in shale reservoirs 1

1.2 Modeling of pressure transient response in shale reservoirs with natural fractures using Fast Marching (FM) Method 5

1.3 Objectives 7

CHAPTER 2: METHOD FOR ESTIMATING RELATIVE PERMEABILITY AND PORE NETWORK CHARACTERISTICS **9**

2.1 Laboratory Measurements of Adsorption-Desorption Isotherm (ADI). 9

2.2 Properties of samples used for this study 10

2.3 Procedure for cleaning and ashing of samples 11

2.4 Adsorption-desorption isotherm interpretation methodology 12

2.5 Assumptions made in the approach 35

2.6 Limitations of the approach 36

CHAPTER 3: ESTIMATION OF PORE NETWORK CHARACTERISTICS **38**

3.1 Estimation of pore size distribution(PSD) and associated characteristics 38

3.2 Correlations of APV and average pore diameter with LPP Porosity and TOC: 40

3.3 Impact of Cleaning and Ashing 42

CHAPTER 4: ESTIMATION OF RELATIVE PERMEABILITY AND RESIDUAL/IRREDUCIBLE SATURATIONS **53**

4.1 Estimation of relative permeability and residual/irreducible saturations 53

4.2 Sensitivity of relative permeability curves to network properties 57

4.3 Correlations of estimates with ADI pore volume, TOC and LPP porosity. 62

4.4 Impact of Ashing and Cleaning on relative permeability estimates 64

4.5 Applications to performance prediction. 66

CHAPTER 5: MODELING OF PRESSURE TRANSIENT RESPONSE IN NATURALLY FRACTURED RESERVOIRS 73

5.1 Multistencil Fast Marching (MFM) Method 73

5.2 Workflow for generating 2D reservoir diffusivity map used to study the effects of conductive natural fractures on pressure front propagation and pressure transient response . 77

5.3 Assumptions made in the approach 78

5.4 Limitations of the approach 79

5.5 Illustration and Validation of Method 79

5.6 Sensitivity of pressure transient response to properties of the naturally fractured reservoir 87

CHAPTER 6: CONCLUSIONS AND RECOMMENDATIONS 102

6.1 Conclusions 102

6.2 Recommendations for Future Work 104

REFERENCES 105

APPENDIX A: NOMENCLATURE 112

LIST OF TABLES

Table 2.1: Petrophysical properties of shale samples studied using the ADI measurements. 10

Table 2.2: Comparison of estimated and published *Z* and *L* estimates 34

Table 4.1: Default values of model parameters used for the sensitivity study on the relative permeability model. 58

Table 4.2: Default values of the key inputs used in simulation fluid flow models to demonstrate the impact of relative permeability curves on the production performance for Case-1. 67

Table 4.3: Fracture and horizontal well inputs used in simulation fluid flow models to demonstrate the impact of relative permeability curve on the production performance for Case-2. 68

Table 4.4: Fluid inputs used in simulation fluid flow models to demonstrate the impact of relative permeability curve along with fluid viscosity on the production performance for Case-3. 72

Table 5.1- Summary of parameters assumed for the reservoir model shown in Figure 5.2a. 80

Table 5.2: Summary of parameters used for the comparisons shown in Figure 5.3. 84

Table 5.3: Summary of inputs used for Base Case of pressure transient response of a vertical production well in sensitivity study of characteristic properties of naturally fractured reservoir. 88

Table 5.4: Summary of inputs used sensitivity on volume fraction of fractures. 88

Table 5.5: Summary of inputs used sensitivity on fracture permeability. 91

Table 5.6: Summary of inputs used sensitivity on compressibility of fractures. 94

Table 5.7: Summary of inputs used sensitivity on location of source well. 95

Table 5.8: Summary of inputs used for normal distribution of fracture length and fracture orientation. 97

LIST OF FIGURES

Figure 2.1: Boxplots showing range and variation in measurements made on the samples for (a) LPP porosity (pu), and (b) TOC (wt. %). 11

Figure 2.2: Flowchart for ADI Interpretation and relative permeability estimation..... 14

Figure 2.3: Comparison of the estimated PSDs against those published by (a) Kruk et al. (1997) for MCM-41 sample presented in Figures 2 and 8 of the referenced literature, (b) Kruk et al. (2000) for S4 sample presented in Figures 4 and 5 of the referenced literature, and (c) Liu et al. (1992) for Sample A presented in Figures 1 and 4 of the referenced literature. 32

Figure 2.4: Estimated *F(P)* vs. *f(P)* plots against those published by Liu et al. (1992) for (a) cylindrical pore geometry (b) slit pore geometry. The sample referred here is Sample-A with data shown in Figures 1,4, and 6 of the referenced literature. 33

Figure 3.1: (a) Incremental pore size distribution, and (b) cumulative pore size distribution for samples from different thermal maturity windows from Bakken, Woodford and Wolfcamp formations. 39

Figure 3.2: (a) Incremental and (b) cumulative pore size distributions for samples from different thermal maturity windows of Eagle Ford (EF) and Wolfcamp (WF) formations. 39

Figure 3.3: Crossplots of (a) LPP porosity before cleaning versus ADI pore volume, and (b) TOC before cleaning versus ADI pore volume for native samples from various maturity windows..... 41

Figure 3.4: Crossplots of average pore diameter versus APV for (a) native samples, and (b) cleaned samples from various maturity windows. 42

Figure 3.5: Crossplots of (a) change in ADI porosity due to ashing versus LPP porosity before ashing and (b) change in ADI porosity due to ashing versus TOC before ashing of samples from gas and oil windows. 43

Figure 3.6: Crossplots of (a) average pore diameter of cleaned samples and (b) average pore diameter of ashed samples versus the average pore diameter of native samples. . 44

Figure 3.7: Incremental pore size distributions of (a) native samples and (b) cleaned samples..... 45

Figure 3.8: Incremental pore size distributions (a) Eagle Ford oil window samples and (b) Eagle Ford gas window samples in their native state and after ashing. 46

Figure 3.9: Pore-size window-based comparison of changes in pore size distribution. 46

Figure 3.10: Boxplots showing range and variation of (a) coordination number (Z), (b) percolation cluster length (L), and (c) fractal dimension of first fractal regime (D_1) estimates for samples from various maturity windows..... 47

Figure 3.11. Estimates of coordination number of native samples versus (a) cleaned samples and those versus (b) ashed samples..... 48

Figure 3.12: Crossplot of percolation cluster length (L) versus APV for native samples from various maturity windows. 49

Figure 3.13: Crossplots of (a) fractal dimension of first fractal regime (D_1) versus APV and (b) fractal dimension of second fractal regime (D_2) versus APV for native samples from various maturity windows. 51

Figure 3.14: Estimates of fractal dimension of first fractal regime (D_1) of native versus (a) cleaned samples and those versus (b) ashed samples. 52

Figure 3.15: Estimates of fractal dimension of second fractal regime (D_2) of native versus (a) cleaned samples and those versus (b) ashed samples. 52

Figure 4.1: Relative permeability curves for wetting and non-wetting phases for (a) Bakken, Woodford and Wolfcamp samples from dataset-1 mentioned in Table 2.1 and (b) Eagle Ford and Wolfcamp samples from dataset-2 mentioned in Table 2.1. 56

Figure 4.2: Correlation between relative permeability and residual/irreducible saturations for (a) non-wetting hydrocarbon phase at S_w=0.5 and (b) wetting aqueous phase at S_w = 0.8..... 57

Figure 4.3: Relative permeability curves for wetting and non-wetting phases for sensitivity of (a) coordination number (Z), (b) fluid content level for switch between percolation and effective medium formulations (θ_x), (c) pore diameter for change of fractal regimes (d_x), (d) probability of drainage for first fractal regime (β_1), and (e) fractal dimension of first fractal regime (D_1). 60

Figure 4.4: Crossplots of (a) residual hydrocarbon saturation (S_{hcr}) and that of (b) irreducible water saturation (S_{wir}) with ADI pore volume (APV). 63

Figure 4.5: Crossplots between (a) residual hydrocarbon saturation (S_{hcr}) and TOC, and that between (b) irreducible water saturation (S_{wir}) and TOC..... 63

Figure 4.6: Changes in (a) residual hydrocarbon saturation (S_{hcr}) and (b) irreducible water saturation (S_{wir}) of samples due to cleaning with methanol-toluene mixture. 64

Figure 4.7: Changes in relative permeability due to (a) cleaning with methanol-toluene mixture, (b) ashing for Eagle Ford gas window samples, and (c) ashing for Eagle Ford oil window sample. 65

Figure 4.8: Simulation-generated (a) cumulative gas production and (b) cumulative water production of a vertical well (Case-1) in various formations. 69

Figure 4.9: Simulation-generated (a) cumulative gas production and (b) cumulative water production of a horizontal fractured well (Case-2) in various formations..... 69

Figure 4.10: Simulation-generated (a) cumulative oil productions of oil-window formations, and (b) cumulative gas productions of condensate and late condensate window formations using horizontal wells of similar design as in Case-2..... 71

Figure 5.1: Schematic of multistencil fast marching (MFM) algorithm..... 75

Figure 5.2: (a) Permeability map of the abstract reservoir, (b) MFM-generated arrival times for the pressure front propagating across the reservoir, and (c) pressure change and Bourdet-type pressure derivative responses of a vertical production well located in the center of the abstract reservoir. 82

Figure 5.3: Validations of MFM-assisted predictions against Kappa Saphir predictions of pressure and its derivative responses in (a) unfractured and (b) fractured vertical well located centrally in bounded circular homogeneous reservoir for various reservoir permeabilities. 83

Figure 5.4: (a) Concentric reservoir model with 5-ft wide zones of alternating permeabilities, and (b) sector reservoir model with 5°-angle sectors of alternating permeabilities. 84

Figure 5.5: Pressure difference and pressure derivative responses of a vertical production well centrally located in (a) concentric model shown in Figure 5.4a and (b) sector model shown in Figure 5.4b. Temporal evolution of drainage areas till 10 days for (c) case-1 of concentric model and that for (d) case-1 of sector model..... 86

Figure 5.6: (a) Reservoir map for Base Case (dimension of square area shown in map is 1000 ft), and (b) pressure difference and pressure derivative responses of a vertical production well centrally located in Base Case reservoir. 89
Figure 5.7: Reservoir map for (a) Base Case, (b) Case-1, and (c) Case-2. The dimension of square shown in each plot is 1000 ft..... 89
Figure 5.8: Time of arrival maps at *t*=10 days for (a) Base Case, (b) Case-1, and (c) Case-2. The dimension of square shown in each plot is 1000 ft..... 89
Figure 5.9: Pressure derivative responses of a vertical production well centrally located in reservoir to study sensitivity on volume fraction of fractures. 90
Figure 5.10: Reservoir map for (a) Base Case, (b) Case-3, (c) Case-4, and (d) Case-5. The dimension of square shown in each plot is 1000 ft..... 91
Figure 5.11: Time of arrival maps at *t*=10 days for (a) Base Case, (b) Case-3, (c) Case-4, and (d) Case-5. The dimension of square shown in each plot is 1000 ft. 93
Figure 5.12: Pressure derivative responses of a vertical production well centrally located in reservoir to study sensitivity on permeability of fractures. 93
Figure 5.13: Time of arrival maps at *t*=10 days for (a) Base Case, (b) Case-6, and (c) Case-7. The dimension of square shown in each plot is 1000 ft..... 94
Figure 5.14: Pressure derivative responses of a vertical production well centrally located in reservoir to study sensitivity on compressibility of fractures. 94
Figure 5.15: Reservoir map for (a) Base Case, (b) Case-8, and (c) Case-9. The dimension of square shown in each plot is 650 ft..... 95
Figure 5.16: Time of arrival maps at *t*=1 day for (a) Base Case, (b) Case-8, and (c) Case-9. The dimension of square shown in each plot is 650 ft..... 95

Figure 5.17: Pressure derivative responses of a vertical production well in reservoir to study sensitivity on location of source well. 96
Figure 5.18: Reservoir map for (a) Base Case, (b) Case-10, and (c) Case-11 to implement variation in fracture length and orientation according to normal distribution. The dimension of square shown in each plot is 650 ft. 97
Figure 5.19: Time of arrival maps at t=10 days for (a) Base Case, (b) Case-10, and (c) Case-11. The dimension of square shown in each plot is 650 ft. 97
Figure 5.20: Comparison of normal distribution expected with that generated using Matlab for (a) length of natural fractures (Case-10), and (b) orientation of fractures (Case-11). (c) Pressure derivative responses of a vertical production well centrally located in reservoir to study impact of variation in fracture length and orientation. 98
Figure 5.21- Reservoir maps for realizations in Cases 12-20 shown in (a)-(i) to show impact of change in position of natural fractures around well. The dimension of square shown in each plot is 650 ft. 99
Figure 5.22: Pressure derivative responses of a vertical production well centrally located in reservoir to study impact of variation in position of fractures with random distribution between different realizations. 100

ABSTRACT

Relative permeability and irreducible saturations of organic-rich shale samples from various formations from different maturity windows are estimated by processing the low-pressure nitrogen adsorption-desorption measurements. Using percolation theory, effective medium theory and critical path analysis along with bimodal fractal regime, we estimate relative permeability curves for 100 samples of Bakken, Eagle Ford, Woodford, and Wolfcamp formations. The process also allows estimation of percolation and fractal parameters like coordination number and fractal dimension which facilitate description of the pore network for these shale samples. Transport properties are compared across different windows of maturity. Subsequently, reservoir simulation is used to predict the biphasic production performances of the corresponding formations and correlate predictions with field performance in unconventional reservoirs.

Pressure transient analysis (PTA) can describe properties of subsurface natural fractures. Multistencils fast marching (MFM) method provides a reliable way to analyze the effects of natural fractures on the time-varying drainage volume and pressure transient response due to a production/injection well. The method is validated in various heterogeneous reservoirs against the response of equivalent systems generated using the Kappa Saphir commercial software. We study the sensitivities of pressure transients to fracture characteristics, such as fracture length, fracture compressibility, fracture permeability, angle of orientation, and fracture volume fraction in the reservoir. In doing so, we identify diagnostic signatures associated with these fracture characteristics.

CHAPTER 1: INTRODUCTION

1.1 Estimation of relative permeability in shale reservoirs

Relative permeability characterizes multiphase flow in porous media by quantifying the reduction in fluid flow due to surface-tension effects between fluids and chemical interaction between fluids and the mineralogy of the rock matrix. Relative permeability estimates enable the assessment of production performance and the prediction of recovery factor. These estimates are indispensable for reservoir simulation, secondary and tertiary recovery strategies, formation damage analysis, and depth-based production forecasting. Inaccuracies in relative permeability estimates adversely affect resource assessment and prospect development in low permeability reservoirs.

Relative permeability in a pore system depends on the fluid properties, fluid saturations, wettability, and the geometry and connectivity of the pore system. In low-permeability sandstone reservoirs, Shanley et al. (2004) illustrated that both wetting and non-wetting phases can be immobile within a certain saturation range referred to as permeability jail. A common observation in low-permeability reservoirs is a large reduction in hydrocarbon phase permeability in response to a small increase in water saturation for water saturations above 40%.

Core-based estimation of relative permeability in shales will reduce uneconomical drilling, formation evaluation, well testing, and completion practices. An understanding of the relative permeability behavior of shale reservoirs facilitates reservoir surveillance to maximize recovery. There are several reasons for the ‘commonly observed and difficult to explain’ drop in gas production rate of a shale well, which is a consequence of reduction in permeability due to compaction, reduction of gas

relative permeability due to an increase in water saturation (Alfi et al., 2014), or inefficiencies of the installed artificial lift and completion techniques, to name a few. Correlations of relative permeability curves to petrophysical parameters of shale reservoirs will improve production forecast, water management strategies, and identification of "sweet spots" within the reservoir having higher EUR.

Laboratory based techniques to estimate or measure saturation-dependent relative permeability of core samples from unconventional reservoirs are extremely limited in their scope, reliability, and adoption (Dacy, 2010). The existence of nanopores in shales hinders the application of known experimental measurement techniques to obtain relative permeability. High injection pressures, generally around 400 MPa (Klaver et al., 2015), are required for fluid intrusion in all the pores of shale samples. In addition, nanometer-sized pores are susceptible to multiple flow mechanisms arising from slippage and Knudsen diffusion that complicates the permeability estimation from fluid flow experiments on shale samples (Dadmohammadi et al., 2016a & 2016b). Mixed wettability of shale pore system, owing to the presence of both organic and inorganic surfaces (Odusina et al., 2011), also impedes the accurate estimation of relative permeability in shales.

In the absence of direct experimental techniques, numerical simulations have been used to study the significance of relative permeability in shales. A compositional simulation was performed by Khoshghadam et al. (2015) for liquid-rich shales. They assigned distinct Pressure-Volume-Temperature (PVT), relative permeability, and rock compaction characteristics to macropores, nanopores and fractures in the shale. Their work highlights the importance of knowing the pore size distribution in a shale reservoir

to quantify the effect of relative permeability on the EUR estimates. Another noteworthy study done in this regard is that of Alfi et al. (2014). They studied three-phase flow in liquid-rich shale reservoirs based on three-phase relative permeability derived from Stone I model.

Dacy (2010) proposed a laboratory technique to estimate relative permeability curves for sub-microdarcy shales by combining up to seven or more separate core measurements. The proposed method involves measurement of end-point specific permeabilities, end point non-wetting phase trapping capacity, critical gas saturation, and selected number of effective gas permeabilities in different core plugs during both imbibition and drainage. Although experimental work is possible on single phase permeability (Bakshi et al., 2016a; 2016b), direct measurement of relative permeability is not feasible within practical laboratory constraints. Lack of experimental techniques to measure relative permeability in sub-microdarcy rocks necessitates semi-empirical methods. Honarpour et al. (2012) developed relative permeability models for primary drainage process in liquid-rich shales based on the measurements conducted on cores and Lattice Boltzmann flow simulation in the 3D digital pore network generated using pore-level images.

Adsorption-desorption (AD) measurement is primarily used for estimation of pore size distribution (Barrett et al., 1951) and pore connectivity (Seaton, 1991). Yang et al. (2014) performed fractal analysis of adsorption/desorption measurement on 11 shale samples from a Lower Cambrian stratum. Yang et al. (2014) demonstrated that the shale pore structure can be described using the estimated fractal parameters and correlations were observed for TOC, fractal dimension, and adsorption capacity. ADI measurements

on shale samples were interpreted by Kuila and Prasad (2013) using Barett-Joyner-Halenda (BJH) method and density-functional-theory (DFT) to estimate the pore size distribution. Recently, a method for estimation of relative permeability in shales was proposed by Daigle et al. (2015). Daigle et al. (2015) processed the low-pressure nitrogen adsorption/desorption measurements on shales based on effective medium approximation, percolation theory and critical path analysis (CPA) to compute the wetting and non-wetting phase relative permeability curves.

The process of thermal maturation and its impact on pore network has been studied using techniques like Scanning Electron Microscopy (SEM) and gas adsorption. During thermal maturation, first kerogen breaks down into gas and bitumen, followed by the decomposition of bitumen into simpler hydrocarbons (Jarvie et al., 2007). The process is completed with secondary cracking of hydrocarbons into pyrobitumen and coke consisting of mainly carbon. Loucks et al. (2009) observed a positive correlation between the abundance of micropores in organic matter and its maturity due to the decomposition of organic matter and formation of pores during thermal maturation. Curtis et al. (2012) suggested that the thermal maturity and composition of organic matter govern the pore formation during thermal maturation. Conflicting results have been obtained from the studies on the relationship between kerogen maturity and nanopore volume. Ross and Bustin (2009) reported an increase in nano- and micropore volumes in shale samples with an increase in thermal maturity. However, Mastalerz et al. (2013) reported a reduction in total pore volume of shale samples with an increase in vitrinite reflectance, which indicates thermal maturity. An experimental approach to relate the

maturity of organic matter in shale with its pore network will help in economic assessment of shale reservoirs of various maturity windows.

1.2 Modeling of pressure transient response in shale reservoirs with natural fractures using Fast Marching (FM) Method

Characterization of natural fractures is indispensable for evaluation of heterogeneous reservoirs. Low permeability reservoirs utilize hydraulic fracturing to aid economic rates of production and fluid transport. During the process of fracturing, hydraulically induced fractures may interact with natural fractures. This increases stimulated rock volume and the productivity/injectivity of wells. Information on natural fractures in the reservoir facilitates well design and reservoir development (Han, 2011). Orientation and trajectory of wells in naturally fractured reservoirs are aimed at optimizing intersection with high conductivity natural fractures for enhanced exposure to rock volume.

Natural fractures intersecting the borehole are detected in-situ using high-resolution downhole imaging tools. Characteristics of natural fractures can be determined by simultaneous application of various techniques, such as microseismic interpretation, rate transient analysis, mud logging, and borehole images (Bounoua et al., 2008). Microseismic studies are helpful in determining the orientation of fractures (Kilpatrick et al., 2010). Borehole electrical images are used to estimate location, density and average orientation of fractures intersecting the well. Resistivity variation helps to determine fracture aperture, while acoustic images help to distinguish between open and closed fractures. Fracture lengths of intersecting natural fractures can be determined by identifying end of bilinear flow in pressure transient (PT) response.

Vasco et al. (2000) proposed an asymptotic method to model pressure front propagation in reservoir with smoothly varying permeability. The approach is based on Fast Marching (FM) solution of the Eikonal equation formulation of the diffusivity equation. FM method (Sethian, 1996) assumes that the time of arrival of a propagating front at any location depends only on the time of arrival at the adjacent locations and diffusivity along the stencil connecting the nodes. FM method models propagation in heterogeneous reservoirs in fraction of the computation time taken by finite-difference simulations. It can predict the arrival times of the first arrival of propagating front; however, subsequent arrivals need to be accounted into solution for accuracy, especially for seismic applications (Lelièvre et al., 2011).

In reservoir characterization, FM methods have been used to model time-varying drainage volume and PT response. Xie et al. (2012) modeled the PT response in homogeneous and heterogeneous unconventional reservoirs. The solution obtained in fraction of computation time typically required by conventional simulators established the efficiency of FM methods. Zhang et al. (2016) pointed out the similarity between FM and streamline simulation wherein a multidimensional transport/propagation problem is reduced to a single dimensional problem by considering only immediate neighboring nodes when solving for the problem at each node. Owing to the fast computation time, similar to streamline simulation, FM can be used for ranking of large number of realizations obtained during uncertainty analysis of reservoir models (Sharifi et al., 2014). Sharifi and Kelkar (2014) used FM method to rank multiple realizations when performing upscaling of permeability in reservoir models.

1.3 Objectives

Our objective is to process the low-pressure nitrogen adsorption-desorption measurements on shale samples to estimate certain fractal and percolation parameters characterizing the pore network. These parameters are used to estimate relative permeability and residual/irreducible saturations in Wolfcamp, Woodford, Eagle Ford, and Bakken shale samples. We modify the methodology proposed by Daigle et al. (2015) and obtain results for samples of varying thermal maturity. Also, we test the petrophysical correlations between the relative permeability, pore characteristics, maturity, porosity, and TOC for various shale samples. We also present the impact of each parameter on the relative permeability curves with a sensitivity. We investigate the impact of cleaning by organic solvents on the relative permeability behavior in shale samples. This is done by comparing the relative permeability in these samples after and before treating samples to remove bitumen, and soluble hydrocarbons. Additionally, the impact of removal of organic matter by ashing is analyzed. Finally, we correlate the relative permeability curves with production performance using reservoir simulation predictions based on these relative permeability estimates.

To model pressure transient response in shale reservoirs, we first test the accuracy of multistencils fast marching (MFM) simulations of time-varying drainage volume and the ensuing calculations of pressure transient responses of vertical production wells in reservoirs containing various types of natural conductive fractures. Unlike FM algorithm, MFM algorithm considers all 8 neighboring nodes including the diagonal nodes when modeling the propagating front in a 2D reservoir model discretized using square grids. MFM-assisted simulations are validated by applying it on known

reservoir configurations and comparing the predicted responses with those generated using Kappa Saphir commercial simulators. Once the validity of MFM method is established, we investigate the sensitivities of the MFM-generated PT responses to characteristics of conductive natural fractures, such as fracture length, compressibility, orientation, conductivity and volume fraction of natural fractures. The sensitivity studies reveal diagnostic transient signatures that can characterize natural conductive-fracture systems based on pressure transient analysis (PTA). The diagnostic methods developed in this study assume the diffusivity in natural fractures to be within two-orders of magnitude variation from the diffusivity in the reservoir. This limiting assumption makes the natural fracture characterization using PTA a challenging problem to be solved.

CHAPTER 2: METHOD FOR ESTIMATING RELATIVE PERMEABILITY AND PORE NETWORK CHARACTERISTICS

2.1 Laboratory Measurements of Adsorption-Desorption Isotherm (ADI).

In this work, we performed Adsorption-Desorption (AD) measurements on shale samples from various maturity windows of Eagle Ford and Wolfcamp formations. The native shale samples were crushed, and sieved with 35 mesh-size. Subsequently, the samples are oven-dried at 100°C for 24 hours to remove moisture and volatile hydrocarbons. This temperature condition is sufficient to remove the volatile components without affecting the bitumen and kerogen present in the sample. The prepared samples were first exposed to nitrogen gas at continuously increasing discrete pressures in the range of 1.1 psi (~ 2 nm) to 14.7 psi (~ 200 nm) at a constant temperature of 77.4 K to obtain nitrogen gas adsorption isotherm. Once the saturation pressure of 14.7 psi was achieved, the pressure was discretely decreased to obtain the nitrogen gas desorption isotherm. Unlike mercury intrusion porosimetry measurements, the pore structure of the sample is not expected to change during experiment because AD measurements are done at low pressures in the range of 1.1 psi to 14.7 psi. Nonetheless, the shale samples used in our research were crushed and sieved for AD measurements that may have altered the pore connectivity and the pore size distribution.

For each shale sample, we evaluated the mineral composition using transmission Fourier Transform Infrared (FTIR) Spectroscopy, total organic carbon (TOC) content using a LECO™ analyzer, and porosity using Low Pressure Helium Pycnometry (LPP). Adsorption-desorption isotherm measurements were then performed on the samples using a Micromeritics Tristar 3020 gas adsorption analyzer. After the completion of

initial set of measurements, the measured ADI data was processed to estimate the pore size distribution and relative permeability of the shale samples.

2.2 Properties of samples used for this study

Table 2.1 shows the summary of samples used in this study. The Eagle Ford samples from gas and oil window have been ashed before repeating the adsorption-desorption measurement on obtained ashed sample. Similarly, samples from L. Bakken, Wolfcamp, and Woodford have been cleaned using organic solvents before repeating the adsorption-desorption measurement on obtained cleaned samples. Properties measured on native samples have been presented in **Figure 2.1** to show range and variation in these characteristics.

Table 2.1: Petrophysical properties of shale samples studied using the ADI measurements.

	Formation	No. of samples	Formation ID.	Maturity
Dataset-1	Lower Bakken	7	L. Bakken	Early Oil
	Wolfcamp (WF)	10	WF-1	Oil window
		9	WF-2	Condensate
		6	WF-3	Condensate
		5	WF-4	Late Condensate
	Woodford	5	WD	Late Condensate
Dataset-2	Eagle Ford (EF)	9	EF Gas	Gas
		6	EF Oil	Oil
	Wolfcamp (WF)	8	WF Condensate	Condensate

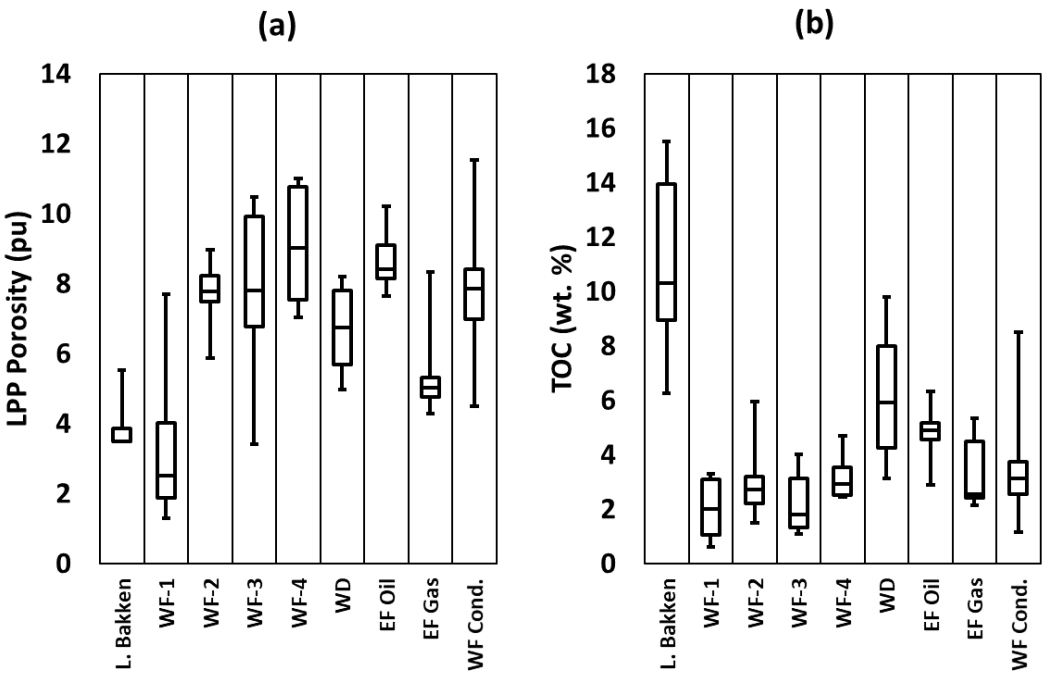


Figure 2.1: Boxplots showing range and variation in measurements made on the samples for (a) LPP porosity (pu), and (b) TOC (wt. %).

2.3 Procedure for cleaning and ashing of samples

For studying the distribution of bitumen and dead oil, crushed samples from Wolfcamp, Woodford and Bakken formations from various maturity windows were treated with 4:1 mixture of toluene and methanol at 110°C for 24 hrs (Sinha, 2017). Following that, we measured and interpreted the ADI measurements on the cleaned shale samples. The advantage of the solvent-extraction process is the low temperature required for this process. Different solvents have different affinity for molecules and hence extract different compounds during the extraction process. The 4:1 mixture of toluene and methanol removes bitumen and dead oil from the crushed shale samples while the insoluble kerogen is left behind. Toluene has the highest yield of extraction after tetrahydrofuran (Nassef et al., 2015) and is much cheaper in comparison. Toluene is useful in extracting aromatic and paraffinic compounds and can decompose the organic

matter in shales. Methanol is primarily used to extract straight-chain unsaturated and saturated hydrocarbons and salt.

For studying kerogen distribution, samples from Eagle Ford oil and gas windows were ashed by exposure to oxygen plasma to remove organic matter. Low Temperature Ashing (LTA) removes organic matter from a sample using activated oxygen (plasma). The removed organic matter could include any hydrocarbons not removed during the oven-drying along with bitumen and kerogen in the samples. Other microstructural impact of ashing include oxidation of pyrites, total/partial dehydration of water-containing minerals (clays), and crystallization of components liberated during ashing (Vassilev and Tascon, 2003). Subsequently, adsorption-desorption measurements were repeated on the ashed samples and these measurements were interpreted to obtain relative permeability estimates for ashed samples.

2.4 Adsorption-desorption isotherm interpretation methodology

The method for interpretation of adsorption-desorption isotherms uses percolation theory, effective medium theory and critical path analysis. Percolation theory defines macroscopic transport properties in terms of statistical transport behavior of connected clusters of microscopic pores. It employs power law formulation that quantifies the probability of connected paths in random systems. It is suitable for systems exhibiting long range connectivity. Percolation theory is invoked to predict the behavior of percolation clusters near percolation threshold where clusters exhibit sharp changes in properties. The sudden change in macroscopic properties can be conveniently described by the power law formulation from percolation theory. Thus, percolation theory is useful in our method for description of the adsorption process with quantification of percolation

threshold and pore network characteristics especially residual/irreducible saturation of the non-wetting/wetting phase. Use of percolation theory lends the non-linear nature of relative permeability curves near the residual/ irreducible saturations. Percolation theory also attempts to correlate macroscopic properties of the system with the pore-level characteristics. Therefore, it works best for narrow pore size distributions.

Effective medium theory defines macroscopic properties in terms of analytical averaging of constituent microscopic properties. It replaces a heterogeneous system with an equivalent homogeneous system. Effective medium theory uses linear scaling to describe gradual changes in system. Effective medium models tend to be erroneous for percolating systems with large range connectivity. Around and beyond percolation threshold, when the system properties show abrupt changes, effective medium theory does not yield desired predictions due to their linear scaling nature. Further away from the percolation threshold, effective medium theory is used for predicting relative permeability behavior of the non-wetting phase which is visible in form of the linear nature of corresponding relative permeability predictions.

Critical path analysis assumes that each pore diameter in the pore network corresponds to a particular value of permeability. Using the estimated pore size distribution along with fractal model, the method correlates between pore characteristics to identify the path of least resistance to flow. CPA is applicable when the range of pore size distribution becomes wide and correlations between pore characteristics become evident. This limits the application of critical path analysis in conjunction with percolation theory for quantifying macroscopic transport behavior. CPA formulates the wetting phase relative permeability curve away from the percolation threshold.

The interpretation methodology for processing the adsorption-desorption isotherm of a shale sample to estimate the relative permeability curves of aqueous and hydrocarbon phases in shales is presented in **Figure 2.2**. Broadly, the interpretation involves three sequential steps:

a) estimation of pore size distribution in the range of 2 nm to 200 nm using BJH method,
b) estimation of fractal and percolation parameters (Z, L, β, D and f_c) using percolation theory which includes application of the universal scaling function and bimodal fractal model, and
c) estimation of relative permeability curves of aqueous and hydrocarbon phases using formulation derived from percolation theory, effective medium theory and critical path analysis.

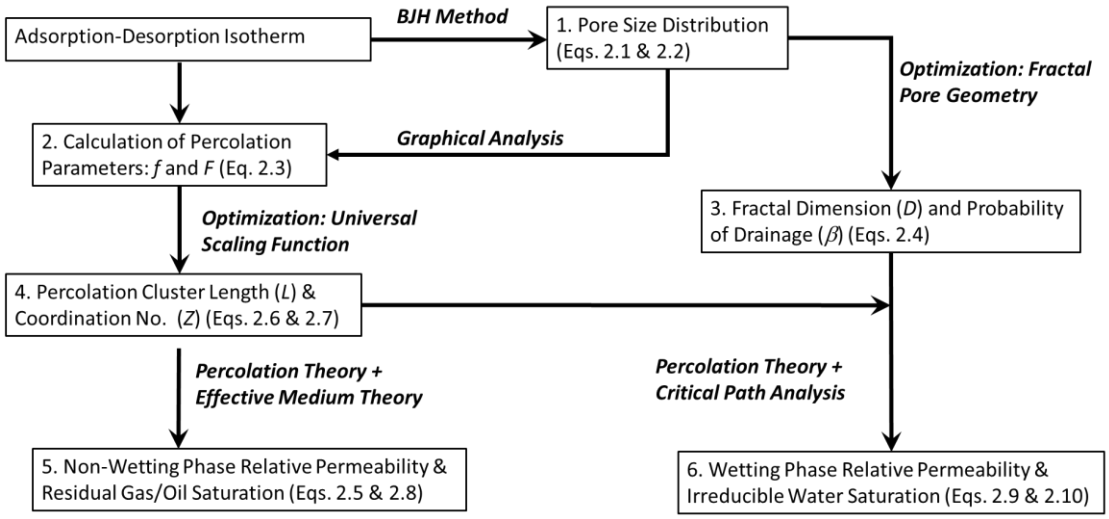


Figure 2.2: Flowchart for ADI Interpretation and relative permeability estimation.

The method has been further explained in Ojha et al. (2017a & 2017b). The results pertaining to pore size distribution and pore network are explained in Ojha et al. (2016, 2017c & 2017d). The impact of these results on relative permeability and production performance has been explained in Ojha et al. (2017e).

2.4.1. Pore size distribution

Pore size distribution (PSD), which includes both pore throat and pore body volumes, can be determined from the adsorption isotherm using several well-established methods that relate condensation pressure to pore size, such as the Kelvin-Cohan equation (Cohan, 1938). In our interpretation methodology, the PSD estimate from adsorption isotherm is used to calculate the percolation and fractal parameters, namely f, D, and β, as shown in **Figure 2.2.**

During an adsorption measurement, nitrogen gas is gradually injected into a sample by increasing the nitrogen gas pressure around the sample. Nitrogen gas adsorbs on the pore walls as mono- and multi-layers until condensation pressure of the injected nitrogen gas is reached. Following that, nitrogen nucleates into liquid phase inside the pores. Nitrogen gas condenses at lower pressures in smaller-sized pores. With gradual increase in pressure during the adsorption measurement, condensation occurs in relatively larger pores. Consequently, the adsorption isotherm data contains information of the pore size distribution of the sample. In contrast, during a desorption measurement, nitrogen gas is gradually withdrawn from the sample by lowering the nitrogen gas pressure around the sample. Volume of liquid nitrogen that remains in the pores at any given pressure during a desorption process is higher than that during an adsorption process due to pore blockage effects. Nitrogen filling the pores that are connected only to smaller-sized pores can desorb and escape only after the evaporation and desorption of nitrogen from the connected smaller-sized pores. Consequently, the hysteresis of adsorption-desorption measurement can be related to the connectivity of the pore network and pore size distribution.

Barrett-Joyner-Halenda (BJH), Dollimore-Heal (DH), and Density-Functional-Theory (DFT) methods are commonly employed to compute pore size distribution from adsorption-desorption isotherm measurements. DFT method is used to calculate PSD from ADI data with an assumption that the distribution of adsorbed fluid over the adsorbent is a function of its density. The equilibrium density of the adsorbed fluid over the adsorbent thus obtained is used to model the adsorption-desorption isotherm. PSD of a sample is estimated by matching the adsorption-desorption isotherm generated using the DFT model with the measured ADI data. In contrast to DFT method, DH and BJH methods employ analytical models that relate the volume desorbed/adsorbed at each pressure decrement/increment to the pore volume associated with the corresponding pore width window by assuming a fixed pore shape, mostly slit or cylinder. The BJH and DH methods are not applicable for pore widths smaller than 7 nm. Average pore size for our samples is in the range of 70-90 nm. Based on the assumed pore shape, both BJH and DH methods have similar approach but assume different constant parameters.

We implemented the BJH method (Barrett et al., 1951) along with the Harkins-Jura thickness equation to compute PSD of shale samples from adsorption isotherm of shale samples. There are several forms of the BJH method in literature; we adopt the BJH method formulation proposed and tested by Kruk et al. (1997, 1999). The thickness equation models the adsorbed nitrogen film thickness, *t*, as a function of relative nitrogen pressure. This corrects the pore radius available for subsequent condensation of nitrogen molecules with change in relative pressure as per the assumed pore geometry. For the PSD estimation, we used the thickness equation and modified Kelvin equation recommended by Kruk et al. (1997). The required α_s values were taken from those given

by Kruk et al. (1999). The calculation was performed in accordance with codes published by Gobin (2006). Kruk et al. (1997) expressed the thickness of adsorbed layer in nm as

$$t = 0.1\left(\frac{60.65}{0.03071 - \log\left(\frac{P}{P_o}\right)}\right)^{0.3968}, \quad (2.1)$$

where P is pressure, P_o is saturation vapor pressure of nitrogen adsorbate (1 atm), and P/P_o denotes relative pressure. This equation provides accurate estimates in the relative pressure range of 0.1-0.95. Kruk et al. (1997) corrected the Kelvin equation using BJH method and expressed the pore radius in which condensation occurs at a given relative pressure in the following form:

$$r = \left(\frac{2\gamma V_L}{RT\ln\left(\frac{P}{P_o}\right)}\right) + t + 0.3, \quad (2.2)$$

where r is the pore radius in nm, V_L is nitrogen molar volume (34.68 cc/mol), $\gamma$is surface tension (8.88 x 10^{-3} N/m), R is universal gas constant (8.314 J/mol/K), and T is the absolute temperature (77 K).

The application of BJH method requires assumption of pore geometry (slit or cylindrical). Based on SEM images of shale pore structure, this assumption may not be valid. Moreover, BJH method is not strictly applicable over the entire range of pore widths. However, it was demonstrated by Kuila and Prasad (2013a) that BJH method provided reasonable estimates of PSD in pore structure of shale and clay samples. The analytical form of BJH method facilitates its application with percolation theory. Kuila and Prasad (2013a) compared results of PSD from DFT and BJH methods for shale samples. They suggested that DFT approach requires assumption of solid-gas

interactions in shale samples which are difficult to validate due to sample heterogeneity. Therefore, application of DFT on these samples would have its own sources of error and application of BJH method is recommended.

A key point to note here is the difference in nitrogen adsorption on the surfaces of organic matter and inorganic content in shale samples. The volume of absorbed nitrogen changes with mineral composition and type of organic matter in various shale samples. Change in thermodynamic interactions between solid-gas molecules is the key premise of DFT method for the estimation of PSD from adsorption measurements on various samples. Although we do not expect gas-solid interactions to remain same for organic matter and inorganics, we assume that the impact of change in interactions is dominated by changes in pore size distribution. Thus, any change in the nitrogen volume adsorbed is a direct consequence of changes in pore size distribution. This allows use of a similar equation for silica and shale samples. This assumption has been reinforced by observations by Kuila and Prasad (2013a) which show that this approach can yield valid estimates for PSD in shale samples.

2.4.2. Percolation parameters: Site Occupation Probability (f) and Percolation Probability (F)

Percolation parameters can be computed from joint interpretation of PSD estimates and the measured ADI data based on Seaton's method (Seaton, 1991). During an adsorption-desorption measurement, shale pore structure is assumed to be composed of connected pores that are filled with either nitrogen vapor and metastable liquid (occupied sites) or condensed stable liquid nitrogen (unoccupied sites). The pores

containing nitrogen vapor are considered as sites in the percolation cluster connected to the external surface. Thus, nitrogen can vaporize during desorption process when it is in an occupied site that is a part of the percolation cluster connected to surface. During the desorption step, the number of occupied sites increases with the decrease in the pressure as a function of pore size distribution and pore connectivity.

Seaton (1991) defined the probability of a pore being occupied by nitrogen vapor and metastable liquid, referred as the site occupation probability, *f*, that is defined as the number of occupied sites divided by the total number of sites. Seaton (1991) showed that *f* can be computed from ADI data as a ratio of number of pores where nitrogen condensation has not occurred to the total number of pores present in the sample. This allows analysis of the adsorption-desorption process using percolation theory. Assuming cylindrical pores with pore radius proportional to length and fractal scaling in the shale sample, *f(P)* can be expressed as

$$f(P) = \frac{\int_{w^*(P)}^{d_{max}} \frac{v(w)}{w^3} dw}{\int_{d_{min}}^{d_{max}} \frac{v(w)}{w^3} dw}, \tag{2.3}$$

where *w*(P)* is the maximum pore diameter in which nitrogen condenses at pressure P, *w* is the pore diameter for cylindrical pores, and *v(w)* is distribution of pore volume as a function of pore diameter, as determined from the PSD estimates. d_{min} and d_{max} are corresponding minimum and maximum pore diameters corresponding to the minimum and maximum relative pressures at which the adsorption-desorption measurements were performed on the samples. Typically, d_{min} will be around 2 nm and d_{max} will be around 200 nm. Ideal fractal objects can follow the relation from zero pore

radius to infinite pore radius but for real samples, the range is restricted by d_{min} and d_{max}. PSD is estimated using the method recommended by Kruk et al. (1997).

Another definition was the probability of a pore being a part of a percolation cluster, referred as the percolation probability, *F*. The *f(P)* needs to be calculated using **Equation 2.3** prior to the calculation of *F(P)*. Seaton (1991) proposed a graphical analysis of adsorption-desorption hysteresis to calculate *F(P).* The ratio *F(P)/f(P)* is the ratio of number of vapor-filled pores in the percolation cluster to the number of vapor-filled and metastable-liquid-filled pores below their condensation pressures. In other words, the ratio *F(P)/f(P)* is equal to the ratio of volume of nitrogen gas that desorb at a given pressure (V_d) and the total volume of nitrogen gas that would desorb at that pressure if all pores had access to nitrogen vapor phase (V_a). The volume V_d can be estimated from the desorption isotherm and V_a can be estimated from the adsorption isotherm at a specific pressure. The contribution of surface clusters, i.e. clusters of vapor-filled pores of limited span only around the surfaces of a sample, to the desorption isotherm is neglected in this approach.

Both the parameters are functions of nitrogen pressure. The parameters help to analyze the adsorption-desorption process using percolation theory. *f* denotes the probability that the pores are occupied by gas which increases with desorption as more liquid nitrogen vaporizes to gaseous state. *F* denotes the probability that these gas pores join to form a continuous spanning cluster. *F* is zero when *f* is below the percolation threshold, f_c which implies that a continuous cluster is yet to form across the pore network. The parameters *F* and *f* increase with a decrease in pressure with more pores being added to the cluster with desorption. *F* tends to *f* as *f* tends to 1 which is a result

that at high site occupation probability, almost all pores are part of the percolation cluster. Estimates of the percolation parameters *f* and *F* of a sample are essential for estimating coordination number (*Z*) and percolation length (*L*) using the universal finite-size scaling function *h*, as described by Seaton (1991). The thermodynamic effects on the hysteresis loop during desorption are neglected in this approach.

2.4.3. Fractal parameters: Fractal Dimension (D) and Probability of Drainage (β)

Fractal dimension (*D*) quantifies the complexity of a pattern in terms of the change in detail to the change in scale. *D* describes the self-similar scaling of a porous medium. Perfect (2005) defined probability of drainage (*β*) is the ratio of pore volume to the sum of pore and solid volumes in a repeating fractal model (Ghanbarian-Alavijeh & Hunt, 2012). A unimodal model for fractal pore size distribution is an ideal approach that may break down for real samples. A bimodal approach tends to be a closer approximation. Moreover, bimodal approach is convenient in implementation compared to a trimodal approach. Therefore, we have used the bimodal approach for sample analysis presented in this paper. From Hunt et al. (2013), the bimodal approach requires two values each for *D* and *β*. In this approach, the cumulative volume distribution of pore sizes, *θ(d),* is defined as

$$\theta(d) = \begin{cases} \varphi_1(d), & d_{min} < d < d_x \\ \varphi_1(d_x) + \varphi_2(d), & d_x < d < d_{max} \end{cases} \tag{2.4}$$

where $\varphi_1(d) = \beta_1 \left[\left(\frac{d}{d_x}\right)^{3-D_1} - \left(\frac{d_{min}}{d_x}\right)^{3-D_1} \right]$ and $\varphi_2(d) = \beta_2 \left[\left(\frac{d}{d_{max}}\right)^{3-D_2} - \left(\frac{d_x}{d_{max}}\right)^{3-D_2} \right]$

Here d_x is the pore diameter at which pore behavior changes from the fractal regime 1 to fractal regime 2 and D_1, β_1, D_2, and β_2 are the fractal dimension and

probability of drainage for respective fractal regimes. d_{min} and d_{max} are minimum and maximum pore diameters in samples influencing the adsorption-desorption isotherm.

The values of d_x, β_1, D_1, β_2 and D_2 are computed using an optimization algorithm implemented in MS-Excel toolbox involving following steps:

1. Assume an initial guess of d_x, such that $d_{min} < 10$ nm $< d_x < 100$ nm $< d_{max}$.
2. For the chosen value, use optimization algorithm to estimate β_1 and D_1 for regime-1 and β_2 and D_2 for regime-2 that generates the best match between $\theta(d)$ predicted by **Equation 2.4** and the PSD estimated from AD measurement using BJH method.
3. Change the value of d_x.
4. Repeat steps 2 and 3 to find the global optimum solution of d_x and corresponding values of β_1, D_1, β_2 and D_2.

2.4.4. Percolation parameters: Percolation cluster length (L) and coordination number (Z)

Coordination number (Z) is the number of immediate neighbors of each pore in the pore structure. An increase in coordination number results in a decrease in the percolation threshold. Percolation cluster length (L) is the size of pore network in terms of number of pores contained in the network. Average pore length in a microparticle can be approximated as the size of microparticle divided by L. The parameter L is used as a qualitative check for the estimated properties of the pore networks of the sample. The parameters Z and L are obtained by using an optimization algorithm on the universal scaling function proposed by Seaton (1991) expressed as

$$L^{\frac{b}{\nu}} ZF = h\left([Zf - Zf_c]L^{\frac{1}{\nu}}\right), \tag{2.5}$$

where

$$h(x) = 9.753\ sin(0.04046x + 0.2653)\ +\ 2.253\ sin(0.4244x - 1.972) + \ 2.072\ sin(0.4495x + 0.8723), \quad (2.6)$$

based on the expression presented by Daigle et al. (2015), b=0.41 (universal value), v=0.88 (universal value), and f and F are percolation parameters. The parametric value of Zf denotes an average number of occupied bonds per site at a given site occupation probability, f. The proposed optimization method to estimate Z and L requires $f(P)$ and $F(P)$ values estimated for relative pressures of the nitrogen gas greater than 0.45.

The behavior of percolation near the percolation threshold is dependent on the size of the system. For an ideal infinite system, the f value changes instantaneously once the percolation threshold is achieved. For any finite cluster, the parameters show a gradual change near the percolation cluster. The universal scaling function defines the effect of size of system on the behavior of parameters near the percolation threshold. The function is universal in form which changes with nature of pore lattice. The function defines the expected behavior of the percolation clusters which helps to model the adsorption phenomenon to find coordination number and percolation cluster length.

The parameter Z is used to compute the bulk volume of a fluid phase at which the pore structure of the porous media changes from percolation scaling to effective medium scaling, denoted as θ_x, that was expressed by Sahimi (1993) as

$$\theta_x = \ \theta_t + \frac{\varphi}{Z}, \quad (2.7)$$

where φ is the ADI porosity of the sample obtained by multiplying the cumulative pore volume from calculated pore size distribution at nitrogen saturation pressure with bulk density of the sample, and $\theta_t = f_c * \varphi$ is the critical phase content for percolation, where f_c is the percolation threshold that describes the critical value of occupation probability at which the cluster percolates across the medium and attains infinite length.

The optimization algorithm is designed to find the values of *Z* and *L* for a given *f, F, b,* and *v* that satisfies the universal scaling function expressed as **Equation 2.5**. **Equation 2.6** was obtained through curve fitting the simulation results of a 3D percolation cluster model. As the first step of the optimization, initial guesses of *Z* and *L* are used to calculate $x = [Zf - Zf_c]L^{\frac{1}{\nu}}$and $y = L^{\frac{b}{\nu}}ZF$. To improve the robustness of the optimization, rather than estimating f_c as the third unknown parameter, we express f_c as a function of *Z,* given as $f_c = 1.7259Z^{-1.081}$, which is calculated as a regression on the typical values of coordination number and corresponding percolation thresholds for various lattice structures, as presented by Seaton (1991). The second step of optimization involves iterative modification of the values of *Z* and *L* to minimize the error between *h(x)* and *y*.

Our interpretation methodology involves two separate optimization procedures: one for β and *D*, and another for *Z* and *L*. The algorithm implemented in the optimization procedure is not significant as long as it converges to the global solution. We confirmed the uniqueness of the optimal solution against 2D contour plots of errors involved in the solution space of the optimization problem for β and *D* and those for *Z* and *L*.

2.4.5. Relative permeability of non-wetting phase

Several authors have demonstrated that percolation theory can predict transport properties of fluid-filled porous media (Ghanbarian et al., 2014 & 2015). We assume that the transport behavior of the non-wetting phase can be holistically predicted using percolation theory and effective medium theory. It is assumed that percolation theory best predicts the transport properties of the fluid phase for small volume fractions of that

phase (θ_i) close to the critical phase content (θ_t), whereas effective medium theory provides the best approximations for the transport properties of the fluid phase for volume fraction of that phase much above the critical phase content (Daigle et al., 2015). The volume fraction of the fluid phase at which percolation scaling switches to effective medium scaling is denoted as θ_x, as described in **Equation 2.7.** Relative permeability of the non-wetting phase at non-wetting phase volume fraction of θ_{nw} is expressed as

$$k_{rnw}(\theta_{nw}) = \begin{cases} \dfrac{(\varphi - \theta_t)(\theta_{nw} - \theta_t)^2}{(\theta_x - \theta_t)(\varphi - \theta_t)^2}, & \theta_t < \theta_{nw} < \theta_x \\ \dfrac{(\theta_{nw} - \theta_t)}{(\varphi - \theta_t)}, & \theta_x < \theta_{nw} < \varphi \end{cases} \tag{2.8}$$

2.4.6. Relative permeability of the wetting phase

We assume that the saturation-dependent transport behavior of the wetting phase can be formulated using percolation theory and critical path analysis (CPA). The transport properties of the wetting fluid phase for volume fraction of that phase much above the percolation threshold can be best approximated using CPA (Daigle et al., 2015). CPA proposes that fluid flow in a highly heterogeneous porous media is dominated by pore throats whose radii are slightly greater than the critical radius (Ghanbarian et al., 2016); therefore, it expresses the pore-size dependence of permeability. The percolation threshold for wetting and non-wetting phases are assumed to be equal. The equation for relative permeability can be derived by applying Poiseuille's law to an assumed fractal porous media. From Hunt et al. (2013), relative permeability of the wetting-phase at wetting phase volume fraction of θ_w is expressed as

a) $\theta_t < \varphi_1$

$$k_{rw}(\theta_w) = \begin{cases} \left[\frac{\beta_1 - \varphi + \theta_w - \theta_t}{\beta_1 - \theta_t}\right]^{\frac{3}{3-D_1}}, & \theta_w - \theta_t > \varphi_2\,, \theta_w > \varphi_2 \\ \left(\frac{\beta_1^{\frac{3}{3-D_1}}}{\beta_2^{\frac{3}{3-D_2}}}\right)\left(\frac{\beta_1 - \varphi}{\beta_1}\right)^{\frac{3}{3-D_1}}\left[\frac{\beta_2 - \varphi_2 + \theta_w - \theta_t}{\beta_1 - \theta_t}\right]^{\frac{3}{3-D_2}}, & \theta_w - \theta_t < \varphi_2\,, \theta_w > \varphi_2\ . \end{cases} \quad (2.9)$$

b) $\theta_t > \varphi_1$

$$k_{rw}(\theta_w) = \left[\frac{\beta_2 - \varphi_2 + \theta_w - \theta_t}{\beta_1 - \theta_t}\right]^{\frac{3}{3-D_2}}\ . \quad (2.10)$$

According to the bimodal approach used in our method, the total ADI porosity (φ) is divided in two components (φ_1 and φ_2), each calculated as a separate fractal regime. This division leads to the following two scenarios:

1. $\theta_t < \varphi_1$: Percolation can occur in both fractal regimes and therefore the scaling is dependent on parameters from both fractal regimes. The $\theta_w - \theta_t > \varphi_2$ indicates θ_w is away from the point of change of fractal regime, whereas $\theta_w - \theta_t < \varphi_2$ indicates θ_w is near the point of change of fractal regimes and percolation characteristics is simultaneously affected by fractal parameters of both regimes.
2. $\theta_t > \varphi_1$: Percolation occurs entirely in the 2nd fractal regime and therefore is only dependent on fractal parameters of the 2nd fractal regime.

The following conditions are required for applying critical path analysis (CPA) to fluid transport:

1. CPA was derived to model transport in random systems with broad distribution of conductance based on the dominance of a controlling conductance of a critical magnitude.

2. It is observed that CPA predictions are good for small coordination numbers, likely characteristics of sedimentary rocks, and a limited range of pore size distribution.
3. Application of CPA to predict permeability assumes equivalence of permeability with electrical conductance. This assumes the same critical pore size for both electrical conductivity and permeability. When surface conductance has significant contribution to electrical transport, it leads to differences in critical radius for conductance and permeability. This requirement for the applicability of CPA is strictly valid for samples with negligible surface conductance (Daigle, 2016) that may breakdown in presence of clays, conductive minerals, and nanoscale pores.
4. Daigle (2016) states that CPA is applicable for PSD varying 2.5 to 3.5 orders of magnitude based on their investigations on pore sizes ranging from 0.9 nm to 1000 nm. Samples studied in our paper exhibit PSDs varying between 2.3 to 2.5 orders of magnitude for pore sizes in the range of 2 nm to 200 nm, as sensed by the phenomena of adsorption and desorption.

2.4.7. Relative diffusivities of wetting and non-wetting phases

Transport of a fluid phase in shale has Darcy (including slip flow) component and diffusive component. Both the components of transport are saturation dependent. Therefore, the concept of relative permeability and relative diffusivity needs to be invoked to characterize the saturation dependence of the two components of flow in shales. Sections 2.4.5 and 2.4.6 describe the formulation of relative permeabilities of wetting and non-wetting phases, which is associated with the Darcy component of flow. For the non-wetting fluid phase, Ghanbarian et al. (2014) demonstrated that the formulation of diffusion coefficient of charge carriers is analogous to that of electric

conductivity. Martys (1999) showed using lattice Boltzmann method that diffusion coefficient of charge carriers in non-wetting phase followed percolation theory and could be expressed using a scaling function, which is similar to that obtained by Ghanbarian et al. (2014). A polynomial scaling between charge carrier diffusion coefficient and electrical conductivity was recommended the by Martys (1999) for the wetting phase. These observations in the domain of electrical conduction and diffusion can be extended to relate relative diffusivity and relative permeability of the non-wetting phase. Daigle et al. (2015) proposed that relative diffusivity of non-wetting phase can be expressed using a formulation analogous to the relative permeability of the non-wetting phase. This was based on experimental data published by Springer et al. (1998). In our interpretation methodology, we assume that relative diffusivity formulations for non-wetting phase are analogous to the relative permeability formulations for non-wetting phase. Consequently, our investigation of saturation-dependent transport properties does not need to explicitly account for both relative diffusivity and relative permeability for non-wetting phase.

The mean free path of water molecules in liquid phase would always remain very small compared to pore diameter. The Fick's diffusion coefficient for water in liquid phase is 3-4 orders of magnitude smaller compared to that in gas phase. As a result, diffusion for liquid phase is not likely to play an appreciable role in transport phenomena. Hence, we assume that advection is the dominant mode of transport in wetting aqueous phase and diffusion can be neglected without compromising on accuracy of predictions for wetting aqueous phase. These assumptions allow us to account for relative diffusivity and relative permeability for non-wetting phase using a single expression whereas relative diffusivity for wetting phase can be neglected.

2.4.8. Improvements implemented in the proposed methodology compared to earlier methodologies

Following are few key improvements in the methodology used for this analysis:

1. We replaced the unimodal fractal model used by Daigle et al. (2015) with a bimodal fractal model, mentioned in **Equation 2.4**, to derive fractal parameters from the computed PSDs. Pore size distribution exhibited by the samples under our investigation are multimodal in nature; consequently, an analysis with unimodal fractal model may not be reliable. We realize that even the bimodal model may not be sufficiently accurate to describe the computed PSDs. We are not aware of any multimodal fractal model that can used for the PSD analysis required for the proposed methodology.
2. Use of bimodal fractal distribution necessitates reformulation of the wetting phase relative permeability, mentioned in **Equations 2.9 and 2.10**, which is significantly different from the one used by Daigle et al. (2015).
3. For calculation of wetting phase relative permeability, Daigle et al. (2015) combined both critical path analysis and percolation theory by defining a crossover fraction θ_d. This could be done because they assumed a unimodal fractal model. On the other hand, we are using critical path analysis for the wetting phase and assume a bimodal fractal model that does not require calculation of a crossover fraction, similar to Hunt et al. (2013).
4. The formulation of **Equation 5** mentioned in Daigle et al. (2015) was modified based on Sahimi (1993) to obtain the new formulation mentioned in **Equation 2.7** in our

paper, which accurately describes the crossover point between percolation theory and effective medium theory.

5. Instead of $f_c = 1.5/Z$ used by Daigle et al. (2015), we use $f_c = 1.7259Z^{-1.081}$ for the correlation between percolation threshold and coordination number. The correlation is based on the published values of numerical simulation results obtained by Seaton (1991).
6. Daigle et al. (2015) separately defines the relative permeability of non-wetting phase due to diffusion and that due to advection using Equations 7 and 8 in that paper, and later combines them to calculate the relative permeability of the non-wetting phase. However, the two aforementioned relative transport models are based on the same formulation of percolation theory; therefore, the two formulations become redundant. We eliminate this repetition as it is not required from the point of view of a relative transport model for shale.

2.4.9. Method Validation

2.4.9.1. Validation of Method to Estimate PSD

The nitrogen adsorption data and pore size distribution results published by Kruk et al. (1997, 2000) and Liu et al. (1992) have been analyzed for purposes of validation. Kruk et al. (1997) used a modified Kelvin equation on ADI measurements on MCM-41 siliceous molecular sieves and macro-porous silica gel. Kruk et al. (2000) used the formulation given by Kruk et al. (1997) to process the ADI measurements on SBA-15 ordered mesoporous silica. Similarly, Liu et al. (1992) modified the method proposed by Seaton (1991) to interpret the ADI measurements on numerous silica samples. All the authors assumed cylindrical or slit pore geometry and used variations of BJH method to

calculate the pore size distribution. The choice of the thickness equation does not alter the estimates as long as the same equation is applied consistently on the entire set of samples (Kuila and Prasad, 2013a).

Figure 2.3 compares the *dV/dR* estimates obtained by Kruk et al. (1997), Kruk et al. (2000) and Liu et al. (1992) with those obtained using the PSD estimation method described in Section 3.1. The *dV/dR* denotes the slope of the cumulative pore volume curve, i.e. incremental pore volume, when plotted against pore diameter. The authors recognize that the nature of the curves will be different for plots of *dV/dR* or *dV/dln R* (Meyer and Klobes, 1999) that will not affect the conclusions based on the type of plot. The plots are presented for *dV/dR* to maintain similarity with the original published literature.

The range of estimated pore diameter exhibits a good match for the three cases but the volumetric results are different. The volumetric disparity between the previously published and newly calculated results should be due to difference in the values assumed for conversion constants, namely V_L, γ and α_s. The α_s values are needed to convert the measured nitrogen gas volume to required liquid nitrogen volume adsorbed at each pressure step and remains constant for each pressure step. Since any alternate reference for α_s values deemed fit for use in shale samples is not available, we have used the only available values but are aware that these values may introduce some error in interpreted PSD. Introduction of error at this stage would result in deviation of interpreted PSD and pore coordination number from actual values but is not likely to introduce much error in relative permeability estimates. **Figure 2.3c** appears noisy due to use of higher number of points as compared to **Figures 2.3a** and **2.3b**. If number of points is decreased, noise

can be reduced although the overall nature of the curve needs to be preserved in each case.

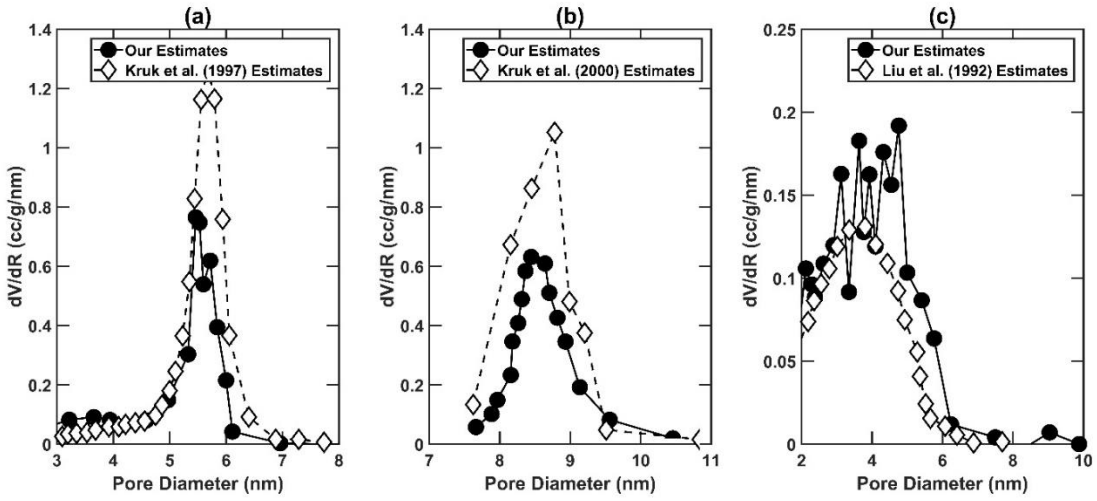


Figure 2.3: Comparison of the estimated PSDs against those published by (a) Kruk et al. (1997) for MCM-41 sample presented in Figures 2 and 8 of the referenced literature, (b) Kruk et al. (2000) for S4 sample presented in Figures 4 and 5 of the referenced literature, and (c) Liu et al. (1992) for Sample A presented in Figures 1 and 4 of the referenced literature.

2.4.9.2. Validation of Method to Estimate F(P) and f(P)

PSD estimates for a sample is used to calculate *F(P)* and *f(P).* **Figure 2.4** compares *F(P)* vs. *f(P)* plots obtained by Liu et al. (1992) against those obtained by using the method described in **Section 2.4.2**. Liu et al. (1992) used adsorption data on silica samples to which they applied the BJH method separately assuming cylindrical and slit pore geometry. Our assumptions of pore geometries are similar to those used by Liu et al. (1992) for processing the ADI measurements using a modified BJH method, as recommended by Kruk et al. (1997). In **Figure 2.4**, the point where *F* equals *f* is a qualitative indicator of the coordination number of pore network (Seaton, 1991). The point where *F(P)=f(P)* is indicative of the point of closure of the hysteresis loop in adsorption-desorption isotherms which is consistently correlated with the coordination

number of pore structure. The *f* value corresponding to smallest positive value of *F* is indicator of percolation cluster length. For small clusters (L<10), this *f* value is close to 0. For an ideal cluster of infinite length, this *f* value will be equal to the percolation threshold. This is representative of the percolation phenomenon for which flow happens only when the cluster percolates and achieves infinite size.

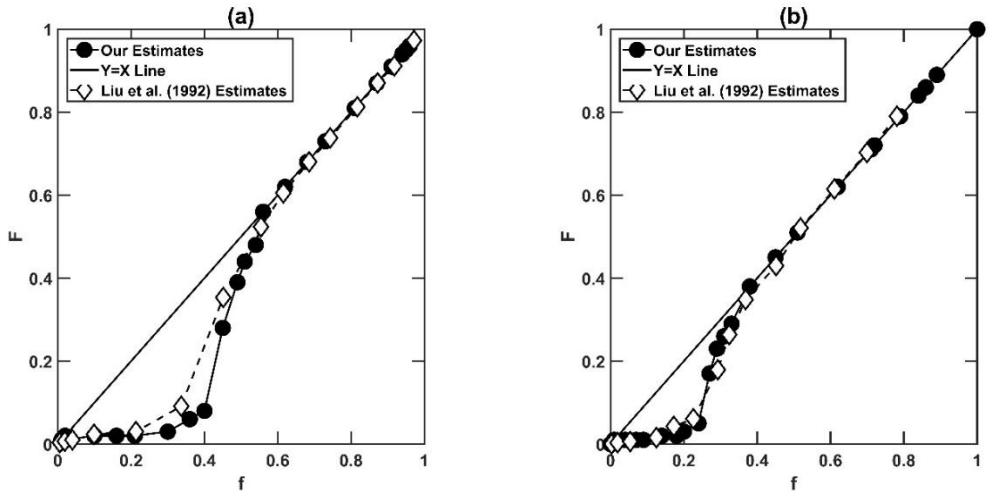


Figure 2.4: Estimated *F(P)* vs. *f(P)* plots against those published by Liu et al. (1992) for (a) cylindrical pore geometry (b) slit pore geometry. The sample referred here is Sample-A with data shown in Figures 1,4, and 6 of the referenced literature.

2.4.9.3. Validation of Estimations of Z and L

Z and *L* estimates were obtained using an optimization algorithm that requires *f(P)* and *F(P)* as inputs. We compare the *Z* and *L* estimates published by Liu et al. (1992), Liu et al. (1993), and Liu and Seaton (1994) against those estimated using our optimization procedure on the corresponding published data. The authors adsorption measurements on silica samples. The authors presented the *f(P)* and *F(P)* curves derived from the AD measurements. These curves were then used to estimate the *Z* and *L* of the samples. We apply our optimization procedure on the published data and curves to compute the *Z* and *L* values. **Table 2.2** shows a good agreement between the estimated

and published Z estimates. The published L values were higher than our estimates, as reported in **Table 2.2**. Our estimation is based on the universal scaling function described in **Equations 2.5** and **2.6**. Liu et al. (1992), Liu et al. (1993), and Liu and Seaton (1994) replaced parameters F and f with accessibility functions (X^P and X). The accessibility functions have the same physical definition and calculation procedure as F and f defined earlier. The accessibility functions were used to estimate Z and L by matching the calculated accessibility functions with those obtained by Monte-Carlo simulations of percolation for different values of L. Procedure used by Liu et al. (1992) assume $10 < L < 60$, which is not valid for our method that assumes $L < 12$, which is chosen to be less than 12 to speed up the calculation for finding the global optimum solution within the chosen solution space. Upon increasing the upper limit of L to 60 in the proposed optimization method, we observed that the accuracy of Z and L estimates are unaltered though the time to converge to an optimal solution increased. The L estimates directly influence the accuracy of Z, other than that there is not any quantitative application of the L estimates in the entire interpretation methodology.

Table 2.2: Comparison of estimated and published Z and L estimates

Reference	Estimated Z	Published Z	Estimated L	Published L
Liu et al. (1993)*	2.9	3	-	-
Liu et al. (1993)*	4.9	5.1	5.1	4.3
Liu et al. (1992)- Sample 1 (Cylindrical)	5.3	5.1	5.7	43
Liu et al. (1992)- Sample 1 (Slit)	3.6	3.7	5.2	50
Liu and Seaton (1994)- Sample A	5.0	4.7	3.3	12

* The samples referred here are presented in Figures 6 and 7 of the referenced literature.

2.5 Assumptions made in the approach

1. We assume that the PSD estimation from BJH method is representative of shale samples. This is in line with demonstrations made by Kuila and Prasad (2013a), wherein the PSD estimates obtained using DFT method were significantly different from those obtained using BJH-type methods.
2. We assume that shale pore structure can be accurately defined by a single value of coordination number (Z) which can be found using the universal scaling function. This assumption is strictly valid only for unimodal samples.
3. We assume that a bimodal fractal model can accurately match the PSD of shale samples used in the study.
4. We assume that in each case of optimization used in the method, the result refers to the global solution of the optimization problem. The estimates β and D strongly depend on d_x. Therefore, it is very important to identify the true global optimum solution of d_x.
5. The method assumes water to be wetting phase for shale samples and hydrocarbon is assumed to be wetting to organic matter.
6. We assume that relative diffusivity formulations for non-wetting phase are analogous to the relative permeability formulations for non-wetting phase. Consequently, the scaling formulation based on percolation theory can holistically predict transport in shale samples.
7. The method assumes equivalence of permeability with electrical conductance. This assumes the same critical pore size for both electrical conductivity and permeability and negligible impact of surface pores on transport properties.

2.6 Limitations of the approach

1. PSD estimation from low-pressure nitrogen gas adsorption measurements is applicable up to a maximum pore width of 200 nm (Kuila and Prasad, 2013b) and minimum pore width of 7 nm. The relative permeability results based on adsorption measurements need to be considered in conjunction with those obtained from other methods, such as mercury intrusion, to include pores beyond the range of width spanned by the AD measurements.
2. The method assumes water to be wetting phase for shale samples and hydrocarbon is assumed to be wetting to organic matter. This assumption needs to be further tested to ensure the reliability of the method.
3. **Equation 2.5** and the assumption of a universal scaling function to find *Z* and *L* is theoretically applicable only for unimodal pore size distributions. In absence of any substitute method to find *Z* and *L* for practical materials with bimodal and trimodal PSDs, we adopt the procedure developed for unimodal distribution.
4. The universal scaling function method generates reliable results for H1 and H2 hysteresis loops only. We observe H3 hysteresis loops in our samples.
5. The *L* estimates obtained from optimization on the universal scaling function differ from those obtained in other published results. This shows that the method is not very sensitive to variation in *L* values.
6. Analytical form of *h(x)* proposed in **Equation 2.6** is not a unique relationship, it was estimated by analytically approximating the simulation results for $L^{\frac{b}{\nu}}ZF$ versus $[Zf - Zf_c]L^{\frac{1}{\nu}}$.

7. An inherent limitation of **Sections 2.4.4** and **2.4.5** is the inability to set bounds on the upper limit of θ_x value because all values of Z theoretically are allowed for the equations mentioned in these sections. This keeps the method open to the possibility of having values such as $\theta_x > \varphi$ for low values of *Z*. In these circumstances, **Equations 2.8, 2.9 and 2.10** may yield inconsistent relative permeability curves.
8. The relative permeability curves generated are equivalent to normalized relative permeability curves since they always predict values ranging from 0 to 1. Further experimental measurements would be required to have the actual relative permeability predictions at maximum saturation of corresponding phase.

CHAPTER 3: ESTIMATION OF PORE NETWORK CHARACTERISTICS

3.1 Estimation of pore size distribution(PSD) and associated characteristics

We define ADI pore volume (APV) as the cumulative volume of nitrogen adsorbed on the grain surfaces of 1 gram of sample at the saturation pressure of nitrogen. **Figure 3.1** shows the incremental and cumulative pore size distributions in the pore size range of 2 nm to 200 nm for dataset-1 mentioned in **Table 2.1** containing shale samples from oil-, condensate-, and late-condensate-window of thermal maturity. For most samples, the PSD is multimodal with peaks visible around 15, 35 and 110 nm. The relative contribution of pore sizes varies with thermal maturity. WF-4 and WD samples show higher contribution from pore size peaks around 15 nm. Except for L. Bakken samples, the cumulative and incremental PSDs tend to increase with increasing thermal maturity. High TOC in L. Bakken samples may be the reason for this discrepancy.

Figure 3.2 shows the incremental and cumulative PSDs for dataset-2 mentioned in **Table 2.1** containing samples from oil-, condensate-, and gas-window of thermal maturity. Unlike dataset-1, these samples do not show a definite correlation between adsorption-desorption-isotherm pore volume (APV), which is the total volume of pores of size between 2 nm and 200 nm, and thermal maturity. Eagle Ford oil- and gas-window samples show similar PSDs. The Wolfcamp samples in this dataset exhibit a dominant peak in pore size around 50 nm. The cumulative pore volume of Wolfcamp condensate-window samples exceeds that of Eagle Ford gas-window samples. Difference in kerogen properties and variation in maturation history could be potential reasons for these

observations. Except the Wolfcamp samples in this dataset, all samples exhibit similar features and petrophysical trends in PSD to those observed for samples in dataset-1.

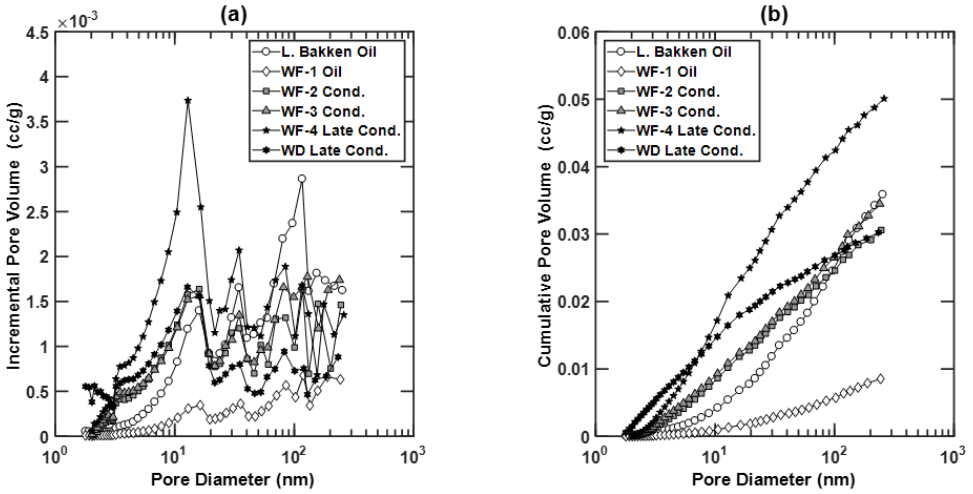


Figure 3.1: (a) Incremental pore size distribution, and (b) cumulative pore size distribution for samples from different thermal maturity windows from Bakken, Woodford and Wolfcamp formations.

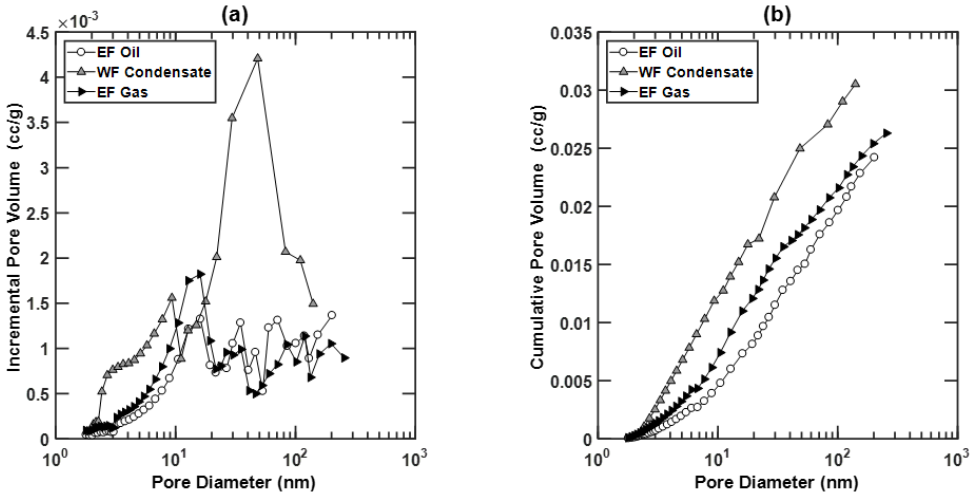


Figure 3.2: (a) Incremental and (b) cumulative pore size distributions for samples from different thermal maturity windows of Eagle Ford (EF) and Wolfcamp (WF) formations.

3.2 Correlations of APV and average pore diameter with LPP Porosity and TOC:

Crossplots between LPP porosity (in porosity units, p.u.) before cleaning and ADI pore volume (APV, in cc/g) for native (**Figure 3.3a**) and cleaned samples indicate the abundance of nano- and micropore volumes smaller than 200 nm. APV varies linearly with LPP porosity of the samples. APV and LPP porosity of samples increase with sample maturity. These trends indicate that a higher LPP porosity is related to larger connected nano- and micropore volumes for adsorption of nitrogen. These observations match with the linear relationship between surface area calculated from ADI experiments and total porosity for Devonian-Mississippian shale samples reported by Ross and Bustin (2009). They also reported that at higher thermal maturity, organic matter is transformed by diagenesis to create more microporosity, which can be detected using AD measurements due to higher number of sites for adsorption of nitrogen. Overall, samples exhibit positive correlations between APV, LPP porosity and maturity.

The crossplots between total organic content (TOC) before cleaning and APV for native samples (**Figure 3.3b**) indicate the abundance of nano- and micropore volumes smaller than 200 nm in the organic matter. Similar response is seen in cleaned samples. L. Bakken samples exhibit considerably higher TOC compared to other samples but show no commensurate increase in APV. This indicates that the maturation resulted in production of larger sized pores that are not observable using the AD measurements. WF-4 samples are the highest maturity samples; nonetheless, they exhibit low TOC and corresponding low APVs. Samples from other formations have TOC in the range of 2-4 wt. % and exhibit positive correlations between APV, TOC and maturity.

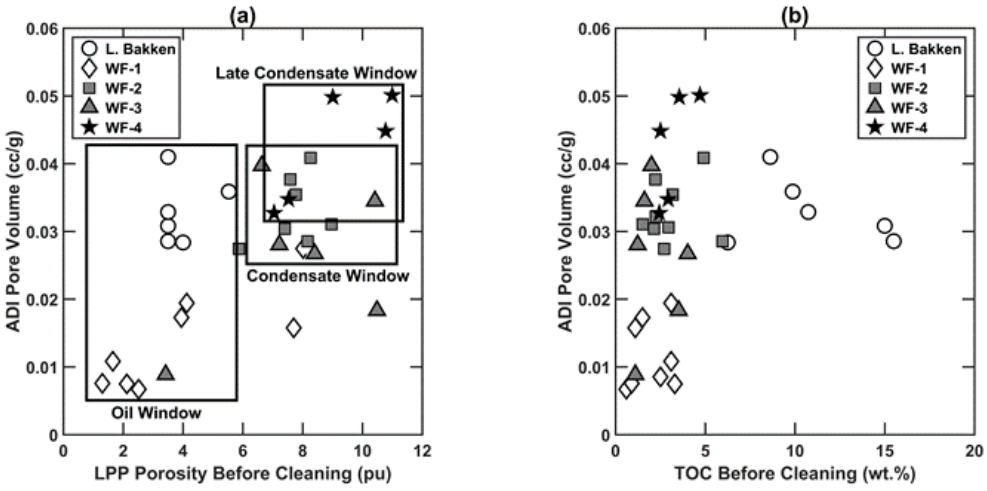


Figure 3.3: Crossplots of (a) LPP porosity before cleaning versus ADI pore volume, and (b) TOC before cleaning versus ADI pore volume for native samples from various maturity windows.

Figure 3.4 shows the relationship between average pore diameter and APV for both native and cleaned samples. We assumed cylindrical pore geometry to compute the pore size distribution of a sample from its ADI measurement. The average pore diameter was calculated as an incremental pore volume weighted average over the entire pore size distribution from 2 nm to 200 nm. In **Figure 3.4**, the average pore diameter of samples decreases with increasing thermal maturity, despite the increase in APV with maturity. This indicates an increase in number of nanopores and micropores for both native and cleaned samples with increase in thermal maturity. Similar observations were made on shale samples from North American basins by Valenza et al. (2013), more micropores were generated during the thermal maturation of organic matter. Higher number of micropores leads to considerable increase in surface area for adsorption. Valenza et al. (2013) explained that the increase in volume with increase in maturity is not as high as the increase in surface area for the studied shale samples. Average pore diameter can be

expressed as $d=8V/A$, a higher increase in surface area compared to the volume will lead to the decrease in average pore diameter, which is in good agreement with our observations.

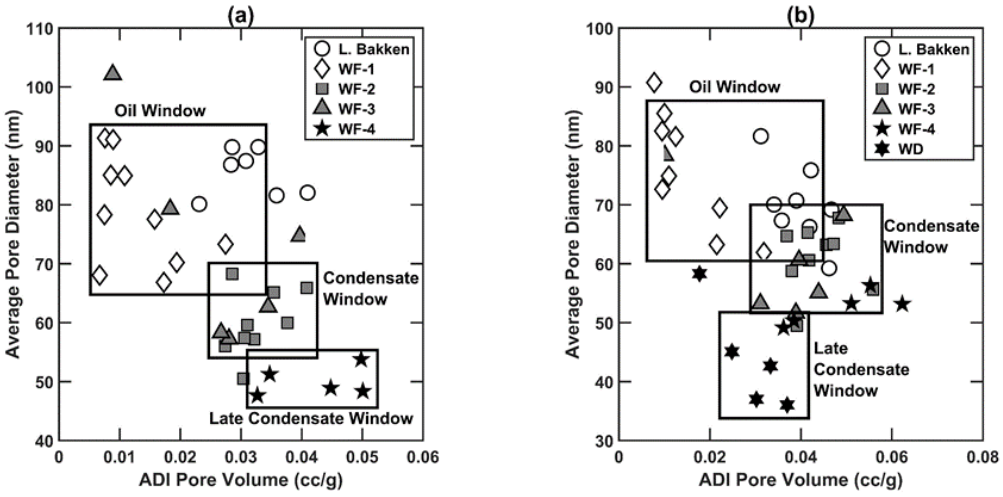


Figure 3.4: Crossplots of average pore diameter versus APV for (a) native samples, and (b) cleaned samples from various maturity windows.

3.3 Impact of Cleaning and Ashing

3.3.1. Impact on PSD and associated parameters

Figure 3.5a shows that the Low Temperature Ashing (LTA) leads to an overall increase in the ADI porosity due to the removal of organic matter. Despite the low bulk porosity of gas-window samples, the net increase in ADI porosity of gas-window samples due to ashing is comparable to that of the higher porosity oil-window samples. The figure indicates that the change in ADI porosity due to ashing is independent of the LPP porosity before ashing. Both oil- and gas-window samples exhibit a physically consistent linear relationship between the change in ADI porosity due to ashing and TOC before ashing, as depicted in **Figure 3.5b**. Also, based on the observed linear trends in **Figure 3.5b**,

gas-window samples exhibit a higher change in ADI porosity due to ashing than oil-window samples, which indicates that the organic matter in gas window samples is present in micro- and mesopores.

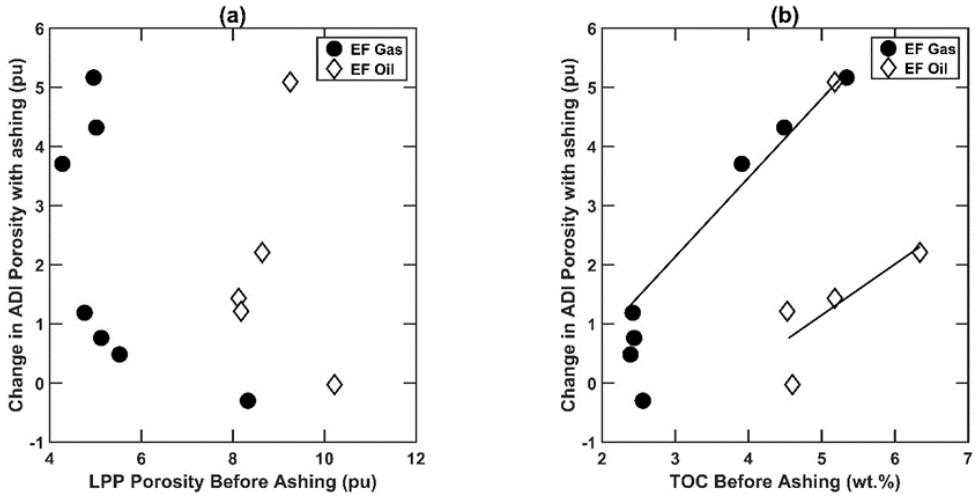


Figure 3.5: Crossplots of (a) change in ADI porosity due to ashing versus LPP porosity before ashing and (b) change in ADI porosity due to ashing versus TOC before ashing of samples from gas and oil windows.

Figure 3.6 has average pore diameters of native samples on X-axis and those of cleaned and ashed samples on Y-axis. The $Y=X$ line demarcates the region for which the samples do not exhibit appreciable change in average pore diameter upon cleaning and ashing. Except for L. Bakken samples, none of the samples show any appreciable change in average pore diameter when cleaned, as shown in **Figure 3.6a**. Consequently, in all except L. Bakken samples, bitumen and dead hydrocarbons are distributed in the pore networks almost evenly across the entire range of pore diameters sensed by AD measurements. On the other hand, **Figure 3.6b** shows a distinct increase in pore diameter upon ashing for most samples. This is in line with observations that kerogen is associated with smaller pores and removal of kerogen yields increase in the average pore diameter.

Unlike the effects of sample ashing, the cleaning of samples generally reduces the average pore diameter.

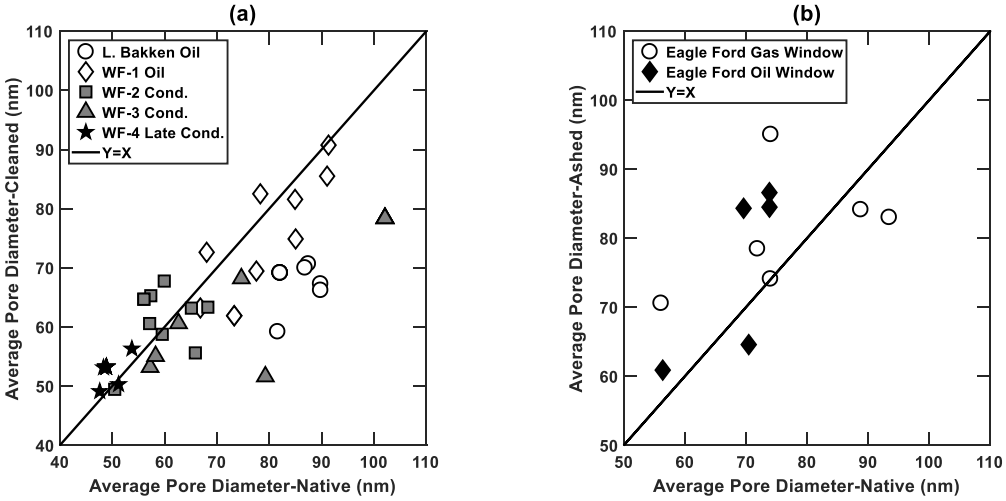


Figure 3.6: Crossplots of (a) average pore diameter of cleaned samples and (b) average pore diameter of ashed samples versus the average pore diameter of native samples.

Figure 3.7 compares the pore size distributions of samples from various thermal maturity windows. **Figures 3.7a & 3.7b** compare the PSDs of native and cleaned samples. PSD is expressed as *dV/d(log D)* plots, where *V* is pore volume in cc/g and *D* is pore diameter in nm. The PSDs are divided into three windows: $d < 20$ nm, $20 < d < 80$ nm, and $d > 80$ nm. In **Figure 3.7a**, the pore volume of pores in all windows increase with the increase in thermal maturity of the samples. The increase is most pronounced for $d < 20$ nm, which agrees with the observations by Valenza et al. (2013) that the process of diagenesis leads to the creation of nanopores. A visual comparison between **Figures 3.7a & 3.7b** highlights that the sample cleaning using 4:1 mixture of toluene and methanol primarily leads to an increase in pore volume associated with $d < 20$ nm. It can be concluded that the kerogen maturation lead to the generation of nanopores and

bitumen creation in the smaller pore sizes. Similar to our observations, Xiong et al. (2015) reported high values of change in pore surface area in pores smaller than 10 nm due to the removal of bitumen.

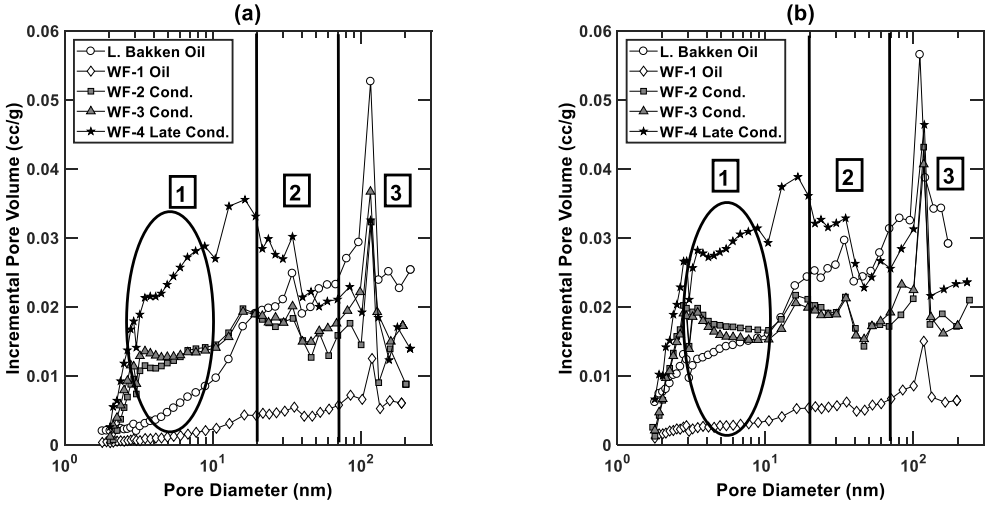


Figure 3.7: Incremental pore size distributions of (a) native samples and (b) cleaned samples.

PSDs of oil- and gas-window samples in all the pore-size windows increase due to ashing as shown in **Figure 3.8**. For oil and gas window samples, the largest increase in PSDs is for the pore-size window $d > 80$ nm. This implies that removal of kerogen tends to increase the macropore and mesopore volumes as compared to the nanopore volume.

The comparisons of PSDs across the three pore-size windows due to cleaning and ashing is depicted as histograms in **Figure 3.9**. Upon ashing, volume fraction of only pore sizes with $d > 80$ nm increases, as presented in **Figure 3.9b**. Upon cleaning, volume fraction for only pore sizes with $d < 20$ nm increases, as presented in **Figure 3.9a**. Increase in volume fraction of small pores due to cleaning is much larger compared to that of large pores upon cleaning.

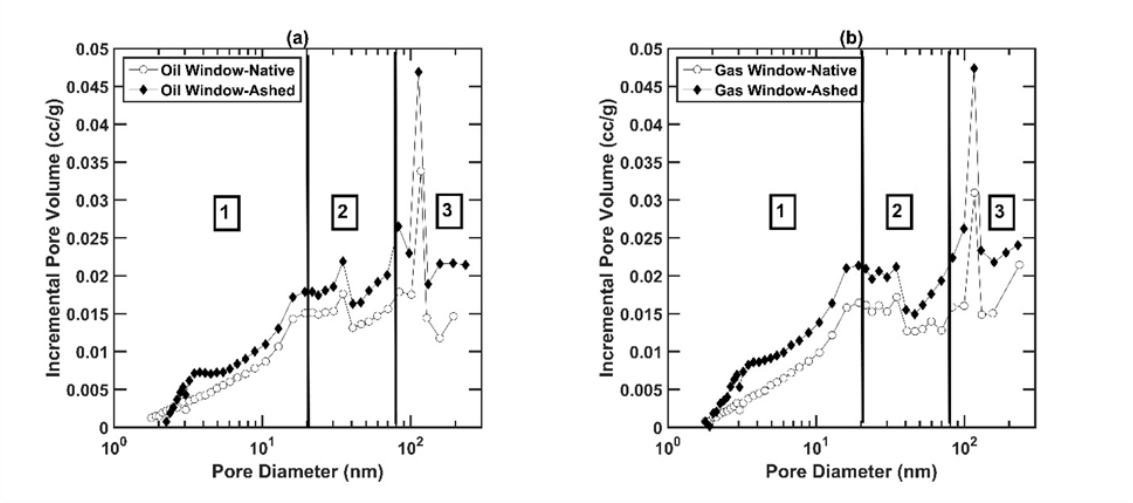


Figure 3.8: Incremental pore size distributions (a) Eagle Ford oil window samples and (b) Eagle Ford gas window samples in their native state and after ashing.

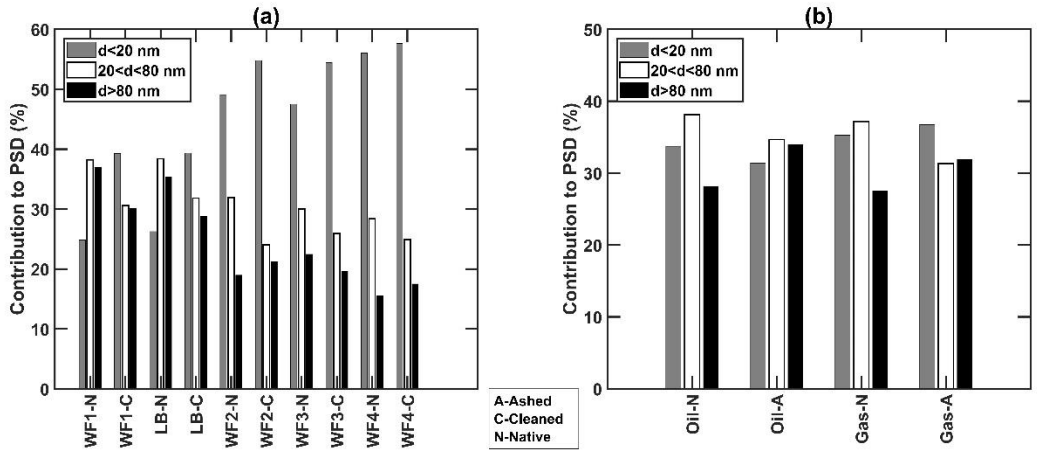


Figure 3.9: Pore-size window-based comparison of changes in pore size distribution.

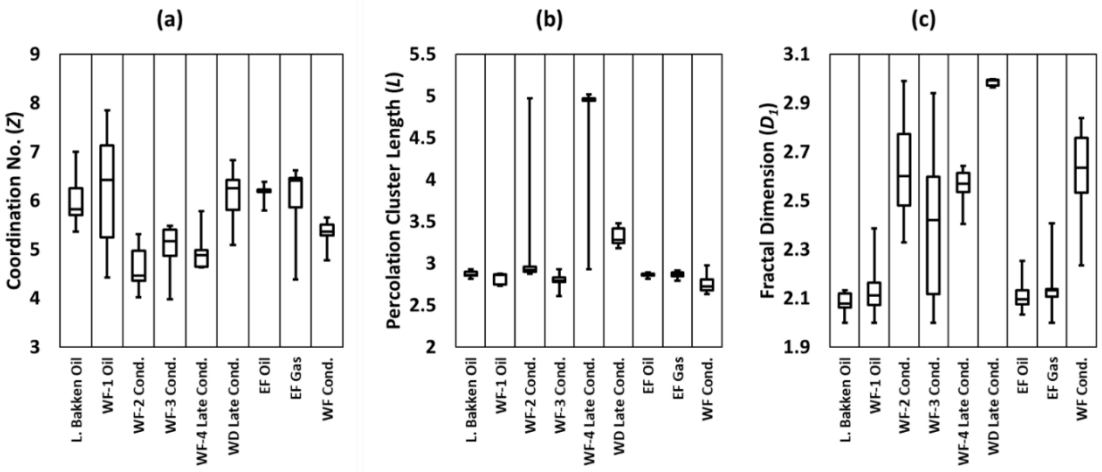


Figure 3.10: Boxplots showing range and variation of (a) coordination number (*Z*), (b) percolation cluster length (*L*), and (c) fractal dimension of first fractal regime (D_1) estimates for samples from various maturity windows.

3.3.2. Impact on percolation and fractal parameters (Z, L, D)

Coordination number (*Z*) is the number of immediate neighbors of each pore in the pore structure. An increase in coordination number will decrease the percolation threshold. Percolation cluster length (*L*) is the size of pore network in terms of number of pores contained in the network. Fractal dimension (*D*) quantifies the complexity of pore network in terms of the change in detail to the change in scale. We implement bimodal fractal regime; consequently, we obtain two values of *D* for each sample corresponding to the two regimes. **Figure 3.10** shows the range of estimates obtained for *Z*, *L* and D_1 for samples from various maturity windows. *Z* estimates do not exhibit a definite trend with kerogen maturity. Few samples have poor pore connectivity having *Z* estimates lower than 4.5. The oil- and condensate-window samples exhibit *L* estimates lower than 3, whereas the late-condensate-window samples exhibit *L* estimates in the range of 3 to 5. D_1 estimates for Wolfcamp, Bakken and Woodford formations increase with increase in thermal maturity.

Coordination number (Z) is the average number of immediate neighboring pores for each pore in the pore structure. *Z* was determined by performing an optimization on the universal scaling function shown in **Equations 2.5 & 2.6**. Cleaning removes the dead hydrocarbons and bitumen and creates more empty spaces in the pore structure which would lead to higher coordination number of pores (**Figure 3.11a**). Samples from the oil window (L. Bakken and WF-1) do not follow the aforementioned trend of coordination number upon cleaning. This indicates that the distribution of bitumen and dead hydrocarbons in the low maturity samples is not even. The impact of ashing on Z estimates is presented in **Figure 3.11b**. Upon ashing, the Z estimates increase for oil window samples, whereas those for gas window samples decrease.

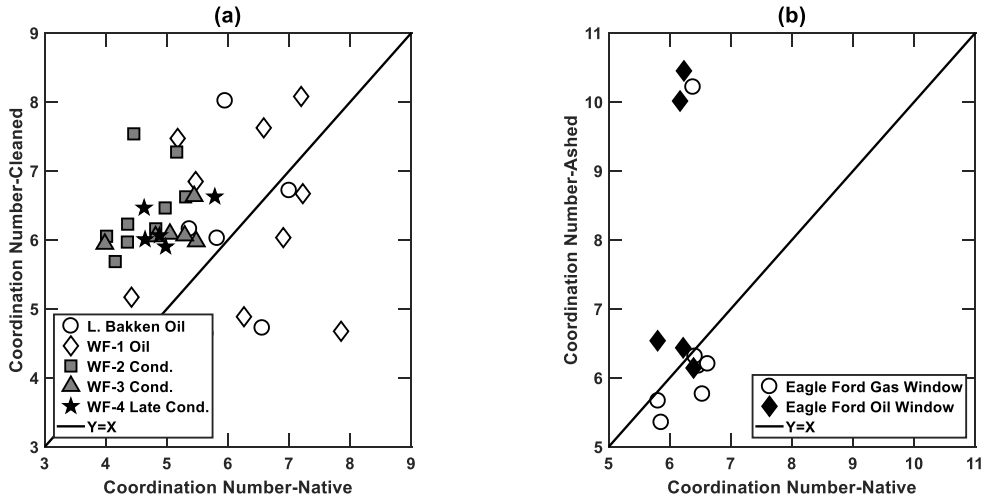


Figure 3.11. Estimates of coordination number of native samples versus (a) cleaned samples and those versus (b) ashed samples.

Percolation cluster length (*L*) for native samples is shown in **Figure 3.12**. *L* is defined as the is the size of pore network in terms of number of pores contained in the network. It is obtained along with *Z* from the optimization procedure as per universal scaling function. Liu and Seaton (1994) reported *L* values between 18 and 31 for alumina

catalyst while Daigle et al. reported values in the range of 1.8 to 2.25 for shale, kerogen and coal samples. For our optimization procedure, we assume *L* to be between 2 and 12. As observed, the results do not change on extending the limits. Therefore, the values of *L* are not constrained by limits in any of the samples. The values obtained for *L* are lower than those reported earlier. However, since *L* is not used in calculation of relative permeability results, we do not expect any error in our results due to this.

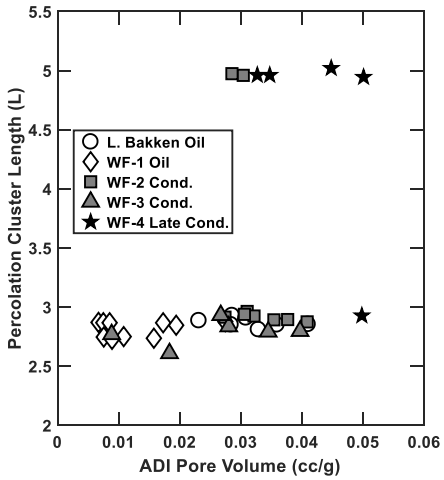


Figure 3.12: Crossplot of percolation cluster length (*L*) versus APV for native samples from various maturity windows.

For the samples, *L* estimates exhibit a distinct increase with the increase in maturity. Only, the mature samples have *L* values higher than 3. It is shown in the previous section that low maturity samples have smaller average pore diameter despite the larger volume content of nanopores and micropores. In agreement with these earlier findings, low maturity samples have low percolation cluster lengths that indicates higher content of dead-end pores. With increase in sample maturity, the pores are well connected leading to larger percolation lengths with lower volume fraction of dead-end pores. For

our dataset, we did not observe any appreciable change in L with ashing or cleaning of samples.

The theoretical limit for fractal dimensions (D) of porous reservoir rocks lie between 2 and 3, with complex fractal structures having D values close to 3. A complex pore structure has a large range of pore diameter and increased small-scale heterogeneity. An increase in the range of pore sizes requires more self-repeating structures for fractal modeling of pore structures, which leads to higher fractal dimensions. Yao et al. (2009) observed inverse relation between permeability and fractal dimension for coal samples from coalbed methane production areas in North China. Yao et al. (2008) partitioned adsorption data of coal samples into two parts and conducted independent fractal analysis to obtain two values of fractal dimensions using the Frenkel-Halsey-Hill (FHH) method. They concluded that D_1 estimated from first regime indicates fractals related to pore surface area generated by surface topography, whereas D_2 estimated from second regime correlates with fractals from pore structure and is sensitive to changes in mineral composition and pore diameter.

Figure 3.13 relates fractal dimensions of both regimes with APV for native samples. The first fractal regime typically extends from 2-30 nm and the second fractal regime extends from 30-200 nm. The limit is a result of the optimization process to get the solution and is a direct consequence of the location of peaks in incremental pore volume distribution of these samples. The fractal dimension for both fractal regimes show an increase with increase in thermal maturity, which agrees with the increase in micropore abundance, reduction in average pore diameter, and longer percolation lengths with the increase in thermal maturity of the samples. Fractal dimensions for the first

regime exhibit larger variation between 2 to 3 as compared to those for the second regime. First fractal regime extends over smaller pore sizes that exhibits simple to complex pore structure, unlike the second fractal regime that tends to mostly exhibit complex pore structures. Several samples exhibit fractal dimensions for the second fractal regime close to $D_2 = 3$, which is the highest theoretical value of fractal dimension for porous rocks.

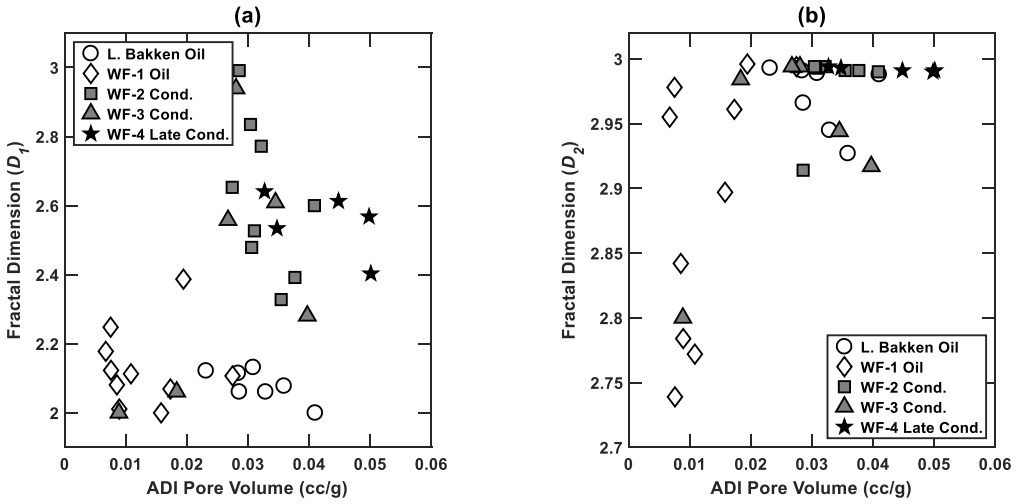


Figure 3.13: Crossplots of (a) fractal dimension of first fractal regime (D_1) versus APV and (b) fractal dimension of second fractal regime (D_2) versus APV for native samples from various maturity windows.

For the first fractal regime corresponding to smaller pore sizes, samples from all maturity windows show an increase in fractal dimension with cleaning and ashing (**Figure 3.14a**). The removal of bitumen and dead hydrocarbons invariably leads to increase in pore complexity by exposing the pore network to previously blocked micropores. Ashing leads to the replacement of pores occupied by kerogen with the host inorganic pore space; thereby leaving more complex inorganic pore networks. Addition of smaller pores to the network adds to the complexity of the network and leads to increase of fractal dimension (**Figure 3.14b**). This sounds counter-intuitive and may indicate partial removal of organic matter as a complete removal of organic matter should

lead to a decrease in fractal dimension. For the second fractal regime corresponding to larger pore sizes, fractal dimension estimates do not exhibit any significant correlation because the D_2 estimates for native samples are close to theoretical limit of 3 (**Figure 3.15**). Overall there is a decrease in the D_2 estimates upon cleaning indicating a simpler pore network for larger-sized pores in the cleaned samples.

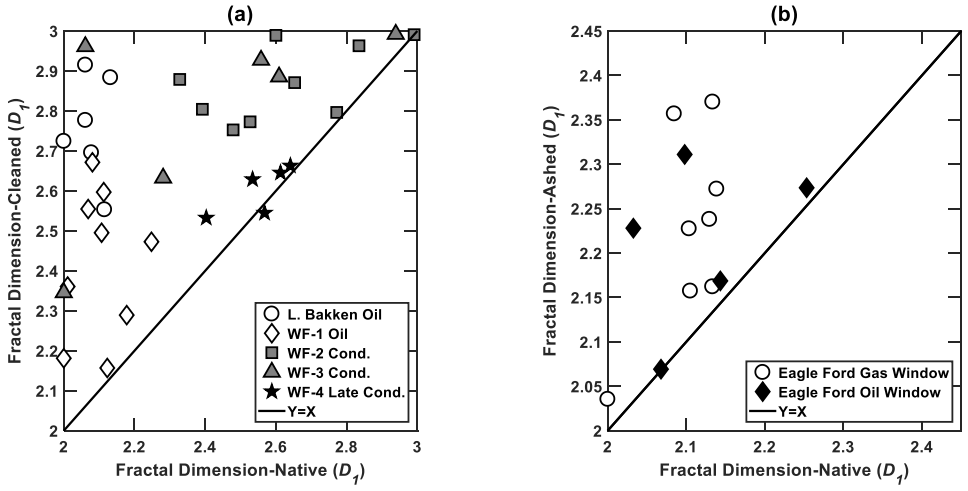


Figure 3.14: Estimates of fractal dimension of first fractal regime (D_1) of native versus (a) cleaned samples and those versus (b) ashed samples.

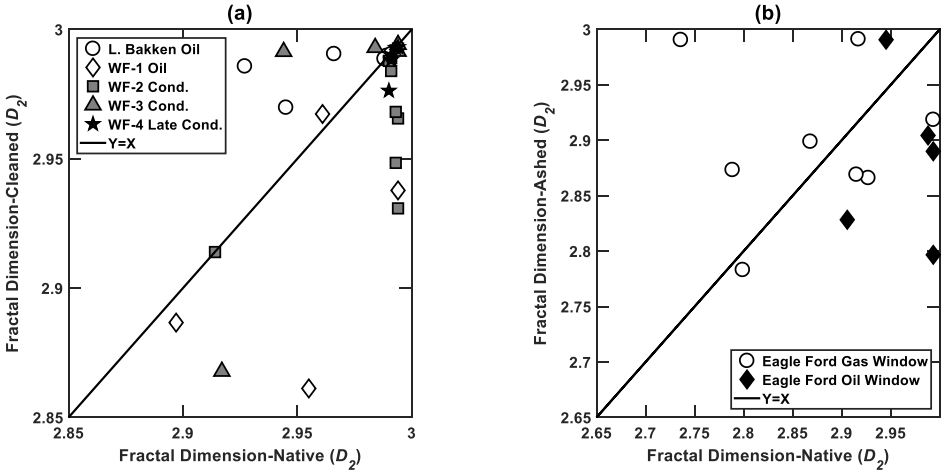


Figure 3.15: Estimates of fractal dimension of second fractal regime (D_2) of native versus (a) cleaned samples and those versus (b) ashed samples.

CHAPTER 4: ESTIMATION OF RELATIVE PERMEABILITY AND RESIDUAL/IRREDUCIBLE SATURATIONS

4.1 Estimation of relative permeability and residual/irreducible saturations

The two-phase relative permeability estimation assumes water phase as the wetting phase and the hydrocarbon phase as the non-wetting phase for shale samples. Irreducible/residual saturation of a phase is defined as the phase saturation at which the relative permeability of the corresponding phase is 0.01. Residual hydrocarbon saturation (S_{hcr}) and irreducible water saturation (S_{wir}) estimates can be obtained by interpolating values from the results in estimated relative permeability curves.

The nature of curves for relative permeability of wetting and non-wetting phases is different. For the wetting phase, effective medium theory (EMT) and percolation theory (PT) are combined to predict the relative permeability curves. PT is used for prediction near the percolation threshold and EMT is employed further away, the limit being calculated as shown in **Equation 2.7**. Use of EMT provides the non-wetting phase relative permeability curve with linear shape away from residual saturations. For saturations closer to residual saturations, the curve is non-linear due to use of PT. Similarly, PT and critical path analysis (CPA) are used for obtaining the relative permeability curve for wetting phase that results in non-linear form of the curve. The linear form of non-wetting phase relative permeability proves useful in explaining fast decline in hydrocarbon production rates. Similarly, the non-linear wetting phase relative permeability curves prove useful in explaining rapid increase in water production after sustained lower water production.

Previous attempts to model relative permeability in tight sandstone reservoirs have used Brooks-Corey model. Cluff and Byrnes (2010) used modified Brooks-Corey model to predict relative permeability for wetting and non-wetting phases in tight sands. Similar approach was used by Dacy (2010) to generate relative permeability curves. The modified Brooks-Corey model takes critical saturations for gas/water as inputs and defines the nature of relative permeability curves based on respective Corey exponents. This approach suffers from following limitations (Behrunbruch and Goda, 2006):

- Does not account for the effect of pore structure.
- Highly sensitive to endpoints of residual hydrocarbon saturation and irreducible water saturation.
- Limited sensitivity to parameters that govern the relative permeabilities at intermediate saturations between critical and maximum saturation of respective phase.
- Limited predictive capacity because it can be used to match the measured data but cannot predict relative permeability in absence of sufficient number of measurements.
- Fails if the endpoints are not available.
- The model cannot be used to predict a relative permeability relationship but is aimed to smoothen an existing relationship. For an existing dataset, the method can match measurements which can be subsequently applied on new data-points within same dataset.

These limitations can be addressed using percolation theory. The relative permeability estimation method proposed in this paper can predict both the endpoints and

the scale-dependent nature of the relative permeability curve. The pore network characteristics, pore size distribution, and percolation behaviors of wetting and non-wetting phases are honored in the proposed estimation method. Separate parameters define the endpoints and the nature of curves which allows independent validation of these parameters. However, the proposed estimation method is only applicable to the relative permeability of the micro- and mesoscale pores in the range of 2 nm to 200 nm.

Figure 4.1 shows representative relative permeability curves for native samples from various maturity windows. Samples from similar maturity windows exhibit similar relative permeability curves. Lower maturity samples have higher relative permeabilities for both the phases indicating better flow performance for both the phases compared to mature samples. WF-4 samples (late condensate window) have the lowest relative permeability, whereas the least mature WF-1 samples have the largest relative permeability. In terms of production performance, samples with lower maturity should exhibit slower decline in gas production rates and faster and more uniform increase in water production. This would be accompanied by higher cumulative production for hydrocarbons and water for WF-1 or L. Bakken samples. Among the formations studied in this paper, WF-1 is likely to sustain hydrocarbon production over a longer production period along with uniform increase in water production rates. WF-1 samples would show higher cumulative water and hydrocarbon production. High maturity samples, like those from WF-4, should show rapid decline in the hydrocarbon production rates with sustained low water production rates until very high-water saturations are achieved in the reservoir when the water production will show a drastic increase. WF-4 samples are also likely to have minimum cumulative production for water and hydrocarbons.

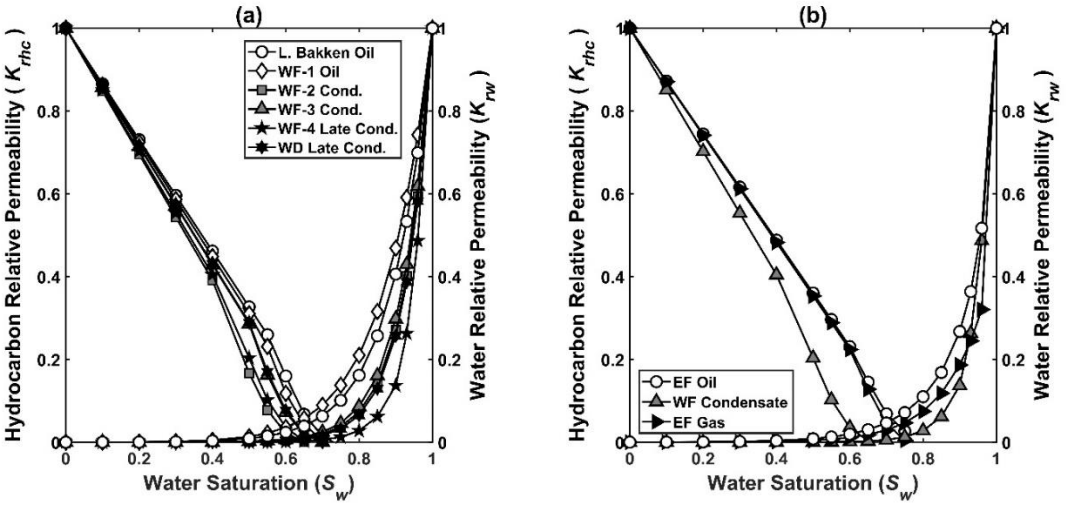


Figure 4.1: Relative permeability curves for wetting and non-wetting phases for (a) Bakken, Woodford and Wolfcamp samples from dataset-1 mentioned in Table 2.1 and (b) Eagle Ford and Wolfcamp samples from dataset-2 mentioned in Table 2.1.

In **Figure 4.1b**, the relative permeability curves for Eagle Ford, Wolfcamp, and Woodford samples from dataset-2. Unlike the trend observed for samples in dataset-1 (**Figure 4.1a**), relative permeability curves of the samples in dataset 2 (**Figure 4.1b**) do not correlate with thermal maturity. However, the curves for samples in dataset-2 correlate with the total volume of pores of size between 2 to 200 nm, also referred to as the adsorption-desorption-isotherm pore volume (APV). Wolfcamp samples with highest APV have the lowest relative permeability for both wetting and non-wetting phases (**Figure 4.1b**). Eagle Ford samples from oil and gas window have similar APVs and show similar relative permeabilities. A slight increase in APV of Eagle Ford gas window sample correlates with slightly lower water relative permeability of gas window sample.

Figure 4.2 shows the correlation between relative permeability of a phase at a fixed saturation and corresponding residual/irreducible phase saturation. For all saturations, relative permeability of both the phases exhibit an inverse relation with the

residual phase saturations. The inverse relation between relative permeability and residual/irreducible saturations is the characteristic of the formulation used and may not be present in field cases.

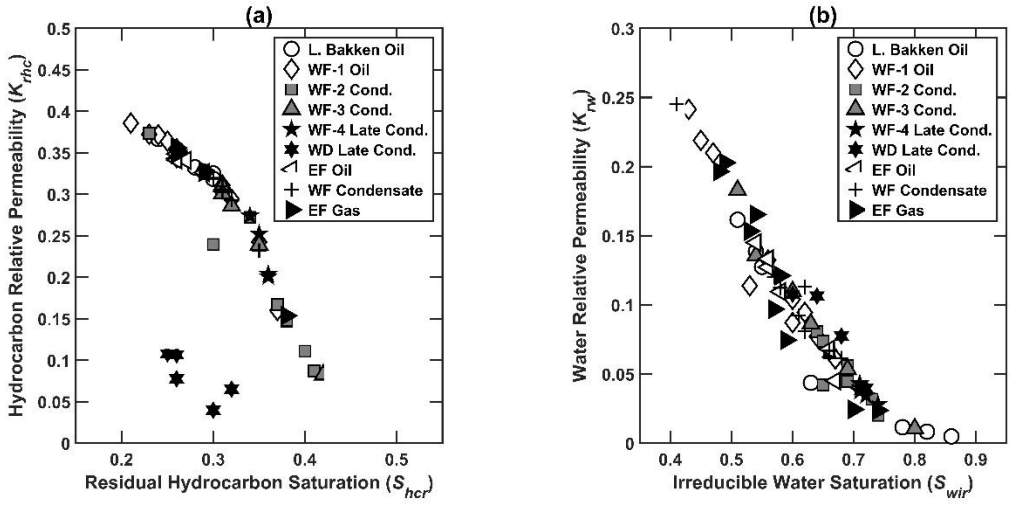


Figure 4.2: Correlation between relative permeability and residual/irreducible saturations for (a) non-wetting hydrocarbon phase at S_w=0.5 and (b) wetting aqueous phase at S_w = 0.8.

4.2 Sensitivity of relative permeability curves to network properties

A sensitivity study on different variables being used in calculation of relative permeability curves is performed to illustrate the role of each parameter. A single formation with default parameter values is considered for the sensitivity study. Thereafter, we vary the value of a single parameter while keeping other parameters at constant values to generate the model sensitivities. **Table 4.1** mentions the default values of the parameters. The relative permeability curves obtained for the various cases are shown and analyzed to infer the importance of these parameters on saturation-dependent fluid transport properties.

Table 4.1: Default values of model parameters used for the sensitivity study on the relative permeability model.

Pore Volume (ϕ in cc/g)	0.0231
Coordination Number (Z)	5.7745
Percolation Cluster Length (L)	2.8871
β_1	0.0090
D_1	2.1221
β_2	1.0000
D_2	2.9928
d_x (nm)	31.47
Min. Pore Diameter- d_{min}(nm)	1.74
Max. Pore Diameter- d_{max}(nm)	274.35
θ_x	0.0100
ϕ_1	0.0080
ϕ_2	0.0151

Changes in coordination number (Z) directly impacts θ_x & θ_t, as discussed in the interpretation methodology section. Consequently, change in Z affects the relative permeability for both phases. Increase in Z gives rise to a decrease in percolation threshold that implies reduction in residual saturations of both the phases (**Figure 4.3a**). There is an increase in the perceived-wettability of the system to the aqueous phase with the increase in Z, as supported by the movement of the point of intersection of wetting and non-wetting phases towards right. For the non-wetting phase, relative permeability curve only depends on Z and θ_x. Hence, as Z increases the curve moves rightward and the non-linear behavior of the curve decreases. For the wetting phase, however, the curve also depends on fractal parameters discussed further and there is an interplay between θ_t and porosities of the two fractal regimes. As can be seen from **Equations 2.9 & 2.10**, nature of the curve for wetting phase relative permeability changes due to alteration in θ_t, which is affected by the change in Z. However, the strong correlation visible earlier in the wetting phase curves tends to weaken for the non-wetting phase. Unlike Z that

indicates the short-range connectivity, percolation cluster length (L) does not affect the relative permeability curves. The estimation method is not able to model the influence of long-range pore connectivity on the transport properties because L is not used quantitatively in any of the mentioned equations. Nonetheless, in mathematical terms, Z and L are related through the optimization used to determine them by processing the ADI measurements using the universal scaling function based on Seaton's method (Seaton, 1991).

Figure 4.3b shows the impact of variation in θ_x on the curves for constant Z and θ_t. Under these restrictions, the wetting phase remains unchanged and independent of θ_x. For the non-wetting phase, θ_x determines the point of switch between percolation theory scaling to effective medium theory formulation. In other words, the parameter determines the point where the curve becomes non-linear around a fixed residual saturation. Higher value of θ_x means percolation theory is being used for larger window of water saturation around the residual saturation.

Pore size distribution of the samples are modeled using a bimodal fractal model that requires us to define the pore diameter d_x demarcating the change in the fractal regime (**Equations 2.9 & 2.10**). The contributions of fractal regimes change by changing the pore diameter at which this switch occurs; thereby changing the nature of the curve for wetting-phase relative permeability (**Figure 4.3c**). No impact is seen on non-wetting phase relative permeability. Generally, a decrease in d_x leads to uniform increase in water relative permeability with the increase in water saturation indicating the presence of predominantly one type of pore fractal regime. Higher values of d_x leads to increase in

residual saturation due to the effect of pore complexity of smaller-sized pores and also leads to a rapid increase in water-phase relative permeability.

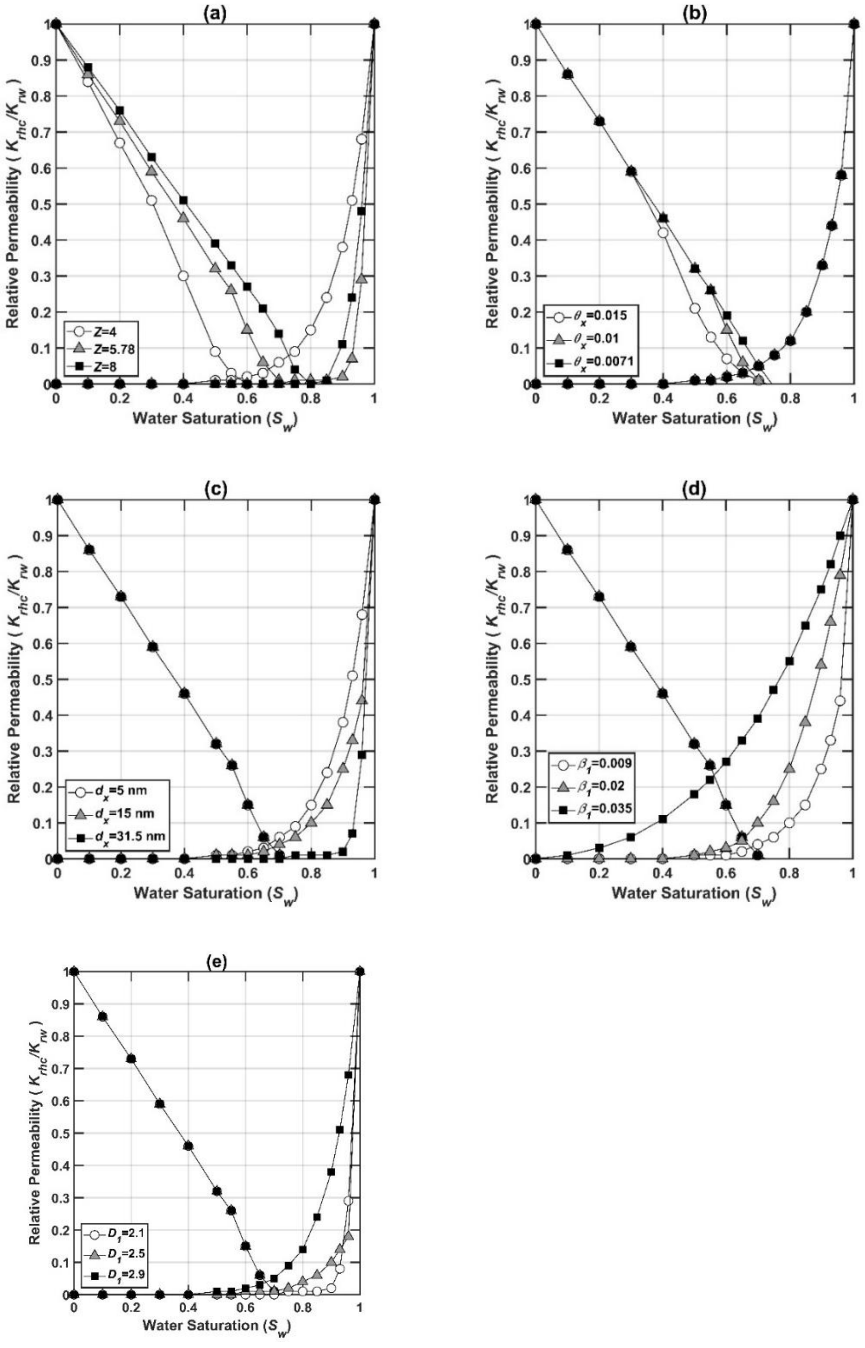


Figure 4.3: Relative permeability curves for wetting and non-wetting phases for sensitivity of (a) coordination number (Z), (b) fluid content level for switch between percolation and effective medium formulations (θ_x), (c) pore diameter for change of fractal regimes (d_x), (d) probability of drainage for first fractal regime (β_1), and (e) fractal dimension of first fractal regime (D_1).

Probability of drainage (β) values are constant multipliers in the fractal model. It must be noted that d_x values must be constant for analyzing sensitivity in β. A higher β implies higher pore volume of the corresponding fractal regime and overall a higher porosity. An increase in wetting-phase relative permeability and resultant decrease in irreducible water saturation is observed with the increase in β (**Figure 4.3d**). Again, no impact is seen on non-wetting phase relative permeability as it is independent of fractal model. Higher β lowers the probability of observing "permeability-jail" and reduces the perceived-wettability to aqueous phase. Here, for the sake of simplicity we illustrate the impact of β from first fractal regime but the effects of β in both fractal regimes are identical.

As seen in **Equations 2.9 & 2.10**, fractal dimension (D) acts as exponent for wetting-phase relative permeability formulation. Therefore, increase in fractal dimension changes the nature of curve for wetting-phase relative permeability if we assume constant irreducible water saturation (**Figure 4.3e**). In other words, increase in pore volume is implied with increase in fractal dimension. A higher fractal dimension leads to regular increase in water relative permeability. If pore volume is assumed constant, both β and D values need β to be changed simultaneously. In this case, changes in D have results similar to that seen in **Figure 4.3c** with increase in d_x value for wetting phase. This trend is illustrated using the fractal dimension of first fractal regime D_1, which is similar to the influence of D_2.

To summarize, the non-wetting phase relative permeability depends on Z and θ_x. On the other hand, wetting phase relative permeability depends on both percolation and fractal parameters including Z, d_x, β, and D. This is the direct result of use of critical path

analysis which invokes fractal parameters only for wetting phase relative permeability formulation.

4.3 Correlations of estimates with ADI pore volume, TOC and LPP porosity.

Figure 4.4a shows the correlation of residual hydrocarbon saturation (S_{hcr}) with thermal maturity of organic matter, such that mature samples from condensate window tend to have higher residual gas saturation and APV than those for oil window samples. Irreducible water saturation (S_{wir}) exhibits the positive correlation with thermal maturity, as shown in **Figure 4.4b**. These trends can be explained by microstructural changes in pore structure with increase in thermal maturity. Due to the conversion of kerogen to bitumen and hydrocarbons, there is an increase in mesopores and micropores. The non-wetting phase tends to reside in larger pores, whereas the wetting phase will occupy the smaller pores. Increase in both micropores and mesopores leads to an increase in residual hydrocarbon saturation and irreducible water saturation. A similar trend is observed for the residual/irreducible saturations as a function of total porosity measured using low-pressure helium pycnometry.

In **Figure 4.5**, no definite correlations are observed between residual/irreducible saturations and TOC. Except for L. Bakken samples, all other samples have TOC in the range of 1-4%. The extended TOC range for L. Bakken samples may have distorted possible correlations existing between these parameters. Absence of a definite correlation may be a consequence of the assumption that all pores in the shale sample are water wet.

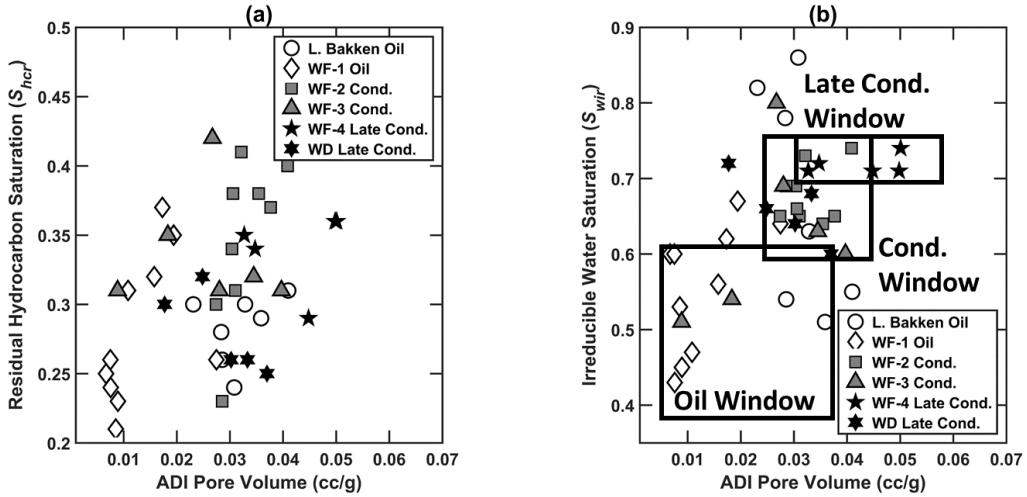


Figure 4.4: Crossplots of (a) residual hydrocarbon saturation (S_{hcr}) and that of (b) irreducible water saturation (S_{wir}) with ADI pore volume (APV).

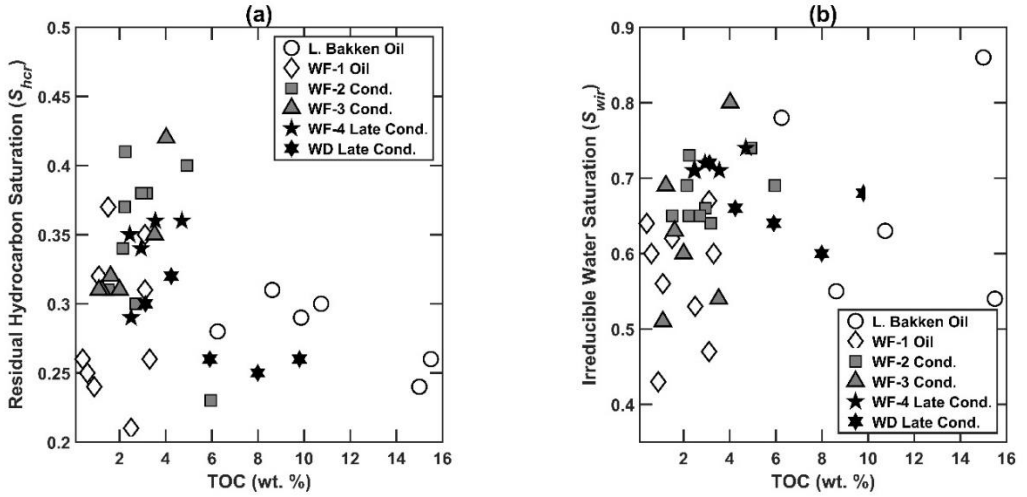


Figure 4.5: Crossplots between (a) residual hydrocarbon saturation (S_{hcr}) and TOC, and that between (b) irreducible water saturation (S_{wir}) and TOC.

4.4 Impact of Ashing and Cleaning on relative permeability estimates

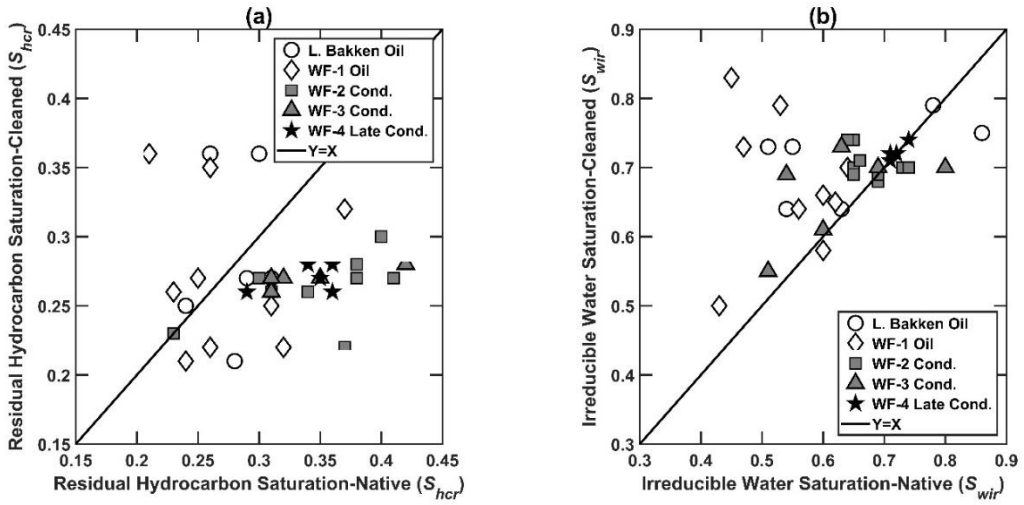


Figure 4.6: Changes in (a) residual hydrocarbon saturation (S_{hcr}) and (b) irreducible water saturation (S_{wir}) of samples due to cleaning with methanol-toluene mixture.

Cleaning the samples with a 4:1 toluene-methanol mixture leads to a decrease in residual hydrocarbon saturation (**Figure 4.6a)** and increase in hydrocarbon relative permeability (**Figure 4.7a**). Further, the cleaning results in a slight increase in irreducible water saturation **(Figure 4.6b)** and a slight decrease in the wetting phase relative permeability (**Figure 4.7a**). Oil-window samples show the largest variation in these results (**Figure 4.6**). The aforementioned impacts of cleaning are a consequence of the microstructural removal of bitumen and soluble dead hydrocarbons especially from larger pores, thereby exposing greater pore surface area that resists the wetting-phase fluid flow. Non-wetting phase tends to occupy the larger pores and the creation of pore space due to cleaning facilitates the movement of non-wetting phase, which is reflected as a significant increase in the non-wetting phase relative permeability. The wetting phase can spread on the newly-created surface and thus has an increased value for residual wetting-phase saturation.

In **Figure 4.7b**, the relative permeabilities for wetting and non-wetting phase for gas window samples tend to change only slightly upon the removal of kerogen through ashing. This indicates that the maturation process has already converted most organic matter to hydrocarbons in gas window. Thus, the pore network characteristics do not change substantially upon removal of kerogen from mature gas-window samples. However, for oil window samples, the residual hydrocarbon saturations do not vary, which results in nearly unaltered hydrocarbon relative permeability, as shown in **Figure 4.7c**. Notably, for the wetting phase, removal of kerogen through ashing results in a decrease in irreducible water saturation and an appreciable increase in the relative permeability of the wetting phase (**Figure 4.7c**). This is a consequence of the removal of micropores and mesopores in kerogen upon ashing which indicates reduced surface area over which the wetting phase can spread.

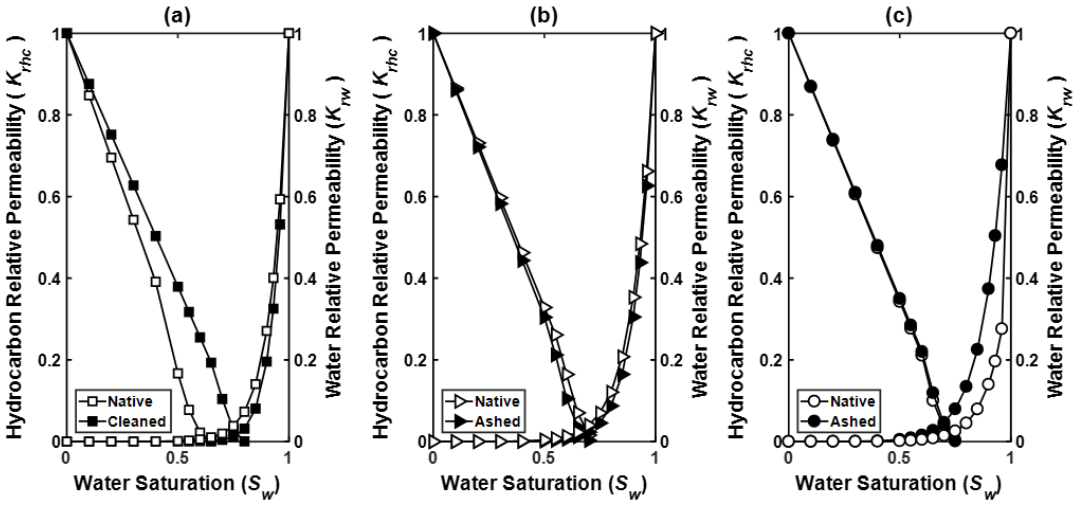


Figure 4.7: Changes in relative permeability due to (a) cleaning with methanol-toluene mixture, (b) ashing for Eagle Ford gas window samples, and (c) ashing for Eagle Ford oil window sample.

4.5 Applications to performance prediction.

To illustrate the impact of the estimated relative permeability curves on the production performance of the formations, we created reservoir models using the Computer Modeling Group (CMG) software. The assumed default values for key parameters of the numerical reservoir flow model is shown in **Table 4.2**. We assume the reservoir to contain gas and water to predict the production performance. The reservoir is drained either through a single vertical well (Case-1) or a horizontal well (Cases-2 & 3) perforated throughout the pay zone and located in the center of the reservoir. In both the cases, the well produces for a period of 10 years. Relative permeability curves for each formation, which is the key input to the reservoir model, is assumed to be the average of the relative permeability estimated for the native organic-rich shale samples extracted from the corresponding formation, as presented in **Figure 4.1a**. We perform the numerical simulations under the following three well scenarios:

- Case-1: Formations have the same porosity (4%) and viscosity with gravity effect and are drained by a vertical well.
- Case-2: Formation properties remain same as in Case-1 but the production well is a horizontal well with perpendicular horizontal fractures. The fracture properties are listed in **Table 4.3**.
- Case-3: All inputs for reservoir and fracture properties are similar to those in Case-2. Oil production is predicted for oil window samples for various fluid viscosities. Similarly, for condensate and late condensate window, cumulative gas productions are predicted for corresponding viscosities.

Table 4.2: Default values of the key inputs used in simulation fluid flow models to demonstrate the impact of relative permeability curves on the production performance for Case-1.

Type of Reservoir	Gas-Water System
No. of Cells in Grid	100*100*10
Grid Size (ft)	10*10*1
Grid Top (ft)	6000
Horizontal Permeability (md)	0.1
Vertical Permeability (md)	0.01
Reservoir Pressure (psi)	6000
Reservoir Temperature (°F)	140
Gas specific gravity	0.6
Porosity (%)	4
Rock Compressibility (psi^{-1})	$6x10^{-6}$
Initial Water Saturation (%)	60
Minimum well bottomhole pressure (psi)	500
Maximum gas production from well (MSCF/D)	1000
Net-to-Gross	1
Formation Thickness (ft)	10

Cumulative productions of hydrocarbon and water phases are shown for each of the five formations. Cumulative production forecasts for both fluid phases are strongly governed by the relative permeability estimated for a given formation. For the case of fully perforated vertical well in these formations (**Figure 4.8**), Lower Bakken oil formation has the highest hydrocarbon-phase relative permeability, whereas Wolfcamp condensate (WF-2) and late condensate (WF-4) formations have the lowest hydrocarbon-phase relative permeability. This is the result of lower coordination numbers and higher fractal dimensions for the mature WF-2 and WF-4 formations. Cumulative water production is highest for Wolfcamp oil formation (WF-1) and lowest for the Wolfcamp late-condensate formation (WF-4). We observe that the hydrocarbon-phase production of Lower Bakken oil formation is better than that of Wolfcamp oil formation (WF-1) but water production trend is significantly reversed. These observations are the result of minor variations in the fractal properties, like fractal dimension, which are influenced by

pore size distribution of these formations. The fractal properties only influence the wetting phase relative permeability. Due to variations in each property, we recommend avoiding quantitative comparison of nearly equal parameters and focus on the general trend of increasing relative permeability of samples of lower thermal maturity. This implies that reservoirs of lower thermal maturity, like Lower Bakken and Wolfcamp oil window formations, would possess the best transport properties leading to higher cumulative production for both hydrocarbon and water phases. On the other hand, Wolfcamp and Woodford late condensate window samples would have poor transport characteristics and lower cumulative production for both hydrocarbon and water.

Table 4.3: Fracture and horizontal well inputs used in simulation fluid flow models to demonstrate the impact of relative permeability curve on the production performance for Case-2.

Fracture Geometry	Planar
Fracture Width (ft)	0.08
Fracture Permeability (md)	200
Effective Permeability (md)	8
Fracture Orientation	Horizontal
Fracture Half-length (ft)	50
Fracture Height (ft)	5
Length of horizontal section (ft)	200
Fracture Spacing (ft)	100
No. of fracture stages	3
Non-Darcy Flow Correlation	General

Case-2 focuses on fractured horizontal well production in these formations (Figure 4.9). The higher permeability due to fractures allows for higher production rates which leads to faster increase in cumulative production for both phases for period < 1000 days. Thereafter, production rates stabilize with relatively slower increase in the cumulative productions. Higher stimulated rock volume leads to increase in ultimate recovery and higher permeability in vicinity of wellbore leads to acceleration of

production. This implies that although well design affects the cumulative production and ultimate recovery, the production trends are predominantly governed by relative permeability curves alone and remain unchanged by well design variation.

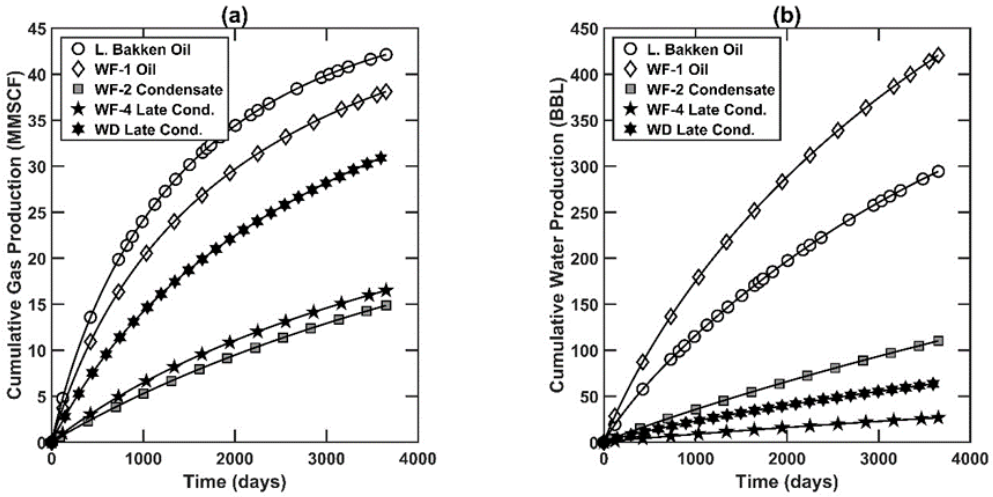


Figure 4.8: Simulation-generated (a) cumulative gas production and (b) cumulative water production of a vertical well (Case-1) in various formations.

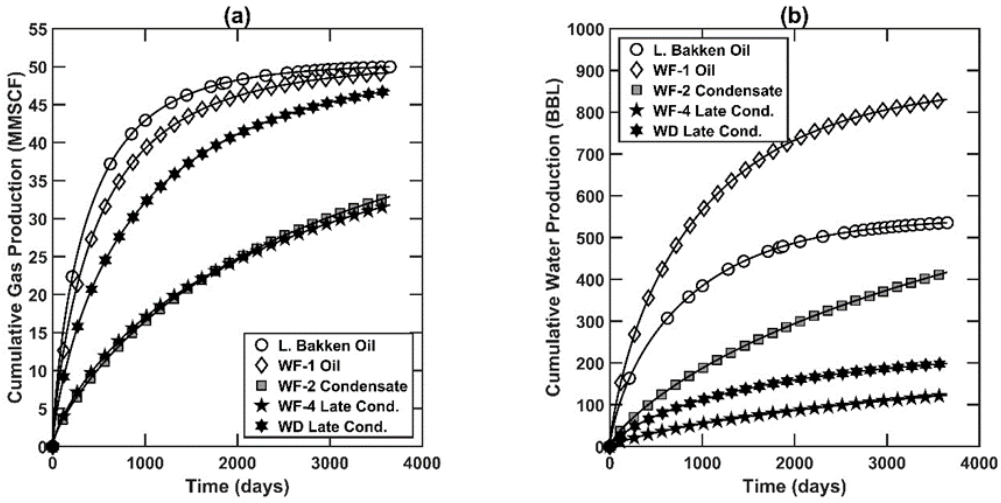


Figure 4.9: Simulation-generated (a) cumulative gas production and (b) cumulative water production of a horizontal fractured well (Case-2) in various formations.

The cumulative production differences between the three best performing formations in the horizontal production well scenario (**Figure 4.9**) are much lower than

for those in the vertical production well scenario (**Figure 4.8**). The relative performance of the worst performing formations in the horizontal well scenario are much better than for those in the vertical well scenario. These are direct consequences of enhancement of permeability due to hydraulic fractures. Fracturing leads to better transport characteristics and horizontal orientation of well leads to better vertical sweep efficiency achieved in smaller production time. This leads to improvement in ultimate recovery for all reservoirs. The ultimate recovery depends on the matrix permeability and is nearly constant for the best performing reservoirs. The relative permeability affects the production time required to drain the reservoir. Therefore, reservoirs with higher relative permeability achieve higher productions at smaller time. The cumulative water production increases disproportionately in comparison to the increase in cumulative hydrocarbon-phase production when the production well changes from vertical to horizontal orientation. This is due to improved vertical sweep caused by horizontal well design. Coupled with gravity, water is able to sweep gases further across the reservoir which leads to higher water saturation and higher cumulative water production. Production performances of the formations exhibit greater variations in the horizontal well scenario compared to those in the vertical well scenario. The improved performance is due to improved sweep in the reservoir by water phase assisted by horizontal trajectory of well and better permeability due to hydraulic fractures. The key observation here is the unchanged trend of production between both cases. The well design may affect the cumulative production figures but reservoirs of lower thermal maturity (Lower Bakken and Wolfcamp oil window) continue to perform better than formations of higher maturity (Wolfcamp and Woodford late condensate).

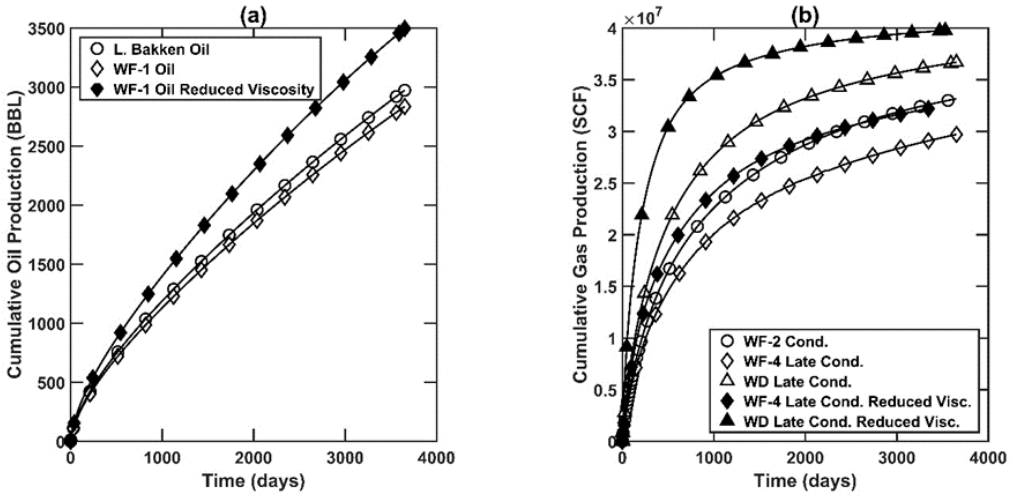


Figure 4.10: Simulation-generated (a) cumulative oil productions of oil-window formations, and (b) cumulative gas productions of condensate and late condensate window formations using horizontal wells of similar design as in Case-2.

Maturation leads to changes in fluid properties like decrease in viscosity, increase in gas-oil ratio and change in reservoir pressure. We designed Case-3 to test the impact of change in viscosity on the production performance of the reservoirs. The impact of hydrocarbon-phase viscosity on production performance of horizontal fractured wells in all formations are shown in **Figure 4.10**. We assume all oil-window reservoirs to have 40° API oil with the water-oil contact at 6010 ft. The wells are operated at minimum bottomhole pressure of 500 psi. In Case-2, we assume similar viscosities for L. Bakken and WF-1 oil. In Case-3, the viscosity of WF-1 oil is reduced to consider the impact of maturation on fluid viscosity. The inputs used for the oil-phase viscosity models are shown in **Table 4.4**. All other reservoir and well inputs remain same as defined for Case-2. Similarly, for condensate and late condensate windows of WF-4 and WD formations, the gas viscosities are assumed to be lower than WF-2 formation. For both oil and gas studies, the properties for water phase remains unchanged. Hydrocarbon production in Case-3 is simulated for the zone having similar water saturation as Case-2.

Table 4.4: Fluid inputs used in simulation fluid flow models to demonstrate the impact of relative permeability curve along with fluid viscosity on the production performance for Case-3.

	Initial viscosity at reservoir conditions (cp)	Reduced viscosity at reservoir conditions (cp)
L. Bakken Oil Window	2	2
WF-1 Oil Window	2	1.5
WF-2 Condensate Window	0.037	0.037
WF-4 Late Condensate Window	0.037	0.025
WD Late Condensate Window	0.037	0.015

With similar viscosities for L. Bakken and WF-1 formations, L. Bakken exhibits slightly higher cumulative oil production (**Figure 4.10a**) according to the hydrocarbon relative permeability curves (**Figure 4.10a**). When viscosity for WF-1 is reduced, the trend is reversed and WF-1 shows better performance than L. Bakken. The same result is observed for condensate and late condensate window samples (**Figure 4.10b**). With similar gas viscosities, WF-2 exhibits higher cumulative gas production than WF-4. When the viscosity for WF-4 is reduced according to maturity, both WF-2 and WF-4 show nearly identical cumulative gas production. These predictions show that the effect of fluid viscosity on production performance may dominate the effect of relative permeability. Therefore, for realistic comparison of field performance based on thermal maturity, fluid properties and reservoir pressure affected by increasing kerogen maturity need to be considered in conjunction with the trends in relative permeability.

CHAPTER 5: MODELING OF PRESSURE TRANSIENT RESPONSE IN NATURALLY FRACTURED RESERVOIRS

The method for modeling of pressure transient response is based on solution of the Eikonal equation. The Eikonal equation defines the propagation of the pressure wave in the reservoir with time and helps in tracking of the pressure propagation front. This equation can be solved using specialized methods called fast marching methods. These methods use finite difference approximation to solve for position of the pressure front at each time-step. The term stencil is used to denote the technique of solution of these fast marching methods. A stencil refers to orientation of nearby cells for each grid point which are used for solution of the equation at each grid point. A single stencil refers to use of cells only in X & Y directions in 2D. A multistencil approach refers to addition of diagonal cells to cells in X & Y directions for the calculation procedure. The solution traverses from one grid point to other until the solution is known for the entire grid. This gives us the location of the pressure front with time. A drainage volume is calculated at each time-step corresponding to the computed location of the front. Spatio-temporal evolution of drainage volume is analyzed to estimate the pressure drop and pressure derivative response of vertical wells in various reservoir and well scenarios.

5.1 Multistencil Fast Marching (MFM) Method

Fast marching solution of Eikonal equation form of diffusivity equation assumes that the arrival time of the pressure front at any node is only dependent on the lowest value of arrival time among the immediate neighboring nodes. This assumption is called the “causality relationship” (Hassouna and Farag, 2007). Unlike conventional fast marching methods, MFM method includes all adjacent nodes including the diagonal

nodes during the calculation of diffusive time of flight (DTOF) from the central node. MFM method was implemented in Matlab using code developed by Yoon (2017). Following steps are executed in the MFM approach (**Figure 5.1**):

1. Use a numerical simulation model in Matlab to develop the 2D reservoir diffusivity map discretized into equal-sized square grids. The center of the grids are the nodes and the lines connecting the nodes in vertical, horizontal, and diagonal directions are the stencils used for the fast marching calculations (also, referred to as diffusive time of flight).
2. Assign the heterogeneous distributions of permeability, viscosity, compressibility, and porosity across the reservoir to the corresponding grids or stencils for the calculation of the diffusivity along each stencil.
3. First node (vertical well location) is selected among the available nodes in the reservoir model and the arrival time for that node is assigned an initial value to start the fast marching calculation (**Figure 5.1a**). Selected node is identified by the filled circle. This is the initialization step. For all the studies listed in this paper, the first node is denoted as source point in corresponding reservoir maps.
4. 8 neighboring nodes around the selected central node (vertical well location) are identified along the 8 stencils, shown as unfilled circles (**Figure 5.1b**).
5. DTOFs of the propagating pressure front from the selected central node to the 8 neighboring nodes are calculated along the 8 stencils (**Figure 5.1b**).
6. Different stencils can have different diffusivity. Therefore, the neighboring node with minimum value of DTOF among the 8 neighboring nodes is selected as the node for

the next fast marching calculation (**Figure 5.1c**). The newly selected node is identified by the filled circle.

7. Arrival time of the pressure front at the newly selected node is the sum of arrival time of pressure front at the previously selected node and a time-equivalent of DTOF calculated along the stencil joining the previously and newly selected nodes.
8. The multistencil then moves to the newly selected node and DTOFs are calculated for the new 7 unselected neighboring nodes (**Figure 5.1d**).
9. The node with minimum value of DTOF among the 12 unselected neighboring nodes is selected as the node for the next fast marching calculation.
10. Steps similar to Steps 8 and 9 are repeated till arrival times for all the nodes are known.

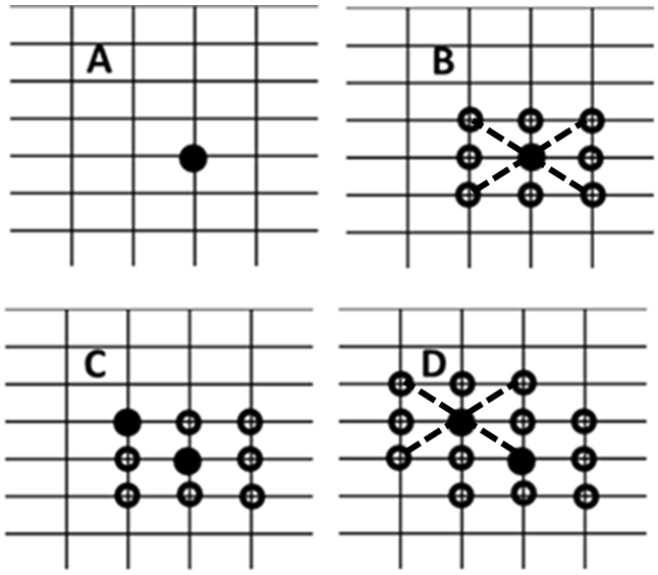


Figure 5.1: Schematic of multistencil fast marching (MFM) algorithm.

The above workflow helps us to solve the Eikonal equation form of diffusivity equation for modeling the propagation of the pressure front in a 2D reservoir (King et al.,

2016). DTOF and diffusivity in the heterogeneous media are related using the following equation:

$$|\nabla\tau(\mathbf{x})|\sqrt{\frac{k(\boldsymbol{x})}{\varphi(\boldsymbol{x})\mu c_t}} = 1 \tag{5.1}$$

where x denotes location of the neighboring node, k is permeability, φ is porosity, μ is fluid viscosity and c_t is total compressibility. Parameters k, φ, μ, and c_t are defined along the stencil joining the selected node and neighboring node of interest located at x. For this study, μ, φ and c_t are assumed to be constant in the entire reservoir including the fractures. The entire term inside the square root is referred as the diffusivity α. $\tau(x)$ is DTOF from the selected node to the neighboring node at x and has the unit of time$^{0.5}$. This technique approximates DTOFs of the pressure front propagation from each selected node to its neighboring nodes. DTOF calculated using the MFM approach is transformed to the physical time t to formulate drainage volume as a function of time using $\tau^2 = 4t$, which assumes flow in pseudo steady state with a transient reservoir boundary (King et al., 2016). This implies negligible pressure depletion beyond the pressure front during a 2D radial flow. The contours connecting nodes of equal arrival time denote the time-varying drainage volume. These drainage volumes are converted to pressure and pressure derivative response of the vertical production well centrally located in the assumed reservoir configuration. A geometric approximation of the drainage volume is used to relate the well rates with the pressure response of a well. A detailed explanation of the procedure with required equations is provided by King et al. (2016).

5.2 Workflow for generating 2D reservoir diffusivity map used to study the effects of conductive natural fractures on pressure front propagation and pressure transient response

A spatially discretized 2D reservoir model needs to be created prior to the fast marching calculations. The workflow used for creating the 2D naturally fractured reservoir model used for the study presented in this paper is as follows:

1. We generate 2D reservoir diffusivity map with varied fracture characteristics, such as fracture length, compressibility, orientation, permeability, and volume fraction of fracture. These maps are imported into the MATLAB-based MFM code for fast marching calculations, as described in the previous section.
2. For this study, a 2D reservoir of dimension of 2000 ft is discretized into 1-ft×1-ft grids. The square reservoir is bounded by no-flow boundary. A vertical production well is located at the center of the circular reservoir.
3. Primary reservoir is the isotropic and homogeneous matrix. Conductive natural fractures of varying properties are placed on the primary reservoir.
4. Conductive natural fractures are defined using the following properties: length, width, orientation, volume fraction, and conductivity. These fractures are inserted at random locations in the primary reservoir. For this study, the natural fractures are assigned viscosity, and porosity similar to the primary reservoir matrix.
5. The 2D reservoir diffusivity map thus generated shows the distribution of fractures in the reservoir.

It is important to note regarding the importance of permeability contrast during generation of fracture distributions. The fracture distributions can be created using any

geological modeling package. However, we observed that these packages may alter the permeability of cells around each introduced fracture to smoothen the permeability variation in nearby cells. This may alter the volume fraction and permeability contrast desired in some cases. To overcome this, we generated these fracture distributions using a code developed in Matlab to ensure accurate permeability contrast and volume fractions of fracture distributions in each reservoir geometry.

5.3 Assumptions made in the approach

1. The proposed method assumes the primary 2D reservoir to be isotropic and homogeneous. The fluid is assumed to be slightly compressible and consisting of single phase.
2. The grid dimension for the method is 1 ft. A constant flow rate is assumed for the vertical production well in the reservoir.
3. The method is based on fast marching method which requires causality relationship to hold true. This means that at each point, the solution for DTOF is only dependent on the smallest value of diffusivity among the neighboring points.
4. All points with the drainage volume at any instant are assumed to be in steady state. This means that an instantaneous pressure drop occurs at the pressure front.
5. All points beyond the pressure front see no impact of the source at the well location. The Darcy flux is negligible beyond the drainage area. This is similar to pseudosteady state approximation in conventional pressure transient analysis.

5.4 Limitations of the approach

1 The proposed method is unable to handle 3D propagation of pressure transients with multiphase fluid. Further improvement of the proposed method is required in this regard.

2 The primary reservoir is assumed isotropic and homogeneous. This may not be representative of shale reservoirs where anisotropy and heterogeneity may interfere with interpretation of pressure transient response.

3 The method does not incorporate grid refinement which prevents consideration of fracture widths less than 1 ft. This may also be the cause for some error introduced in early-time results.

4 The method needs to be improved to allow interpretation in cases where the source well may be intersected by one or more natural fractures or is hydraulically fractured.

5 The method is based on fast marching method which requires causality relationship to hold true. This assumption fails in presence of large permeability contrasts. For permeability contrasts higher than 2 orders, the pressure predictions are not accurate.

6 The application of this method for non-conductive fractures needs further improvement. In the current approach, the pressure front chooses the path of highest diffusivity and bypasses the non-conductive zones. This makes characterization of non-conductive fractures difficult.

5.5 Illustration and Validation of Method

5.5.1. Illustration of MFM simulations of pressure propagation and pressure transient response for an abstract reservoir

Table 5.1- Summary of parameters assumed for the reservoir model shown in Figure 5.2a.

Reservoir size (ft)	2000×2000
Uniform grid size (ft)	1
Distance of no-flow boundary (ft)	1000
Production rate (bbl/d)	5
Total compressibility (psi^{-1})	6.00E-06
Fluid viscosity (cp)	0.4
Initial reservoir pressure (psi)	6000
Porosity (%)	20
Formation thickness (ft)	10
Wellbore radius (in)	3.6
Reservoir permeability (md)	0.01

This section qualitatively validates the MFM simulations. The abstract circular reservoir model has a radius of 1000 ft (**Figure 5.2a**) and the region outside the circular no-flow boundary has zero diffusivity. A vertical production well is located at the center of the reservoir model. An inner circular region of radius 100 ft with permeability 0.5 md is implemented in the model to prevent fast propagation of the pressure into the conductive wings. A 2000×300 ft rectangular section having permeability of 2 md is centrally located along the West-East (WE) diameter of the reservoir. A 2000×200 ft section having permeability of 1 md is centrally located along North-South (NS) diameter of the reservoir. The remaining portion of the abstract reservoir has a permeability of 0.01 md. In **Figure 5.2a**, higher permeability regions are in lighter colors, whereas the lower permeability regions are darker in color. **Table 5.1** lists parameters assumed for building the reservoir model. **Figure 5.2b** shows the propagation of the pressure front across the reservoir for a time period of 6 days. The pressure diffuses at higher speed along the high-permeability WE section. Contours of arrival time are farther spaced in the WE section compared to that in NS direction indicating a faster propagation. At the

end of 6 days, the pressure front has travelled farther in the WE section reaching the circular no-flow boundary.

Arrival-time contour joins all locations that require similar time for the propagating pressure front to travel from well to those locations and is similar to the drainage volume in the reservoir due to the production well. The increase in drainage volume with time can be used to calculate the change and Bourdet-type derivative of the PT response (**Figure 5.2c**). The constant pressure derivative till time of 0.2 days is result of circular zone with permeability 0.5 md around the well. At any instant, the pressure derivative is representative of the average permeability of area drained till that instant. A higher permeability is indicated by lower value of the pressure derivative. Once the pressure front moves into the WE section with higher permeability, there is a drop in the pressure derivative. Due to higher permeability in WE direction, the WE no-flow boundary is seen first at t = 6 days. Pressure derivative response exhibits linear trend after t =10 days when the boundaries in both the WE and NS rectangular sections are reached by the pressure front. The propagation of pressure front is slow in the four low-permeability sections (shown as dark gray regions in **Figure 5.2a**). This leads to very closely spaced arrival-time contour lines along the edges of the high-permeability WE and NS rectangular sections, indicating a slow pressure propagation into the low-permeability regions.

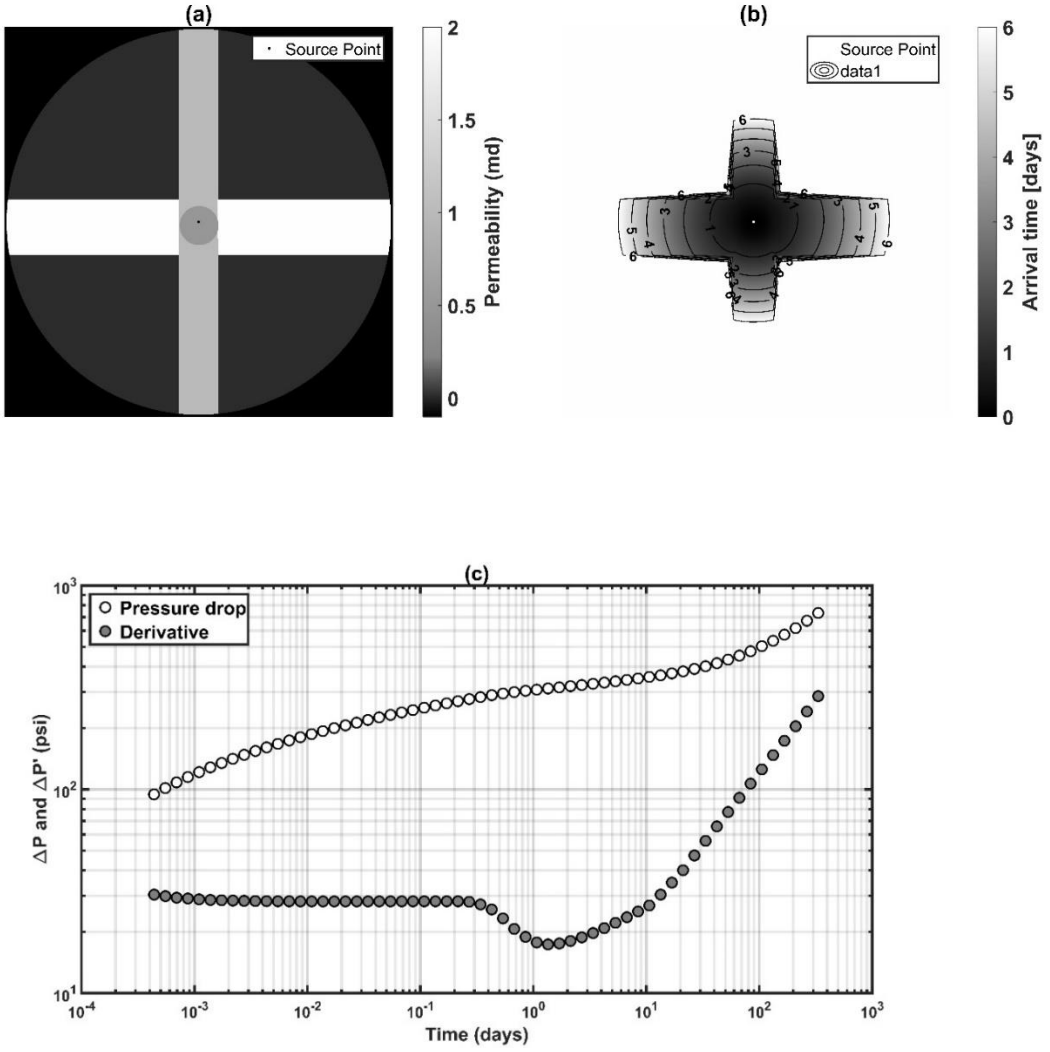


Figure 5.2: (a) Permeability map of the abstract reservoir, (b) MFM-generated arrival times for the pressure front propagating across the reservoir, and (c) pressure change and Bourdet-type pressure derivative responses of a vertical production well located in the center of the abstract reservoir.

5.5.2. Validation of MFM simulations against Kappa Saphir commercial software simulations for vertical production wells with and without hydraulically induced bi-wing planar fractures

MFM model simulations were compared against Kappa Saphir simulations for unfractured and fractured vertical wells centrally located in a homogeneous reservoir

having permeability of 0.1, 0.5, and 1 md (**Figure 5.3**). In these simulations, the reservoir does not contain natural fractures. In **Figure 5.3a**, we observe good match between the two simulation methods for the unfractured vertical well without induced hydraulic fractures. The pressure derivative is constant until the pressure front reaches the circular reservoir boundary, beyond which the derivative exhibits a unit slope. For the vertical production well with hydraulically induced bi-wing planar fractures, the predictions of the two methods show discrepancy during the early time (**Figure 5.3b**) because the current version of the MFM model does not handle local grid refinement for fractures. Values of other parameters used for this comparison is in **Table 5.2**.

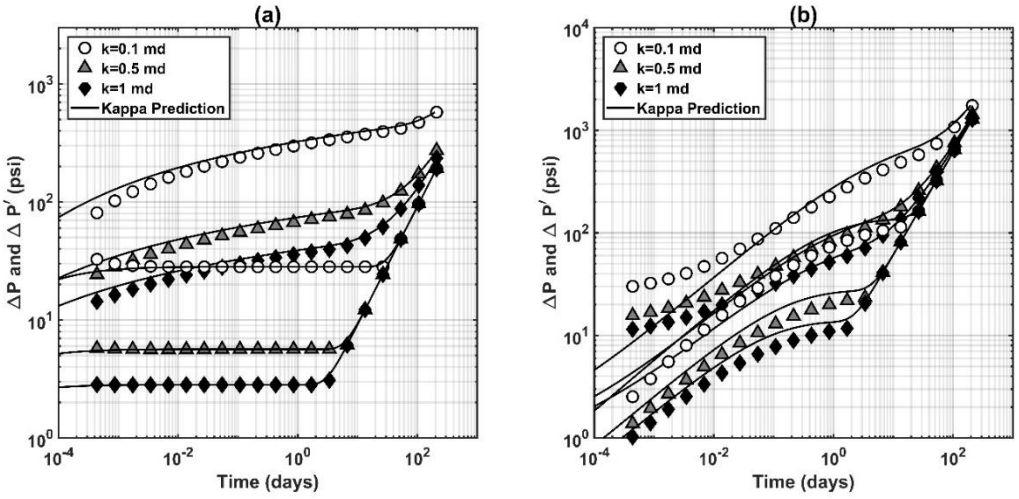


Figure 5.3: Validations of MFM-assisted predictions against Kappa Saphir predictions of pressure and its derivative responses in (a) unfractured and (b) fractured vertical well located centrally in bounded circular homogeneous reservoir for various reservoir permeabilities.

Table 5.2: Summary of parameters used for the comparisons shown in Figure 5.3.

Reservoir size (ft)	2000x2000
Uniform grid size (ft)	1
Distance of outer no-flow boundary (ft)	700
Production rate (bbl/d)	1
Total compressibility (psi^{-1})	2.00E-06
Fluid viscosity (cp)	0.4
Initial reservoir pressure (psi)	6000
Porosity (%)	20
Formation thickness (ft)	10
Wellbore radius (in)	3.6
Fracture half-length (ft)	100
Fracture permeability (md)	100
Fracture width (ft)	3
Production time (days)	400
Reservoir permeability (md)	0.1

5.5.3. MFM Simulations of Pressure Front Propagation and Pressure Transient Response of a Vertical Production Well in a Conceptual Sector/Concentric Reservoir Model

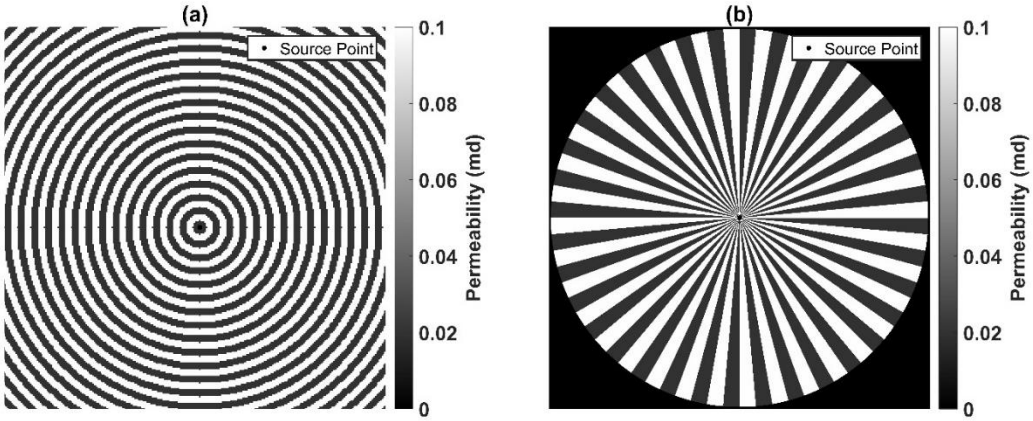


Figure 5.4: (a) Concentric reservoir model with 5-ft wide zones of alternating permeabilities, and (b) sector reservoir model with 5°-angle sectors of alternating permeabilities.

Conventional homogenization equations or effective medium (EM) equations are used to model various physical responses of mixtures as a combination of responses due

to the constituents. Similarly, it is common knowledge that, for approximating effective permeability of a reservoir comprising series distribution of two alternating equidimensional concentric layers of permeabilities k_1 and k_2 (**Figure 5.4a**), the following EM model is used

$$k_{eff} = \frac{\ln\left(\frac{r_e}{r_w}\right)}{\sum_1^n \frac{ln\left(\frac{r_{ext}}{r_{int}}\right)}{k_i}} \tag{5.2}$$

where k_{eff} is the approximate effective permeability (md), r_e is the radius of reservoir boundary (ft), r_w is the wellbore radius (ft), n is the number of concentric rings, r_{ext} is the outer radius of i-th ring, r_{int} is the inner radius of i-th ring and k_i is the permeability of the i-th ring. Similarly, for approximating effective permeability of a reservoir comprising parallel distribution of two alternating equidimensional sectored layers of permeabilities k_1 and k_2 (Fig. 4b), the following EM model is used

$$k_{eff} = \frac{(k_1\theta_1 + k_2\theta_2)}{(\theta_1 + \theta_2)} \tag{5.3}$$

where $k_1$is the permeability of the first alternating sector extending over an angle of θ_1, while k_2 & θ_2 are the corresponding properties of the second alternating sector.

Accuracy of conventional EM model increases when the alternating layers are very thin and the propagating front encounters an infinitely alternating media, as shown in Misra et al. (2016) for propagation of EM waves in a mixture containing parallel beds. We generate MFM simulations of Pressure Transient (PT) response of a vertical production well centrally located in the conceptual reservoir model comprising series/parallel distribution of permeabilities (**Figure 5.4**). These are compared against those for an equivalent homogeneous reservoir model having permeability equal to that

calculated using **Equations 5.2** and **5.3.** This helps to test the effectiveness of the conventional series/parallel effective medium equations for flow in a composite reservoir. These conceptual models comprise two alternating zones having permeability of 0.1 md and 0.02 md, respectively. Homogeneous reservoir models equivalent to the concentric and sector reservoir models can be generated by calculating the effective permeability of the conceptual models using series (**Equation 5.2**) and parallel (**Equation 5.3**). EM equations, respectively, in cylindrical coordinates. The effective permeability of concentric model is 0.04 md and that of sector model is 0.06 md.

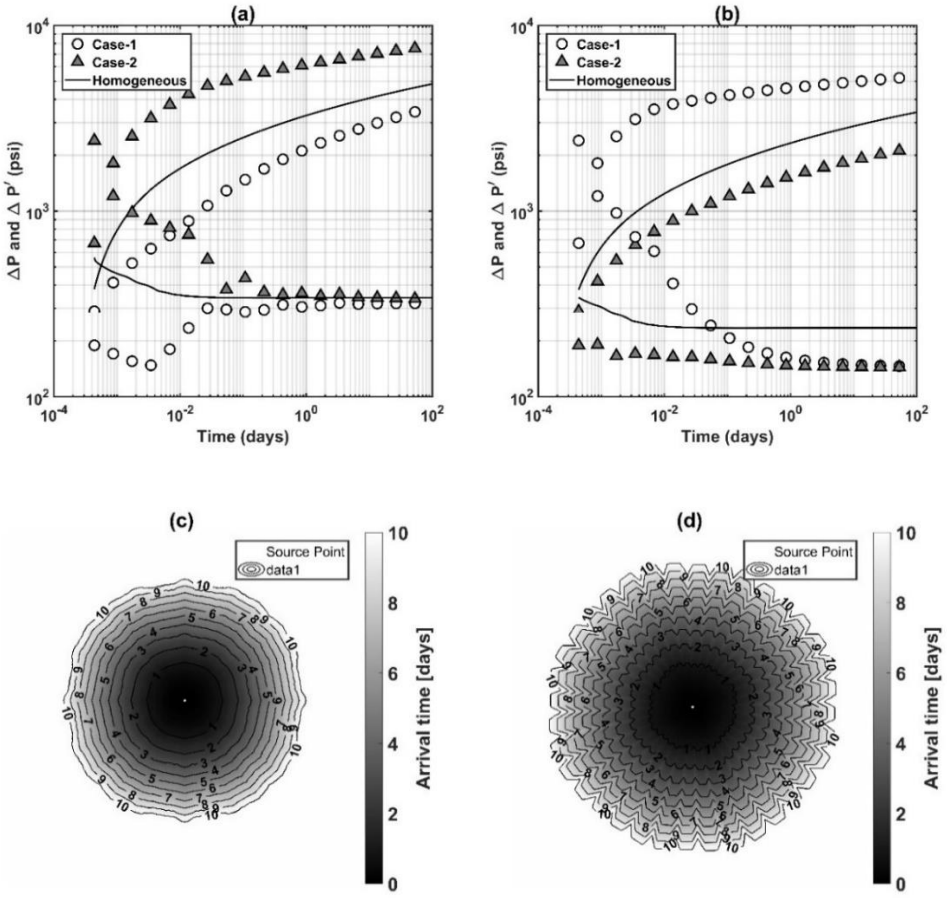


Figure 5.5: Pressure difference and pressure derivative responses of a vertical production well centrally located in (a) concentric model shown in Figure 5.4a and (b) sector model shown in Figure 5.4b. Temporal evolution of drainage areas till 10 days for (c) case-1 of concentric model and that for (d) case-1 of sector model.

When performing fast marching calculation for concentric or sector models, the early PT response is significantly affected by whether the first node is in the zone that has the higher permeability of 0.1 md (Case 1 in **Figure 5.5**) or the lower permeability of 0.02 md (Case 2 in **Figure 5.5**). As the pressure front propagates through larger numbers of alternating layers to a larger drainage area, the late-time pressure derivative response of the vertical production well in the concentric model converges with that of the equivalent homogeneous model (**Figure 5.5a**); however, there is discrepancy between the derivative response of sector model and that of the corresponding equivalent homogeneous model (**Figure 5.5b**). Importantly, the derivative responses of concentric and sector models oscillate and converge to steady values due to the homogenization effect. Pressure responses show large discrepancies due to initial errors in the pressure derivatives. In other words, pressure derivative responses are more reliable than pressure responses for history matching purposes in composite reservoirs.

5.6 Sensitivity of pressure transient response to properties of the naturally fractured reservoir

The characteristic properties of naturally fractured reservoir considered in the sensitivity study includes fracture orientation, fracture length, fracture compressibility, permeability contrast between matrix and fracture, and fracture volume fraction. Comparison of the modeled PT responses obtained in the sensitivity study will reveal diagnostic signatures that will aid PTA for naturally fractured systems containing conductive fractures. **Table 5.3** lists the values of the characteristic properties modeled in the Base Case of the sensitivity study. Values of all other relevant parameters are listed in **Table 5.1**. For the sensitivity study, natural fractures are assumed to be linear,

directionally aligned, randomly distributed, and more conductive than the reservoir background. For each case, all fractures in the reservoir have similar properties. This provides an ideal scenario to identify distinct features in the PT response of the naturally fractured systems.

For the Base Case, early-time derivative response is constant till the front encounters the nearest natural fracture, beyond that the derivative drops (**Figure 5.6b**). As the transient moves further outward, it encounters more conductive fractures; therefore, the effective permeability of the drainage area increases and derivative response progressively drops. In the Base Case, the decrease continues till the pressure front reaches the reservoir boundary, following that the derivative exhibits unit slope. The steady drop in derivative till the unit-slope response indicates that the conductive natural fractures are distributed over the entire reservoir.

Table 5.3: Summary of inputs used for Base Case of pressure transient response of a vertical production well in sensitivity study of characteristic properties of naturally fractured reservoir.

	Base Case Value
Fracture Orientation (deg)	30
Width (ft)	1
Length (ft)	50
Fracture Compressibility (psi^{-1})	6.00E-06
Volume Fraction (%)	1
Matrix permeability (md)	0.1
Fracture Permeability (md)	1
Well Location (X-Y)	1001-1001

Table 5.4: Summary of inputs used sensitivity on volume fraction of fractures.

	Base Case	Case-1	Case-2
Volume Fraction of fractures (%)	1	2	4

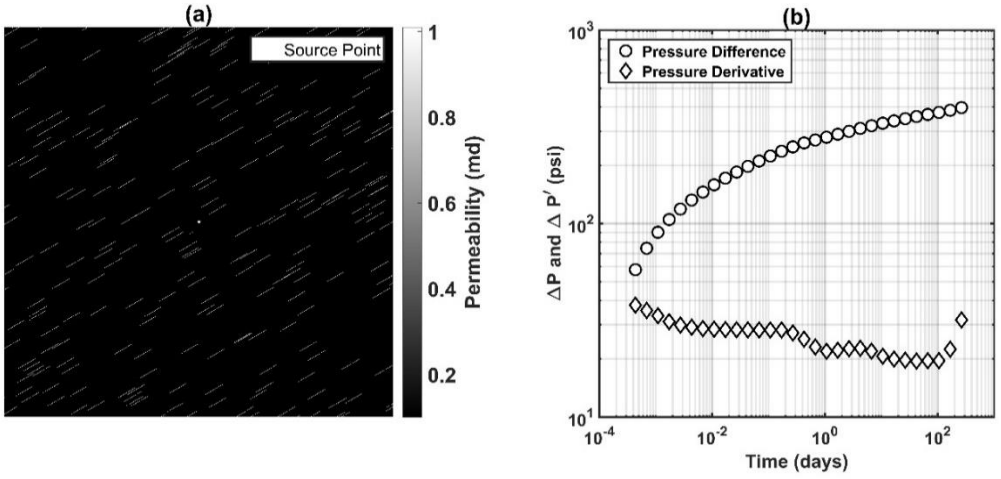


Figure 5.6: (a) Reservoir map for Base Case (dimension of square area shown in map is 1000 ft), and (b) pressure difference and pressure derivative responses of a vertical production well centrally located in Base Case reservoir.

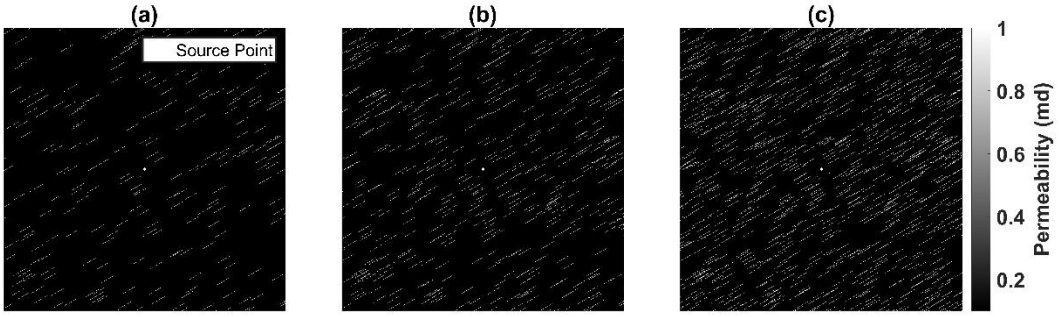


Figure 5.7: Reservoir map for (a) Base Case, (b) Case-1, and (c) Case-2. The dimension of square shown in each plot is 1000 ft.

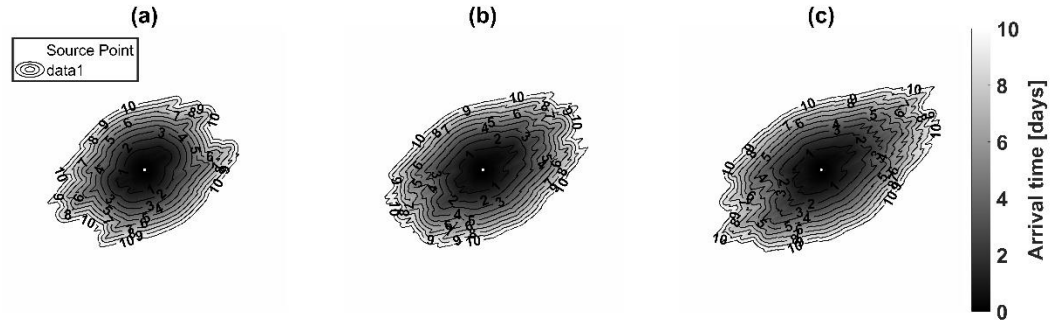


Figure 5.8: Time of arrival maps at *t*=10 days for (a) Base Case, (b) Case-1, and (c) Case-2. The dimension of square shown in each plot is 1000 ft.

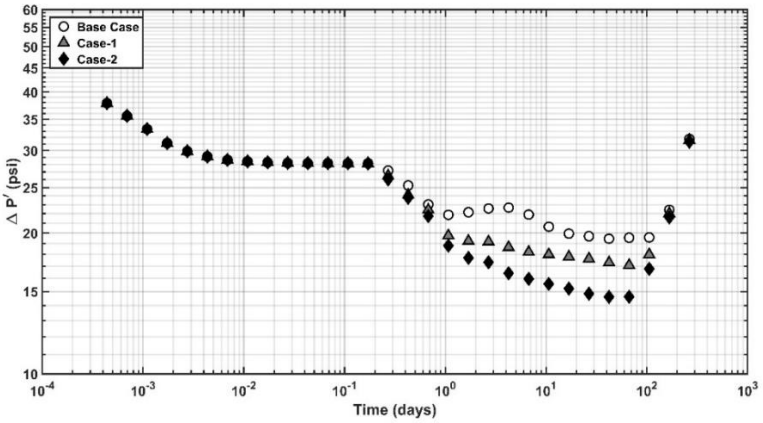


Figure 5.9: Pressure derivative responses of a vertical production well centrally located in reservoir to study sensitivity on volume fraction of fractures.

Volume fractions of the natural fractures in Base Case, Case-1, and Case-2 are 1%, 2% and 4%, respectively **(Table 5.4**) with remaining parameters same as shown in **Table 5.3**. The maps for the three cases are shown in **Figure 5.7** and the corresponding time of arrival contour maps are shown in **Figure 5.8**. For these three cases, the volume fraction of fracture and number of fractures increase while keeping the length and width of all fractures the same. The increase in volume fraction is achieved by increasing the number of fractures without altering the minimum distance of the fracture from source well. Derivative responses are relatively similar till 0.8 day (**Figure 5.9**). As the front moves away from the well, Case-2 exhibits the lowest derivative response indicating the highest effective permeability of the drainage area. This is evident in **Figures. 5.8a-c**, in which at 10 days, the drainage areas are significantly different and largest for Case-2. When the front reaches the circular reservoir boundary, the derivative responses converge and exhibit unit slopes. We notice an overall faster propagation of pressure front in Case-2 indicated by early signature of boundary flow.

Table 5.5: Summary of inputs used sensitivity on fracture permeability.

	Base Case	Case-3	Case-4	Case-5
Permeability of fractures (md)	1	0.2	10	0.01

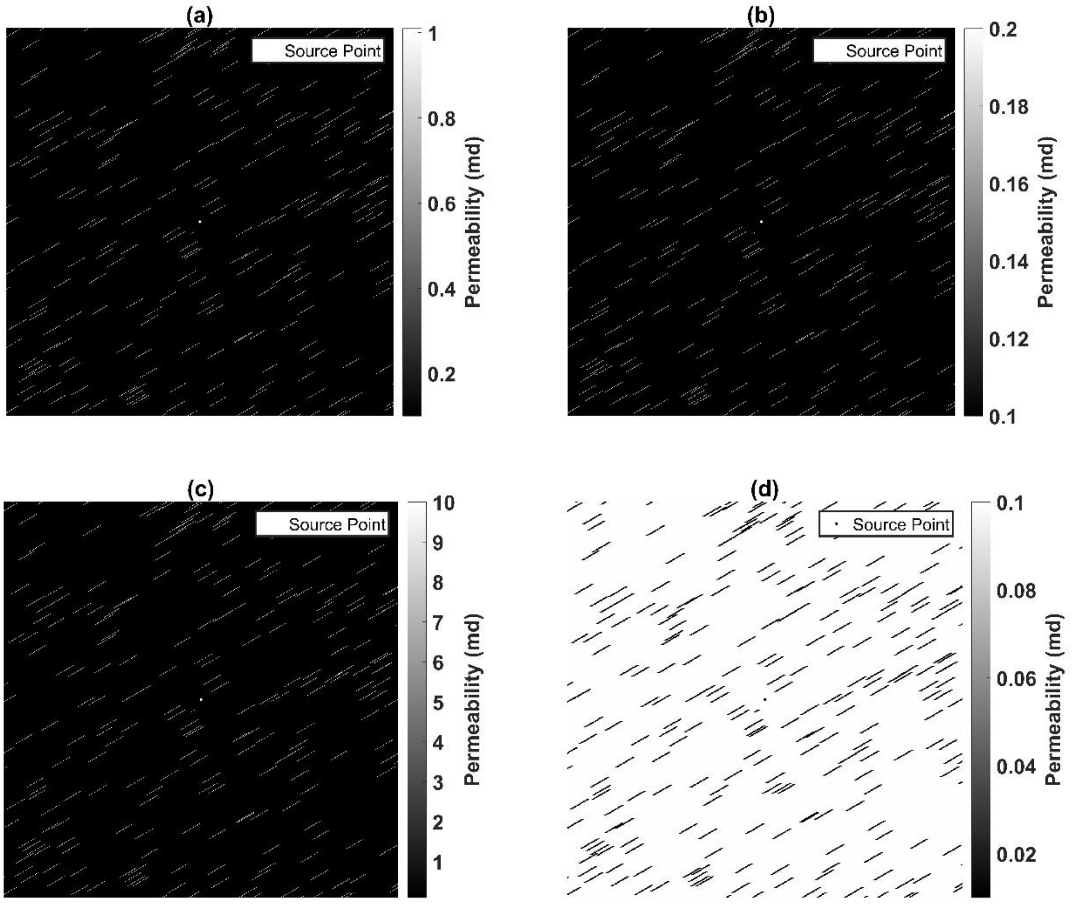


Figure 5.10: Reservoir map for (a) Base Case, (b) Case-3, (c) Case-4, and (d) Case-5. The dimension of square shown in each plot is 1000 ft.

Cases-3,4 & 5 are used to study the sensitivity to fracture permeability while ensuring the other properties to be similar. Cases 3 & 4 show cases where the fractures are more permeable compared to matrix whereas Case-5 considers the fractures to be non-conductive compared to matrix. **Table 5.5** shows the fracture permeability used in each case with the corresponding reservoir maps shown in **Figure 5.10** and time of arrival

maps shown in **Figure 5.11**. The position of fractures in each map remain the same with the permeability contrast between fracture and matrix as the variable. Derivative response starts dropping for all cases at the same time when the pressure front encounters the nearest conductive fracture. Out of all cases for conductive fractures, Case-3 has the lowest fracture permeability of 0.2 md with a permeability contrast of 2 with respect to the reservoir background. Consequently, Case-3 exhibits the slowest decline in derivative before the unit slope response. This indicates that a permeability contrast of 2 cannot be distinguished from the reservoir background response using pressure derivatives. As the fracture permeability increases, rate of decrease in the derivative response is faster as shown for Case-4 in **Figure. 5.12**. An increase in volume fraction of natural fractures and increase in fracture permeability leads to a drop in pressure derivative response. However, an increase in fracture permeability led to a dual minima and oscillation in derivative response which was not observed for the response due to increase in volume fraction. As expected, higher fracture permeability leads to faster propagation of pressure front and the circular reservoir boundary is reached earlier that results in the unit slope response (**Figure 5.12**). Presence of non-conductive fractures in Case-5 is accompanied by nearly horizontal pressure derivative (**Figure 5.12**) and nearly circular time of arrival contours (**Figure 5.11**). This indicates that the pressure transient tends to bypass the non-conductive fractures and stays in the continuous reservoir matrix. Therefore, the pressure derivative is not similar to that expected for a radial composite response.

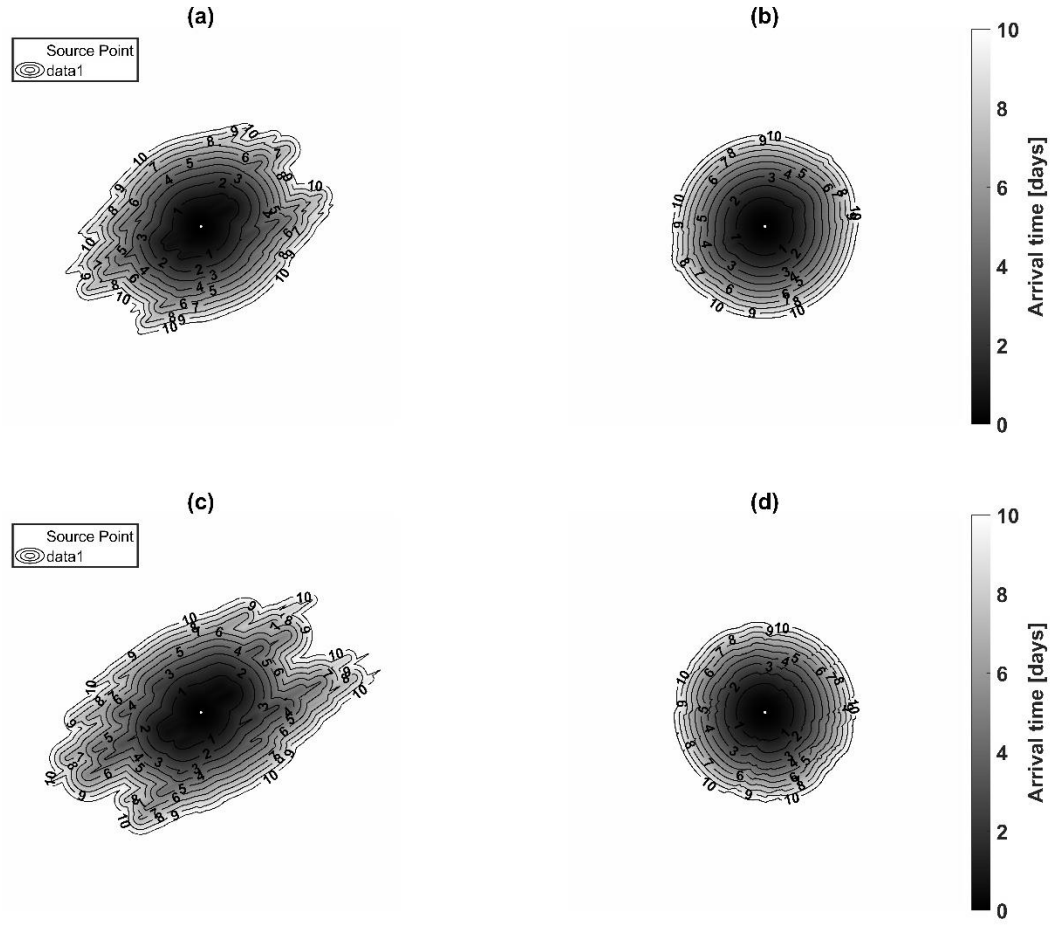


Figure 5.11: Time of arrival maps at *t*=10 days for (a) Base Case, (b) Case-3, (c) Case-4, and (d) Case-5. The dimension of square shown in each plot is 1000 ft.

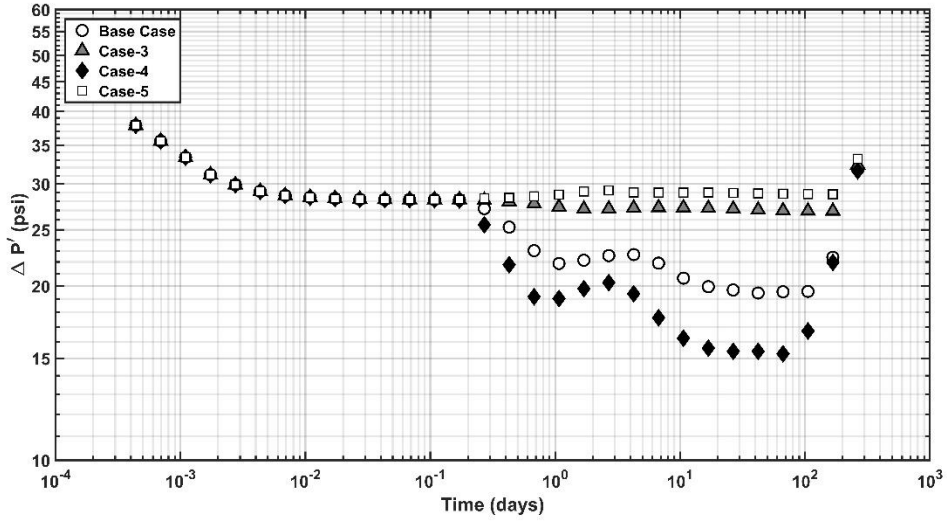


Figure 5.12: Pressure derivative responses of a vertical production well centrally located in reservoir to study sensitivity on permeability of fractures.

Table 5.6: Summary of inputs used sensitivity on compressibility of fractures.

	Base Case	Case-6	Case-7
Fracture Compressibility (psi^{-1})	6.00E-06	1.00E-06	1.00E-05

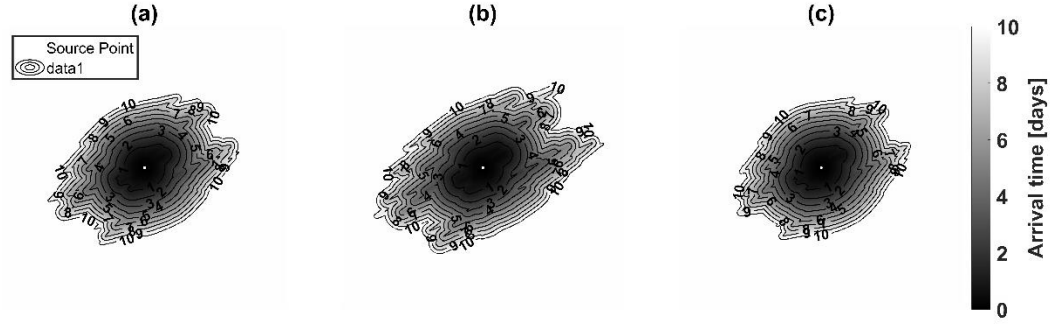


Figure 5.13: Time of arrival maps at *t*=10 days for (a) Base Case, (b) Case-6, and (c) Case-7. The dimension of square shown in each plot is 1000 ft.

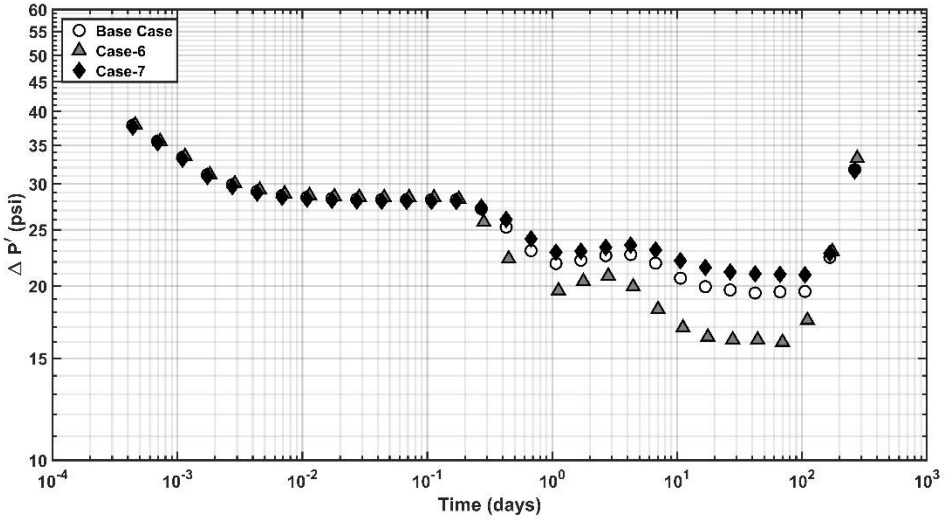


Figure 5.14: Pressure derivative responses of a vertical production well centrally located in reservoir to study sensitivity on compressibility of fractures.

Cases-6 & 7 are used to study the sensitivity to fracture compressibility while ensuring the other properties to be similar. **Table 5.6** shows the fracture compressibility used in each case with the corresponding reservoir maps remain same as that for Base

Case shown in **Figure 5.6a**. The time of arrival maps for each case is shown in **Figure 5.13** with the corresponding pressure derivatives shown in **Figure 5.14**. Since diffusivity is inversely proportional to compressibility, a lower fracture compressibility helps in increasing the contrast in diffusivity. For the same fracture distribution, Case-6 has faster propagation of pressure front due to lower compressibility whereas Case-7 has nearly circular time of arrival contours due to high fracture compressibility (**Figure 5.13**). The same response is also visible in derivative responses in **Figure 5.14** where the reservoir boundary is seen earliest for **Case-6.**

Table 5.7: Summary of inputs used sensitivity on location of source well.

	Base Case	Case-8	Case-9
Well Location	(1001,1001)	(901,1001)	(1001,1101)

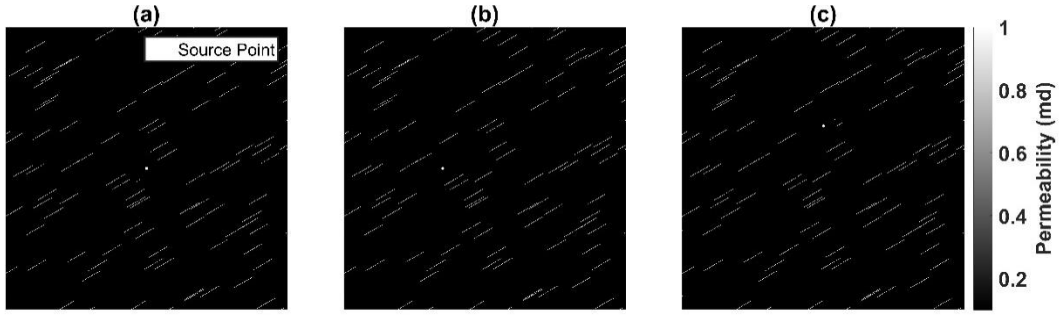


Figure 5.15: Reservoir map for (a) Base Case, (b) Case-8, and (c) Case-9. The dimension of square shown in each plot is 650 ft.

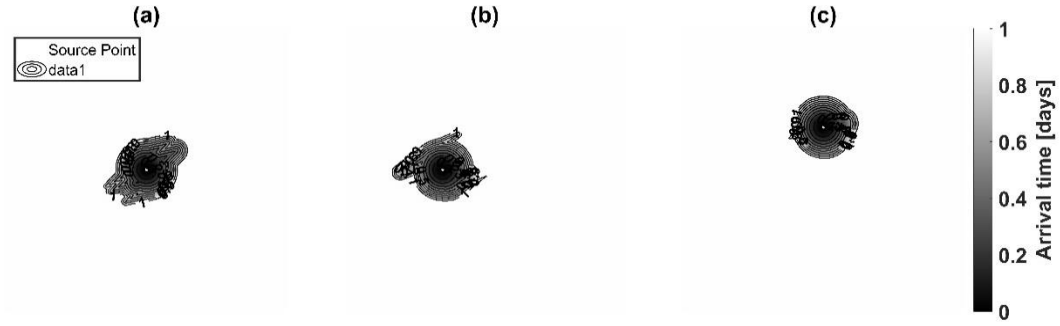


Figure 5.16: Time of arrival maps at *t*=1 day for (a) Base Case, (b) Case-8, and (c) Case-9. The dimension of square shown in each plot is 650 ft.

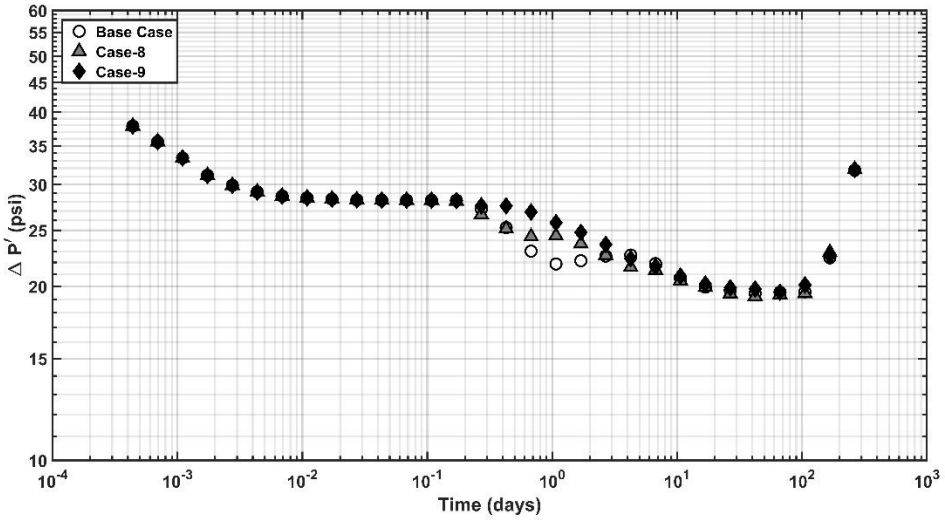


Figure 5.17: Pressure derivative responses of a vertical production well in reservoir to study sensitivity on location of source well.

Cases-8 & 9 are used to study the sensitivity to well location without altering other properties. **Table 5.7** shows the well location used in each case with the corresponding reservoir maps shown in **Figure 5.15**. The time of arrival maps for each case is shown in **Figure 5.16** with the corresponding pressure derivatives shown in **Figure 5.17**. In each case, the fractures are placed at minimum 30 ft distance from the well. The distribution of fractures in the immediate vicinity of well is variable due to variable well location. This results in different shape of contours indicating changes in pressure propagation when the pressure transient approaches the nearby fractures (**Figure 5.16**). The same is also visible in pressure derivative at t=1 day (**Figure 5.17**). When the pressure front moves further away, the overall distribution of fractures is same in each case as the map is unaltered. This leads to similar pressure propagation and pressure derivative response at time after t= 3 days.

Table 5.8: Summary of inputs used for normal distribution of fracture length and fracture orientation.

Normal distribution	Minimum Value	Mean Value	Maximum Value	Comment
Fracture Length (ft)	0	50	100	Case-10
Fracture Orientation (deg)	10	30	50	Case-11

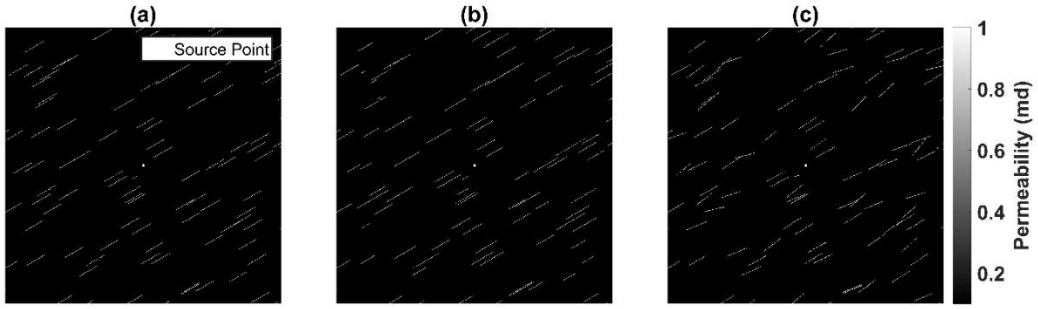


Figure 5.18: Reservoir map for (a) Base Case, (b) Case-10, and (c) Case-11 to implement variation in fracture length and orientation according to normal distribution. The dimension of square shown in each plot is 650 ft.

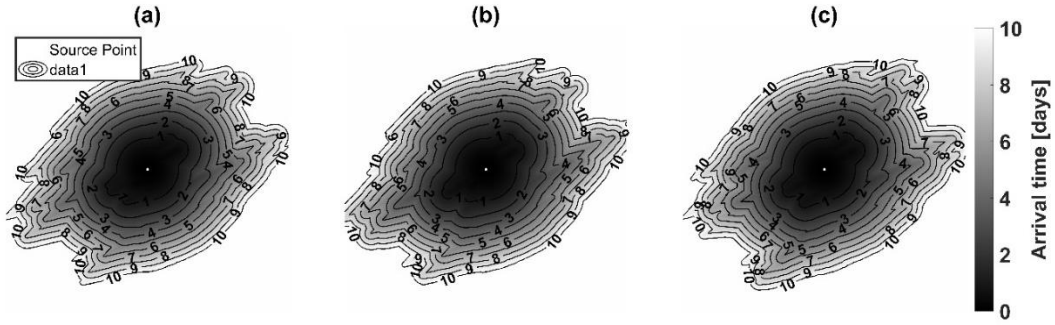


Figure 5.19: Time of arrival maps at *t*=10 days for (a) Base Case, (b) Case-10, and (c) Case-11. The dimension of square shown in each plot is 650 ft.

Cases-10 & 11 are used to study the impact of variation in fracture properties including fracture length and fracture orientation. The properties are assumed to vary according to normal distribution. The limits assumed for these properties are shown in **Table 5.8** with the corresponding reservoir maps shown in **Figure 5.18**. The time of arrival maps for each case is shown in **Figure 5.19** with the corresponding pressure

derivatives shown in **Figure 5.20c**. Due to variation in fracture characteristics, we see minor variation in the time of arrival contours for each case shown in **Figure 5.19**. However, these changes are negligible compared to total drainage volume at any instant which is shown by nearly identical pressure derivative response seen in **Figure 5.20c**. **Figures 5.20a & 5.20b** show that the normal distribution generated in the maps according to grid constraints is aligned with the theoretical normal distribution expected according to input limits.

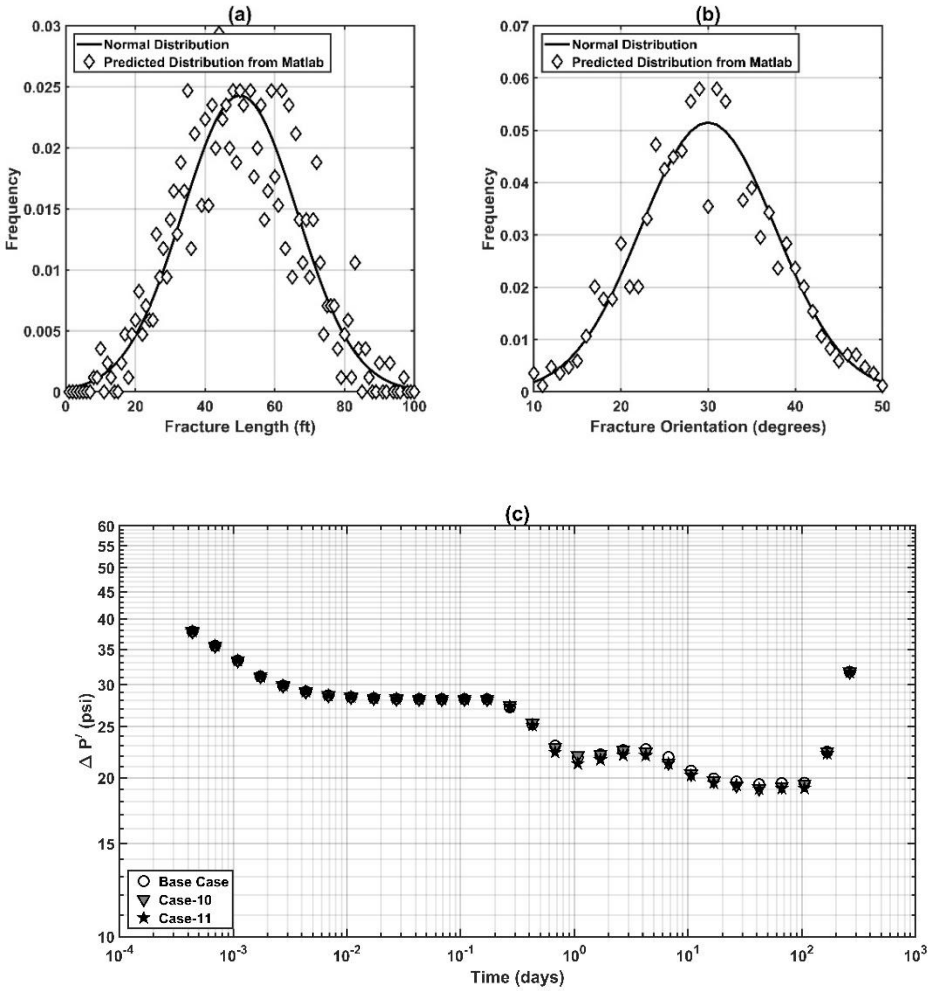


Figure 5.20: Comparison of normal distribution expected with that generated using Matlab for (a) length of natural fractures (Case-10), and (b) orientation of fractures (Case-11). (c) Pressure derivative responses of a vertical production well centrally located in reservoir to study impact of variation in fracture length and orientation.

These cases aim to replicate the variation of properties of natural fractures found in field cases. The volume fraction and permeability contrast of fractures are constant in each case. Under these conditions, it becomes evident that the impact of variation in characteristics of natural fractures is negligible and the system can be described using mean values of these characteristics. Impact of width has not been considered due to grid limitations which do not allow fracture width of less than 1 ft. For higher fracture widths, we do not expect any impact of variation, similar to cases shown here.

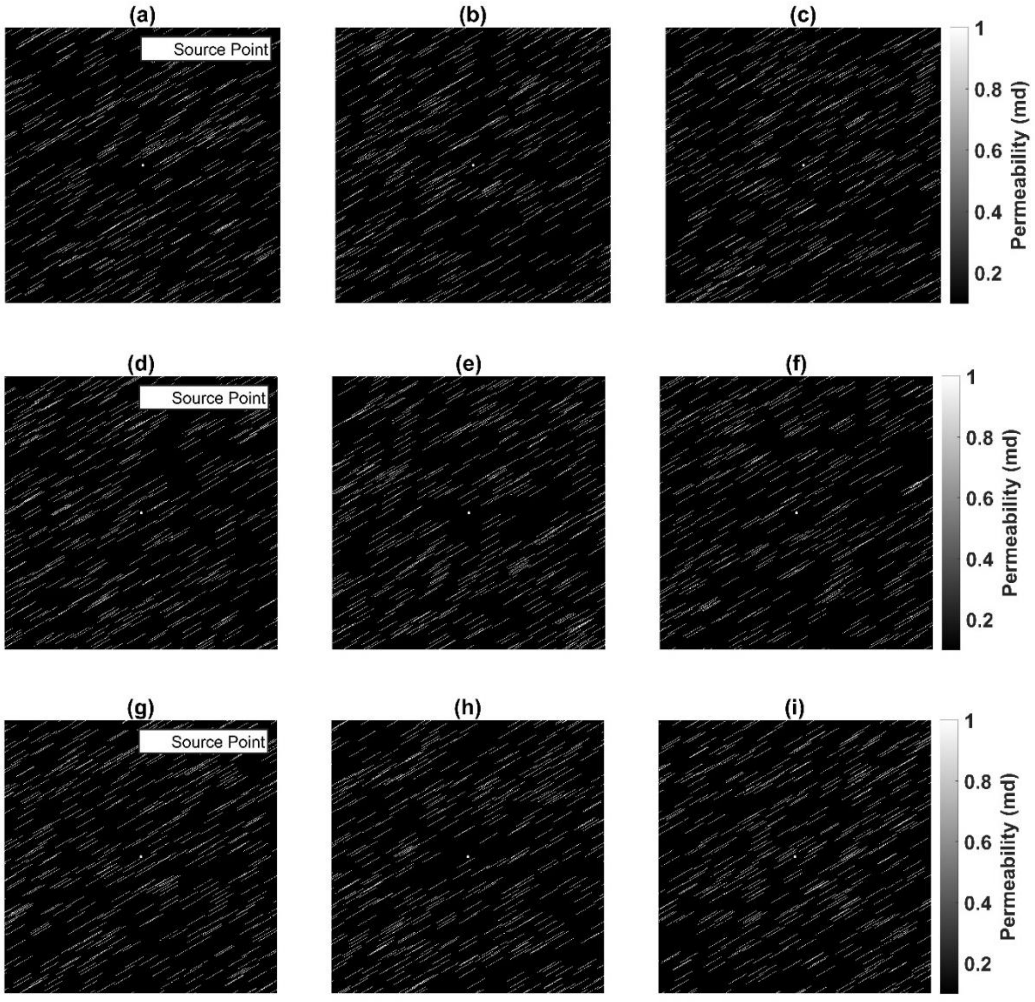


Figure 5.21- Reservoir maps for realizations in Cases 12-20 shown in (a)-(i) to show impact of change in position of natural fractures around well. The dimension of square shown in each plot is 650 ft.

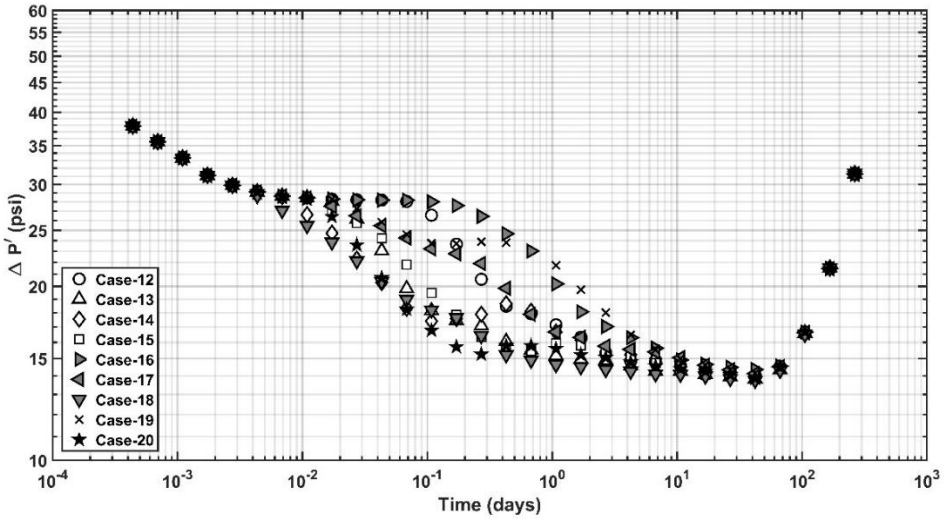


Figure 5.22: Pressure derivative responses of a vertical production well centrally located in reservoir to study impact of variation in position of fractures with random distribution between different realizations.

For considering the impact of change in distribution of fractures in the reservoir, 9 different realizations were considered (**Figure 5.21**). For each realization, all fracture properties like length, width and orientation remain same. Similarly, the volume fraction of fractures and the permeability contrast is also maintained constant. The position of fractures in the reservoirs is generated new is each case and is variable for different realizations. The closest distance of fractures with well is 5 ft and remains same for all cases in **Figure 5.21**. In each case (**Figure 5.22**), the pressure derivative remains same just near the well (t~0.003 day) and near the reservoir boundary (t~40 days). These values are dependent on volume fraction, permeability contrast and compressibility of fractures. Since these values remain unchanged between realizations, the pressure derivative has same value at these instants of time. The transition between these two fixed values varies according to position of fractures around the well. A sharp decrease in pressure derivative, as in Case-20 (**Figure 5.21i & Figure 5.22**), shows closer positioning of

fractures around the well. Similarly, fractures placed further away from well, as in Case-16 (**Figure 5.21e & Figure 5.22**), result in decrease of pressure derivative at later time. At any instant between early (t~0.003 day) and late time (t~40 days), the decrease in the pressure derivative is proportional to the fraction of fractures traversed by the propagating pressure front. Therefore, the shape of the curves is indicative of the distribution of fractures around the well.

CHAPTER 6: CONCLUSIONS AND RECOMMENDATIONS

6.1 Conclusions

Our method uses percolation theory, effective medium theory, and critical path analysis for estimation of relative permeability. The method assumes use of single coordination number, bimodal fractal model for pore size distrbution and negligible impact of surface pores on the percolation process. The method assumes water to be wetting phase for shale samples. We also assume efficacy of percolation theory along with critical path analysis in holistic prediction of transport properties including diffusion.

Based on these assumptions, relative permeability, residual/irreducible saturations, and production performance for Bakken, Eagle Ford, Wolfcamp, and Woodford shale formations from gas, oil, condensate and late-condensate maturity windows are estimated using low-pressure nitrogen adsorption-desorption measurements on the samples. Relative permeability curves for the wetting and non-wetting phases are well correlated with the thermal maturity, and the volume of pores of size ranging from 2 nm to 200 nm. Residual/irreducible saturations of both the phases tend to increase with increasing thermal maturity. The estimated relative permeability curves allow us to predict the expected production performance using a numerical simulator. The simulated production performances of the various formations exhibit greater variations in the horizontal well scenario compared to the vertical well scenario. Formations with lower thermal maturity show slower decline in hydrocarbon production rates and more uniform increase in water production.

The approach is limited due to the inability of adsorption measurements to describe pore diameters beyond range of 2-200 nm. The assumption of wettability of shale samples needs further investigation and validation. The method is yet to be validated using alternate laboratory experiments. The method is not strictly applicable on shale samples due to requirement of unimodal samples for application of universal scaling function along with presence of H1 or H2 hysteresis loops.

We also analyze a new approach to characterize conductive natural fractures in heterogeneous shale reservoirs, using multistencils fast marching method. This method assumes a homogeneous and isotropic 2D reservoir with a vertical well producing at a constant rate. The fluid is assumed to be single phase and slightly compressible. The method needs causality relationship to hold true and assumes pseudosteady state propagation of pressure wave in the reservoir.

Based on these assumptions, pressure transient response is analyzed to determine impact of change in fracture characteristics. The method can also prove useful in estimating the location of nearest natural fracture from the well. An increase in volume fraction of natural fractures, decrease in fracture compressibility and increase in fracture permeability lead to drop in pressure derivative responses. A progressive decrease in the derivative response is an indicator of conductive naturally fractured system, such that a short duration of such a drop indicates that the conductive fractures are distributed in a narrow band.

The method is limited in the present application due to its 2D approach and single phase fluid without any anisotropy in the reservoir. The present grid implementation needs to incorporate grid refinement techniques to consider natural fractures with width

smaller than 1 ft. It also needs improvement to consider variety of cases where natural fractures may be intersecting the production well. The causality relationship is an important assumption which breaks down if permeability shows more than 2 order of magnitude of variation in adjacent cells.

6.2 Recommendations for Future Work

The prediction of relative permeability based on percolation theory assumes water to be the wetting phase for shale samples and hydrocarbon is assumed to be wetting for isolated organic matter. Further research will be useful in evaluating this assumption on samples from different formations. Additionally, validation of the method using alternative methods of measurements on field data would be helpful in establishing the efficacy of the method for predicting production performance in shale reservoirs.

Analysis of natural fractures using multistencil fast marching method can be improved by extending the current 2D approach to 3D. Incorporation of multiphase flow will improve the versatility of the method. Most importantly, the current method uses a uniform grid of 1 ft. Due to this, fracture widths smaller than 1 ft cannot be modeled. Therefore, further research on incorporation of grid refinement which will also enable incorporation of complex fractures into the model is recommended. Wellbore effects may be accounted in the model. Also, the fast marching methods would be benefitted by improving their ability to handle large permeability contrasts within the reservoir.

REFERENCES

Alfi, M., Yan, B., Cao, Y., An, C., Wang, Y., He, J., & Killough, J. E. (2014, October). How to improve our understanding of gas and oil production mechanisms in liquid-rich shale. In SPE Annual Technical Conference and Exhibition. Society of Petroleum Engineers.

Bakshi, R., Halvaei, M. E., & Ghassemi, A. (2016a). Geomechanical Characterization of Core from the Proposed FORGE Laboratory on the Eastern Snake River Plain, Idaho.

Bakshi, R., Halvaei, M. E., & Ghassemi, A. (2016b). Injection Experiments on Basaltic Tuffs under Triaxial and Heated Conditions with Acoustic Emissions Monitoring. In 50th US Rock Mechanics/Geomechanics Symposium. American Rock Mechanics Association.

Barrett, E. P., Joyner, L. G., & Halenda, P. P. (1951). The determination of pore volume and area distributions in porous substances. I. Computations from nitrogen isotherms. Journal of the American Chemical society, 73(1), 373-380.

Behrenbruch, P., & Goda, H. M. (2006, January). Two-Phase Relative Permeability Prediction: A Comparison of the Modified Brooks-Corey Methodology with a New Carman-Kozeny Based Flow Formulation. In SPE Asia Pacific Oil & Gas Conference and Exhibition. Society of Petroleum Engineers.

Bounoua, N., Dozier, G. C., Montaggioni, P. J., & Etchecopar, A. (2008, January). Applied Natural fracture characterization using combination of imagery and transient information: Case studies from Cambro-Ordovician tight sandstones of Algeria. In SPE North Africa Technical Conference & Exhibition. Society of Petroleum Engineers.

Cluff, R. M., & Byrnes, A. P. (2010, June). Relative Permeability in Tight Gas Sandstone Reservoirs-The" Permeability Jail" Model. In SPWLA 51st Annual Logging Symposium. Society of Petrophysicists and Well-Log Analysts.

Cohan, L. H. (1938). Sorption hysteresis and the vapor pressure of concave surfaces. Journal of the American Chemical Society, 60(2), 433-435.

Curtis, M. E., Cardott, B. J., Sondergeld, C. H., & Rai, C. S. (2012). Development of organic porosity in the Woodford Shale with increasing thermal maturity. International Journal of Coal Geology, 103, 26-31.

Dacy, J. M. (2010). Core tests for relative permeability of unconventional gas reservoirs. Presented at SPE Annual Technical Conference and Exhibition, Florence, Italy, 19-22 September, 2010. SPE-135427-MS. doi:10.2118/135427-MS

Dadmohammadi*, Y., Misra, S., Sondergeld, C. H., & Rai, C. S. (2016b, August). Improved Petrophysical Interpretation of Laboratory Pressure-Step-Decay Measurements on Ultra-Tight Rock Samples. In Unconventional Resources Technology Conference, San Antonio, Texas, 1-3 August 2016 (pp. 888-904). Society of Exploration Geophysicists, American Association of Petroleum Geologists, Society of Petroleum Engineers.

Dadmohammadi, Y., Misra, S., Sondergeld, C. H., & Rai, C. S. (2016a, May). Simultaneous Estimation of Intrinsic Permeability, Effective Porosity, Pore Volume Compressibility, and Klinkenberg-Slip Factor of Ultra-Tight Rock Samples Based on Laboratory Pressure-Step-Decay Method. In SPE Low Perm Symposium. Society of Petroleum Engineers.

Daigle, H. (2016). Application of critical path analysis for permeability prediction in natural porous media. Advances in Water Resources, 96, 43-54.

Daigle, H., Ezidiegwu, S., & Turner, R. (2015, September). Determining Relative Permeability in Shales by Including the Effects of Pore Structure on Unsaturated Diffusion and Advection. In SPE Annual Technical Conference and Exhibition. Society of Petroleum Engineers.

Ghanbarian, B., Daigle, H., Hunt, A. G., Ewing, R. P., & Sahimi, M. (2015). Gas and solute diffusion in partially saturated porous media: Percolation theory and effective medium approximation compared with lattice Boltzmann simulations. Journal of Geophysical Research: Solid Earth, 120(1), 182-190.

Ghanbarian, B., Hunt, A. G., Ewing, R. P., & Skinner, T. E. (2014). Universal scaling of the formation factor in porous media derived by combining percolation and effective medium theories. Geophysical Research Letters, 41(11), 3884-3890.

Ghanbarian, B., Sahimi, M., & Daigle, H. (2016). Modeling relative permeability of water in soil: Application of effective-medium approximation and percolation theory. Water Resources Research.

Ghanbarian-Alavijeh, B., & Hunt, A. G. (2012). Unsaturated hydraulic conductivity in porous media: Percolation theory. Geoderma, 187, 77-84.

Gobin, O. C. (2006). SBA-16 materials: Synthesis, diffusion and sorption properties. Quebec, Canada: Laval University, 80p.

Han, G. (2011, January). Natural fractures in unconventional reservoir rocks: identification, characterization, and its impact to engineering design. In 45th US Rock Mechanics/Geomechanics Symposium. American Rock Mechanics Association.

Hassouna, M. S., & Farag, A. A. (2007). Multistencils fast marching methods: A highly accurate solution to the eikonal equation on cartesian domains. IEEE transactions on pattern analysis and machine intelligence, 29(9).

Honarpour, M. M., Nagarajan, N. R., Orangi, A., Arasteh, F., & Yao, Z. (2012, January). Characterization of Critical Fluid PVT, Rock, and Rock-Fluid Properties-Impact on Reservoir Performance of Liquid Rich Shales. In SPE Annual Technical Conference and Exhibition. Society of Petroleum Engineers.

Hunt, A. G., Ghanbarian, B., & Saville, K. C. (2013). Unsaturated hydraulic conductivity modeling for porous media with two fractal regimes. Geoderma, 207, 268-278.

Jarvie, D. M., Hill, R. J., Ruble, T. E., & Pollastro, R. M. (2007). Unconventional shale-gas systems: The Mississippian Barnett Shale of north-central Texas as one model for thermogenic shale-gas assessment. AAPG bulletin, 91(4), 475-499.

Khoshghadam, M., Lee, W. J., & Khanal, A. (2015). Impact of Fluid, Rock and Hydraulic Fracture Properties on Reservoir Performance in Liquid-Rich Shale Oil Reservoirs. Unconventional Resources Technology Conference (URTEC).

Kilpatrick, J. E., Eisner, L., & Williams-Stroud, S. (2010). Natural fracture characterization from microseismic source mechanisms: a comparison with FMI data. In SEG Technical Program Expanded Abstracts 2010 (pp. 2110-2114). Society of Exploration Geophysicists.

King, M. J., Wang, Z., & Datta-Gupta, A. (2016, May). Asymptotic Solutions of the Diffusivity Equation and Their Applications. In SPE Europec featured at 78th EAGE Conference and Exhibition. Society of Petroleum Engineers.

Klaver, J., Hemes, S., Houben, M., Desbois, G., Radi, Z., & Urai, J. L. (2015). The connectivity of pore space in mudstones: insights from high-pressure Wood's metal injection, BIB-SEM imaging, and mercury intrusion porosimetry. Geofluids, 15(4), 577-591.

Kruk, M., Antochshuk, V., Jaroniec, M., & Sayari, A. (1999). New approach to evaluate pore size distributions and surface areas for hydrophobic mesoporous solids. The Journal of Physical Chemistry B, 103(48), 10670-10678.

Kruk, M., Jaroniec, M., & Sayari, A. (1997). Application of large pore MCM-41 molecular sieves to improve pore size analysis using nitrogen adsorption measurements. Langmuir, 13(23), 6267-6273.

Kruk, M., Jaroniec, M., Ko, C. H., & Ryoo, R. (2000). Characterization of the porous structure of SBA-15. Chemistry of materials, 12(7), 1961-1968.

Kuila, U., & Prasad, M. (2013a). Application of nitrogen gas-adsorption technique for characterization of pore structure of mudrocks. Lead Edge 32 (12): 1478–1485.doi: 10.1190/tle32121478.1.

Kuila, U., & Prasad, M. (2013b). Specific surface area and pore-size distribution in clays and shales. Geophysical Prospecting, 61(2), 341-362.

Lelièvre, P. G., Farquharson, C. G., & Hurich, C. A. (2011). Computing first-arrival seismic traveltimes on unstructured 3-D tetrahedral grids using the Fast Marching Method. Geophysical Journal International, 184(2), 885-896.

Liu, H., Zhang, L., & Seaton, N. A. (1992). Determination of the connectivity of porous solids from nitrogen sorption measurements—II. Generalisation.Chemical Engineering Science, 47(17), 4393-4404.

Liu, H., Zhang, L., & Seaton, N. A. (1993). Analysis of sorption hysteresis in mesoporous solids using a pore network model. Journal of colloid and interface science, 156(2), 285-293.

Liu, H., Zhang, L., & Seaton, N. A. (1994). Characterisation of mesoporous solids using sorption hysteresis measurements. Studies in Surface Science and Catalysis, 87, 129-139.

Loucks, R. G., Reed, R. M., Ruppel, S. C., & Jarvie, D. M. (2009). Morphology, genesis, and distribution of nanometer-scale pores in siliceous mudstones of the Mississippian Barnett Shale. Journal of sedimentary research, 79(12), 848-861.

Martys, N. S. (1999). Diffusion in partially-saturated porous materials. Materials and Structures, 32(8), 555-562.

Mastalerz, M., Schimmelmann, A., Drobniak, A., & Chen, Y. (2013). Porosity of Devonian and Mississippian New Albany Shale across a maturation gradient: Insights from organic petrology, gas adsorption, and mercury intrusion. AAPG bulletin, 97(10), 1621-1643.

Meyer, K., & Klobes, P. (1999). Comparison between different presentations of pore size distribution in porous materials. Fresenius' journal of analytical chemistry, 363(2), 174-178.

Misra, S., Torres-Verdín, C., Revil, A., Rasmus, J., & Homan, D. (2016). Interfacial polarization of disseminated conductive minerals in absence of redox-active species—Part 1: Mechanistic model and validation. Geophysics.

Nassef, E., Soliman, A., Al-Alla, R.A. and Eltaweel, Y. (2015) Experimental study on solvent extraction of Quseir oil shale in Egypt. Journal of Surface Engineered Materials and Advanced Technology, 5, 147-153. http://dx.doi.org/10.4236/jsemat.2015.53016

Odusina, E. O., Sondergeld, C. H., & Rai, C. S. (2011, January 1). NMR Study of Shale Wettability. Society of Petroleum Engineers. doi:10.2118/147371-MS

Ojha, S. P., Misra, S., Sinha, A., Dang, S., Sondergeld, C., & Rai, C. (2017d). Estimation of Pore Network Characteristics and Saturation-Dependent Relative Permeability in Organic-Rich Shale Samples Obtained from Bakken,

Wolfcamp, and Woodford Shale Formations. In SPWLA 58th Annual Logging Symposium. Society of Petrophysicists and Well-Log Analysts.

Ojha, S. P., Misra, S., Sinha, A., Dang, S., Tinni, A., Sondergeld, C., & Rai, C. (2017e). Relative Permeability and Residual Saturation Estimates for Organic-Rich Shale Samples from Bakken, Wolfcamp, Eagle Ford and Woodford Formations. In SPE Annual Technical Conference and Exhibition. Society of Petroleum Engineers.

Ojha, S. P., Misra, S., Tinni, A. O., Sondergeld, C. H., & Rai, C. S. (2016). Estimation of Saturation-Dependent Relative Permeability in Shales based on Adsorption-Desorption Isotherm. In AAPG Eastern Section Meeting.

Ojha, S. P., Misra, S., Tinni, A., Sinha, A., Dang, S., Sondergeld, C., & Rai, C. (2017c). Alterations in Pore Topology of Organic-Rich Shale Samples Due to the Removal of Dead Oil, Bitumen, and Kerogen. In SPWLA 58th Annual Logging Symposium. Society of Petrophysicists and Well-Log Analysts.

Ojha, S. P., Misra, S., Tinni, A., Sondergeld, C., & Rai, C. (2017a). Relative permeability estimates for Wolfcamp and Eagle Ford shale samples from oil, gas and condensate windows using adsorption-desorption measurements. Fuel, 208, 52-64.

Ojha, S. P., Misra, S., Tinni, A., Sondergeld, C., & Rai, C. (2017b). Pore connectivity and pore size distribution estimates for Wolfcamp and Eagle Ford shale samples from oil, gas and condensate windows using adsorption-desorption measurements. Journal of Petroleum Science and Engineering, 158, 454-468.

Perfect, E. (2005). Modeling the primary drainage curve of prefractal porous media. Vadose Zone Journal, 4(4), 959-966

Ross, D. J., & Bustin, R. M. (2009). The importance of shale composition and pore structure upon gas storage potential of shale gas reservoirs. Marine and Petroleum Geology, 26(6), 916-927.

Sahimi, M. (1993). Fractal and superdiffusive transport and hydrodynamic dispersion in heterogeneous porous media. Transport in porous Media, 13(1), 3-40.

Seaton, N. A. (1991). Determination of the connectivity of porous solids from nitrogen sorption measurements. Chemical Engineering Science, 46(8), 1895-1909.

Sethian, J. A. (1996). A fast marching level set method for monotonically advancing fronts. Proceedings of the National Academy of Sciences, 93(4), 1591-1595.

Shanley, K. W., Cluff, R. M., & Robinson, J. W. (2004). Factors controlling prolific gas production from low-permeability sandstone reservoirs: Implications for resource assessment, prospect development, and risk analysis. AAPG bulletin, 88(8), 1083-1121.

Sharifi, M., & Kelkar, M. (2014). Novel permeability upscaling method using fast marching method. Fuel, 117, 568-578.

Sharifi, M., Kelkar, M., Bahar, A., & Slettebo, T. (2014). Dynamic ranking of multiple realizations by use of the fast-marching method. SPE Journal, 19(06), 1-069.

Sinha, A. (2017). Surface Area Study in Organic Rich Shales using Nitrogen Adsorption. http://hdl.handle.net/11244/52243

Springer, D. S., Loaiciga, H. A., Cullen, S. J., & Everett, L. G. (1998). Air permeability of porous materials under controlled laboratory conditions. Ground Water, 36(4), 558-565.

Valenza, J. J., Drenzek, N., Marques, F., Pagels, M., & Mastalerz, M. (2013). Geochemical controls on shale microstructure. Geology, 41(5), 611-614.

Vasco, D. W., Keers, H., & Karasaki, K. (2000). Estimation of reservoir properties using transient pressure data: An asymptotic approach. Water Resources Research, 36(12), 3447-3465.

Vassilev, S. V., & Tascón, J. M. (2003). Methods for characterization of inorganic and mineral matter in coal: a critical overview. Energy & Fuels, 17(2), 271-281.

Xie, J., Gupta, N., King, M. J., & Datta-Gupta, A. (2012, January). Depth of investigation and depletion behavior in unconventional reservoirs using fast marching methods. In SPE Europec/EAGE Annual Conference. Society of Petroleum Engineers.

Xiong, F., Jiang, Z., Chen, J., Wang, X., Huang, Z., Liu, G., ... & Zhang, L. (2016). The role of the residual bitumen in the gas storage capacity of mature lacustrine shale: A case study of the Triassic Yanchang shale, Ordos Basin, China. Marine and Petroleum Geology, 69, 205-215.

Yang, F., Ning, Z., & Liu, H. (2014). Fractal characteristics of shales from a shale gas reservoir in the Sichuan Basin, China. Fuel, 115, 378-384.

Yao, Y., Liu, D., Tang, D., Tang, S., Huang, W., Liu, Z., & Che, Y. (2009). Fractal characterization of seepage-pores of coals from China: an investigation on permeability of coals. Computers & Geosciences, 35(6), 1159-1166.

Yao, Yanbin, et al. (2008): "Fractal characterization of adsorption-pores of coals from North China: an investigation on CH4 adsorption capacity of coals." International Journal of Coal Geology 73.1, 27-42.

Yoon, S. (2017). Numerical Simulation of the Effects of Reservoir Heterogeneity, Fractures, and Multi-Well Interference on Pressure Transient Responses Using Multistencils Fast Marching Method. http://hdl.handle.net/11244/51921

Zhang, Y., Bansal, N., Fujita, Y., Datta-Gupta, A., King, M. J., & Sankaran, S. (2016). From Streamlines to Fast Marching: Rapid Simulation and Performance Assessment of Shale-Gas Reservoirs by Use of Diffusive Time of Flight as a Spatial Coordinate. SPE Journal, 21(05), 1-883.

APPENDIX A: NOMENCLATURE

k_1	Permeability of first sector in sector model (md)
k_2	Permeability of second sector in sector model (md)
k_{eff}	Effective Permeability of reservoir model (md)
r_e	Drainage radius of reservoir (ft)
r_{ext}	Outer radius of *i*-th layer in concentric ring model (ft)
r_{int}	Inner radius of *i*-th layer in concentric ring model (ft)
r_w	Wellbore radius (ft)
b	Constant with universal value of 0.41
c_t	Total compressibility (psi^{-1})
d	Pore diameter (nm)
D	Fractal Dimension
D_1	Fractal Dimension for first fractal regime
D_2	Fractal Dimension for second fractal regime
d_{max}	Maximum pore diameter (nm)
d_{min}	Minimum pore diameter (nm)
d_x	Pore diameter at which fractal regime changes from regime-1 to regime-2 (nm)
$F(P)$	Percolation Probability
$f(P)$	Site Occupation Probability
f_c	Percolation Threshold
i	Reference for layer number in concentric ring model
k	Permeability (md)
$k(x)$	Permeability at node *x* (md)
k_{rhc}	Hydrocarbon Relative Permeability
k_{rnw}	Relative permeability of nonwetting phase
k_{rw}	Relative permeability of wetting phase
L	Percolation cluster length
n	No. of layers in concentric ring model
P	Pressure (psi)
P/P_o	Relative Pressure
P_o	Nitrogen saturation pressure (1 atm)
r	Pore radius (nm)
R	Universal gas constant (8.314 J/mol/K)
S_{hcr}	Residual hydrocarbon saturation
S_{wir}	Irreducible water saturation
T	Absolute temperature for adsorption experiment (77 K)
t	Thickness of adsorbed layers of nitrogen in nm
t	Time of pressure wave propagation (days)
v	Constant with universal value of 0.88
V	Pore Volume Distribution (cc/g)
V_a	Total volume of nitrogen gas that would desorb at that pressure if all pores had access to nitrogen vapor phase
V_d	Volume of nitrogen gas that desorb at a given pressure
V_L	Nitrogen molar volume (34.68 cc/mol)

w	Mean pore diameter (nm)
Z	Coordination Number
k	Reservoir permeability (md)
$v(w)$	Distribution of pore volume as a function of pore diameter
$\varphi_1(d)$	Contribution to pore volume from first fractal regime
$\varphi_2(d)$	Contribution to pore volume from second fractal regime
θ_1	Angle subtended by first sector in sector model (°)
θ_2	Angle subtended by second sector in sector model (°)
μ	Fluid viscosity (cp)
β	Probability of Drainage
β_1	Probability of Drainage for first fractal regime
β_2	Probability of Drainage for second fractal regime
ΔP	Pressure difference (psi)
$\Delta P'$	Bourdet pressure derivative (psi)
θ	Pore volume fraction
$\theta(d)$	Cumulative volume distribution of pore sizes
θ_d	Crossover volume fraction for wetting phase
θ_{nw}	Pore volume fraction of nonwetting phase
θ_t	Critical Phase Content
θ_w	Pore volume fraction of wetting phase
θ_x	Crossover volume fraction for non-wetting phase
$\varphi(x)$	Porosity at node *x* (fraction)
α_s	Constants needed to convert the measured nitrogen gas volume to required liquid nitrogen volume adsorbed at each pressure step
β	Probability of Drainage
ϕ	ADI pore volume
γ	Surface tension (8.88 x 10^3 N/m)
α	Diffusivity (time$^{-0..5}$)
$\tau(x)$	Diffusive time of flight (time$^{0.5}$)
AD	Adsorption-Desorption
ADI	Adsorption-Desorption Isotherm
APV	ADI Pore Volume
BJH	Barrett-Joyner-Halenda
CPA	Critical path analysis
DFT	Density Functional Theory
DH	Dollimore-Heal
DTOF	Diffusive Time of Flight
EF	Eagle Ford Formation
EMT	Effective Medium Theory
EUR	Estimated ultimate recovery
FHH	Frenkel-Halsey-Hill
FM	Fast Marching
FTIR	Fourier Transform Infrared
LPP	Low Pressure Helium Pycnometry

LTA	Low Temperature Ashing
MFM	Multistencil Fast Marching Method
PSD	Pore Size Distribution
PT	Percolation Theory
PT	Pressure Transient
PVT	Pressure-Volume-Temperature
SEM	Scanning electron microscopy
TOC	Total organic content
WD	Woodford formation
WF	Wolfcamp formation

Subscripts

gr	Residual for gas phase
max	Maximum
min	Minimum
nw	Non-wetting phase
hcr	Residual for hydrocarbon phase
w	Wetting phase
wir	Irreducible for water phase